NTNU
Kunnskap for en bedre verden

DEPARTMENT OF MATERIAL SCIENCE

Characterization of Polymetallic Manganese Nodules and Reduction by Hydrogen and Methane

Author:
Jonas Låstad, Ole Kristian Brustad

May, 2022

Foreword

This bachelor thesis is the final assignment of our bachelor at the Norwegian University of Science and Technology (NTNU). It is written at NTNU, Department of Material Science and Engineering the spring of 2022. Special thanks go to our two supervisors Associate Professor Jafar Safarian and our cosupervisor Dr. Arman Hoseinpur-Kermani. Whom have guided our work and helped shape this project and without whom this project could not have been completed, if not even begun. With their knowledge of the field, they put us on the right path for what parts of the project needed to be completed. We are grateful for the help the supervisors have provided and for all the interesting discussions on the data gathered making us all the more knowledgeable on the subject. Further, we want to extend our gratitude to the following people for their invaluable help through the project:

- Arman Hoseinpur-Kermani for invaluable help and guidance working the ReSiNa furnace and for leaving your office door open whenever a question arose.
- Andrey Kosinskiy for good help and guidance with metallography, electron microscopy and X-ray diffraction analysis.
- Berit Vinje Kramer for good help and guidance at the high temperature lab.
- Caitilin Guzzo for good guidance with the XRD-analysis.
- Jonas Einan Gjøvik for interesting talks during some otherwise boring reduction experiments.
- The student counsil of the faculty of natural science for letting us use their office and drink their coffee.
- All our friends and family whom had to suffer our complaints, and did their best to help.
- All the staff at NTNU for making this project a reality.

Abstract

The field of subsea mining has been investigated since the 19th century with a heightened interest arising in the 1970's. Due to an increase in demand of valuable metals such as copper, cobalt, and nickel this field is once again experiencing heightened interest. The Clarion Clipperton Fracture Zone contains vast reserves of polymetallic manganese nodules which contains considerable amounts of minerals of manganese, iron, copper, nickel, and cobalt as well as other minerals such as rare earths.

Another development is the need to reduce the carbon footprint of metal production. As such the exploration of gaseous reduction processes, utilizing hydrogen and/or methane as reactants, is becoming more and more relevant. This bachelor thesis investigates an overall process of calcination and reduction utilizing various mixtures of methane and hydrogen as reduction agents. The ore used in this study originated from the Clarion Clipperton Fractured Zone.

The results given in this paper was found by:

- Chemical analysis of the raw and calcined ore by XRF.
- Specific surface area of the calcined ore found by BET.
- Thermogravimetric analysis of the calcination and reduction process.
- Electron microscope images of the raw, calcined and reduced ore.
- Element distribution in sample by SEM-EDX.
- X-ray diffraction patterns of the raw, calcined and reduced ore.

The main findings of this paper is that:

- Polymetallic manganese nodules will produce metallic iron, nickel, and copper when reduced at 900°C in an environment with readily available reactants of either methane or hydrogen gas. Phases of cobalt was not identified, but is theoretically reduced to a metallic state, and may have alloyed with another metal.
- No carbide was found in the samples reduced by methane-containing gases
- Manganese oxides were reduced to a phase of manganosite (MnO).
- Silicon content of the ore greatly affected the reduced samples, binding elements of manganese and iron into phases of fayalite and tephorite.
- Aluminium in the reduced sample entered phases with silicon, sodium and potassium in phases of nepheline.
- The increase in porosity of the manganese nodules during calcination allows for easy mass transport of reactants and gaseous reduction products, possibly allowing for processing without a pelletization stage.
- The reaction speed of the reduction is significant and appear exothermic in nature.

Sammendrag

Feltet havbunns gruvedrift har blitt utforsket siden 1800-tallet, med stor utvikling rundt 1970-tallet. På grunn av en økning i etterspørselen etter verdifulle metaller slik som kobber, kobolt og nikkel har dette feltet fått gjenvunnet interesse. Clarion Clipperton sonen inneholder enorme reserver av polymetalliske noduler rike på mineraler av mangan, jern, kobber, nikkel og kobolt så vel som mineraler av sjeldne jordarter.

En annen utvikling har vært behovet for å redusere karbonavtrykket til metallproduksjonen. Dermed utforskningen av gassbaserte reduksjonsprosesser, ved bruk av hydrogen og/eller metan som reaksjonsmiddler mer og mer relevante.

Denne rapporten utforsker en overgående prosess med kalsinering og reduksjon ved bruk av ulike av konsentrasjoner av metan og hydrogen som reduksjonsmidler. Malmen brukt i denne oppgaven kommer opprinnelig fra Clarion Cliperton sonen i Stillehavet.

Resultatene gitt i denne rapporten ble funnet ved:

- Kjemisk analyse av rå og kalsinert malm ved XRF.
- Spesifikt overflateareal av kalsinert malm funnet via BET metode.
- Thermogravimetrisk analyse av kalsinasjon og reduksjonsprosessene.
- Elektronmikroskopi av den rå, kalsinerte og reduserte malmen.
- Grunnstoff fordelingen i den rå, kalsinerte og reduserte malmen, funnet via SEM-EDX.
- Røntgendiffraksjonsmønstre av den rå, kalsinerte og reduserte malmen.

Hovedfunnene i denne rapporten kan oppsummeres som:

- Polymetalliske noduler vil danne metallisk jern, nikkel og kobber når det blir redusert ved 900°C i et miljø med god tilgang på reduksjonsmidel av metan eller hydrogen. Faser av kobolt ble ikke identifisert, men vil teoretiskt sett også reduseres til en metallisk fase, og kan ha legert seg med et annet metall.
- Det ble ikke oppdaget karbider i noen av de reduserte prøvene.
- Manganoksid ble redusert til stadiet MnO.
- Silisium innholdet i de polymetalliske nodulene påvirker fasesammensettingen til de reduserte prøvene. Silisium går i fase med elementer av mangan og jern og danner faser av fayalitt og tefroitt.
- Aluminium i den reduserte prøven går i fase med silisium, natrium og kalium i nefelin.
- En økning i porositeten av polymetalliske mangannoduler under kalsinering tillater for enkel massetransport av reagenser og avgasser, noe som mulig kan tillate for prossessering uten et pelletiseringsstadie.
- Reaksjonshastigheten til reduksjone er høy og virker eksotermisk.

Table of Contents

1 Introduction

1.1 Motivation

The major shift towards sustainable development is causing strain on material supply. Battery technology, electrification, digitization, as well as other advanced materials have new requirements and the more widespread adoption of these places more and different demands on the value chain. Sub-sea mining has been explored to supply an industry with a growing demand for metals. Sub-sea minerals are usually rich in iron and manganese, with a high concentration of valuable elements such as nickel, copper, cobalt, and rare earth minerals. [1]

The field of sub-sea mining has been mostly investigated since the 1970's without any major progress towards realizing commercial extraction. Due to an increase in demand of valuable metals such as Cu, Co and Ni, largely caused by the major shift towards renewable energies combined with the increased importance placed of securing the supply of critical materials this field is once again experiencing heightened interest. The Clarion Clipperton Fracture Zone contains vast reserves of polymetallic nodules containing amounts of valuable metals rivaling the total amount of land resource which contain potentially useful amounts of these minerals, as well as Mn, Fe and other minerals. [2][3]

An article in Materials transactions titled "Forecasting of the Consumption of Metals up to 2050" concludes that with existing reserves, and even for some reserve bases it will be impossible to satisfy the projected demand. This demonstrates the need of renewed thinking regarding mineral reserves and the need for decoupling between extraction and consumption. Figure 1 is an extract from that report illustrating exactly the scale of the issue regarding resource scarcity. In this figure the blue bars extending downwards represents today's reserves and the red upper lines represent the reserve base adjusted so that today's reserves are set to 1 for the respective metals. The yellow upward extending bars indicate the accumulative consumption of the respective metals up to 2050. When the line marking 1 is crossed, that means that today's reserves are depleted, when the upper lines are crossed that means the reserve base is depleted. Viewing the relevant bars of Cu, Mn, Ni and Co it is apparent that these reserves are expected to become depleted, either completely or just the current reserves. The blue downward-extending bars indicates today's reserves. [4]
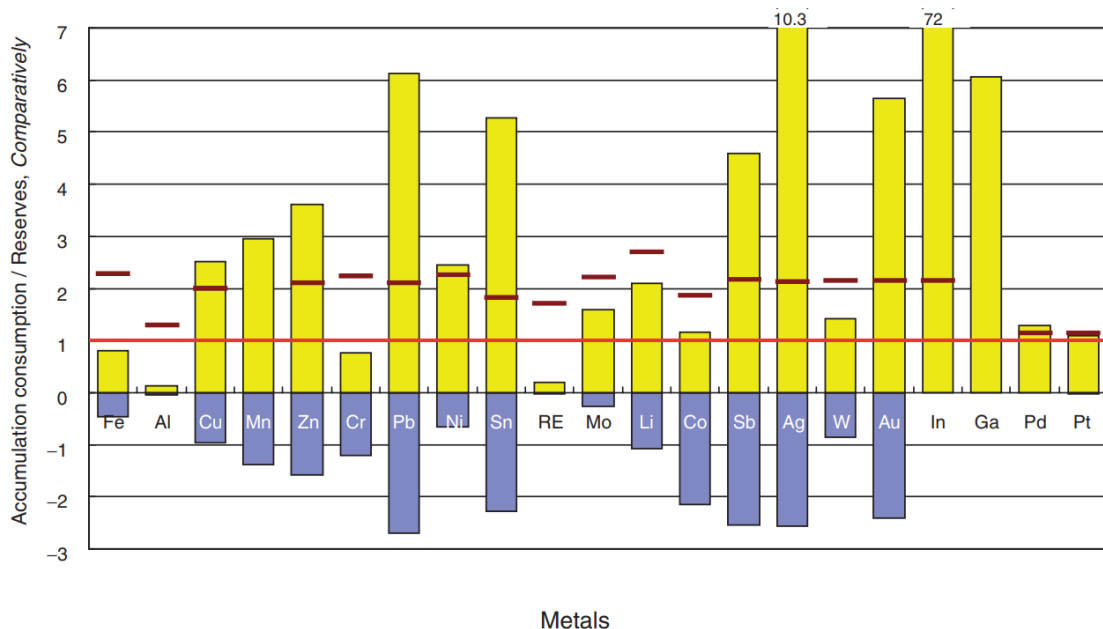

Figure 1: The relation between cumulative demand and existing reserves of metals by 2050

Another major development is the need to reduce the carbon footprint of metal production. To achieve the global climate goals set in the Paris Agreement, it is necessary to reduce carbon emissions. Carbon, mainly in the form of coal, has traditionally been the main reducing agent in metallurgical processes, this is cause of approximately 7% worlds CO_2 emissions as an off gas in the process [5]. As such the exploration of low carbon methods such as gaseous reduction is making headway in multiple metal production paths. The utilization of hydrogen and or methane as reactants due to their lower carbon emissions has been central to this exploration.

A move to a gas-based reactant can also reduce the logistical problems for example in the case of producing hydrogen locally via electrolysis. Thereby eliminating the need to transport the reactant. This plays into the move towards electrification of industry, where electricity replaces various resources increasing efficiency and reducing logistical complexity. However, the handling of gas introduces multiple complexities regarding safety during storage and handling [6]. Gas reactants and especially hydrogen is highly volatile and difficult to store. Examples of work to commercialize the use of gaseous reduction is HYBRIT a project by LKAB, Vattenfall and SSAB. This project plans to use hydrogen as reducing agent and hopes to supply the market with fossil-fuel free steel by 2030 and has recently received funding from the EU Innovation fund [7].

For the reduction of other metals such as manganese it might be necessary to introduce other gases or methods such as aluminothermic reduction to achieve full reduction of the metal ore. Such as in a new established process based on experimental work, the HAlMan process, manganese is produced from primary sources via the combination of hydrogen reduction to MnO and further aluminothermic reduction of MnO from molten slags to Mn metal at elevated temperatures [8].

The field of sub-sea innovation is center stage for Norwegian industry as of today. A large part of the economy is centered around offshore oil and gas. Seeing that a stated goal of the Norwegian government is to diversify its economy, and to reduce its dependency on oil and gas [9], it should be of interest to apply the existing expertise in Norwegian industry within the field of subsea innovation to achieve this diversification.

The positioning of Norway as a potential lead player in the field of subsea mining is not only reserved to the existing expertise, but also the existence of abundant subsea mineral deposits within the Norwegian exclusive economic zone. Rystad Energy estimates that there is an occurrence of subsea minerals of a value of 180 bNOK yearly within its exclusive economic zone. [10]

1.2   Objectives of research

The objective for this research is to perform a series of reduction experiments utilizing different reduction agents. Performing characterization of the polymetallic nodules at the different stages raw, calcined and reduced, and gaining insight into the mechanisms of reduction of the polymetallic manganese nodules.

Characterizations useful for this paper is the analysis of chemical and phase composition of the nodules at various process stages such as raw, calcined and reduced. The porosity and surface area of the ore is also of interest as to give insight into specific surface area, as this is important for mass transport during reduction, and may be of interest in future reduction experiments of ore of a similar type.

An ideal result of this research is the contribution of research to a developing field. Aiding in producing valuable knowledge for the possible expansion of a new field of industry of subsea mining, as well as contributing to the decarbonization of the metallurgy field.

2 Literature review

2.1 Polymetallic manganese nodules

Polymetallic nodules have been confirmed to occur at various abyssal planes. Due to their formation mechanism they tend to form at depths of around 4000-6000 meters. Some known locations are the Clarion Clipperton zone (CCZ), Peru basin, Gulf of Cadiz, Baltic Sea and Fiji basin. The nodules are assumed to be highly prevalent, with estimates of 21 billion tons in the Clarion Clipperton zone alone. Manganese nodules and manganese crusts form in the abyssal planes within silicious ooze shortly below the carbonate compensation depth, where water mineral composition is high. Silicious ooze is described as containing carbonate, opal-A and some quartz [11]. Deeper formations tend to be smaller, due to less ideal conditions leading to slower formation. The nodules have three growth mechanisms: hydrogenetic, diagenetic, and hydrothermal precipitation. Minerals in the CCZ tends to form via a combination of hydrogenetic and diagenetic.[3]

Hydrogenetic precipitation is a process of Mn and Fe precipitating onto hard surfaces. This is a vital step in the formation of manganese nodules, and will in normal conditions form $Mn^{4+}O_2$, and $Fe^{3+}OOH$. With this mechanism, ions of $Co^{2+}, Ni^{2+}, Zn^{2+}, Ti^+$ tend to adsorb onto the MnO_2 particles, while negative complexes such as carbonate, hydroxide, or oxyanion complexes adsorb onto the $Fe^{3+}OOH$. When the two colloids' precipitates onto a surface, they usually form a hydrogenic ferromanganese crusts with high internal surface area, enabling high enrichment of seawater minerals, up to a factor of 109. Phases formed by this formation mechanism tend to have a Mn/Fe ratio of >5. This growth mechanism is also the main mechanism in manganese crusts, which is another form of subsea mineral. The resulting mineral formed via this mechanism is a form of hydrogenetic layers, often in the form of vernadite. [3][12]

The second formation mechanism is diagenetic, which is the process of precipitation in or on the sediment surface caused by microbial activity. This process is controlled by oxidation of organic material on the seafloor and is a source of energy for microorganisms living in this environment. Layers formed utilizing this mechanism has a high Mn/Fe ratio, up to 800, as the manganese and iron reduction processes won't occur simultaneously. This mechanism tend to form properly crystalline phyllomanganates such as birnessite or buserite. [3]

The third is caused by the precipitation of minerals of hydrothermal fluids. As hydrothermal vents with warmer and more acidic water solves manganese within the ocean crust and vents it in the hydrothermal plumes. When the solved manganese ions mix with the colder, oxic water, it oxidizes, precipitates, and becomes deposited onto the seafloor, either forming manganese crusts, or enriching the sediments in which the manganese nodules grow.[3]

Manganese nodules consist of various mineralogical phases. Some characteristic phases are vernadite 7Å/10Å, Fe-vernadite all with the chemical formula $(Mn^{4+}, Fe^{3+}, Ca, Na)(O, OH)_2 \cdot nH_2O$ the Fe-vernadite being rich in iron, 7Å birnessite, 10Å buserite both with formula $MnO_2 \cdot nH_2O$, asbolane with formula $Mn^{4+}(O, OH)_2 \cdot (Co, Ni, Mg, Ca)_X(OH)_{2X} \cdot nH_2O$, chalcophanite $ZnMn_3^{4+}O_7 \cdot H_2O$, lithiophorite $(Al, Li)Mn^{4+}O_2(OH)_2$ and todorokite $(Na, Ca, K, Ba, Sr)_{1-x}$ $(Mn, Mg, Al)_6O_{12} \cdot 3 - 4H_2O$. The 7Å/10Å indicates the interlayer distance being either 0,7nm or 1,0 nm of the phyllomanganates which is a microporous structure. Manganese nodules have a high rate of interstitial atoms and a unique variety of phases, due to its formation mechanism. This causes issues when analyzing an XRD diagram in two ways. One is that the interstitial atoms cause strain on the structure, this causes the peaks to become less sharp and widen or shift. The other is the presence of multiple phase [13][3]

The composition of manganese nodules tends to vary widely, an analysis based on various studies fund the compositions described in table 1. Here samples retrieved from various parts of the Clarion Clipperton Fraction Zone have been analyzed. The composition is not properly understood by only analyzing the phase composition due to the high rate of interstitial atoms, which is what gives the high rate of valuable elements.[3]

Table 1: Chemical composition of polymetallic manganese nodules from the Calarion Clipperton Zone

Source: Deep-Sea Mining [3]

Element	CCZ (a) Mean	N	Eastern CCZ (b) Mean	N	Central CCZ (b) Mean	N
Fe (%)	6.16	66	6.3	575	6.1	17
Mn	28	66	31.4	575	27.56	39
Si	6.55	12	6.04	523	7.49	39
Al	2.36	65	2.29	523	27.1	39
Mg	1.89	66	1.94	575	2	39
Ca	1.70	66	1.68	575	1.68	39
Na	1.99	66	2.19	575	20.4	39
K	0.99	66	0.97	575	1.09	39
Ti	0.32	66	0.26	566	0.33	39
P	0.21	66	0.15	575	0.21	39
Cl	0.27	12	0.7	497	0.46	27
LOI	26.50	12	15.2	497	15.1	27
H2O−	11.60	12	-	-	-	-
H2O$^+$	8.80	7	-	-	-	-
CO2	-	-	-	-	-	-
ST	0.17	12	0.16	497	0.1	-
Ag (ppm)	0.17	12	-	-	-	-
As	67.00	12	83	497	65	27
Au (ppb)	4.50	9	-	-	-	-
B (ppm)	-	-	-	-	-	-
Ba	3500	66	4304	566	2280	39
Be	1.9	12	-	-	1.9	18
Bi	8.8	12	8.4	600	7.25	3
Br	-	-	-	-	-	-
Cd	16	12	-	-	-	-
Co	2098	66	1738	575	2501	39
Cr	17	12	14	9	18	4
Cs	1.5	61	1.34	566	1.51	18
Cu	10.714	66	11.79	575	10.81	39
Ga	36	12	25.7	45	-	-
Ge	-	-	-	-	-	-
Hf	4.7	66	4.53	565	4.51	39
Hg (ppb)	18	3	-	-	-	-
In (ppm)	0.27	12	-	-	-	-
Li	131	66	133	566	123	39
Mo	590	66	622	567	556	39
Nb	22	66	18.7	566	21.3	39
Ni	13.002	66	14.01	575	13.57	39
Pb	338	66	276	566	358	39
Rb	23	66	20.2	566	25.2	39
Sb	41	12	75	90	19	5
Sc	11	66	10.1	566	12	39
Se	0.72	12	-	-	-	-
Sn	5.3	12	-	-	-	-
Sr	645	66	701	575	592	39
Ta	0.33	66	0.27	559	0.33	39
Te	3.60	66	3.57	528	3.85	23
Tl	199	12	-	-	-	-
Th	15	66	11.5	566	17.7	39
Continued on next page						

Table 1 – continued from previous page

Element	Mean	N	Mean	N	Mean	N
U	4.2	66	3.78	566	3.79	39
V	445	66	717	575	486	39
W	62	66	64.3	566	55	39
Y	96	66	78.9	566	105	39
Zn	1366	66	1544	566	1228	39
Zr	307	66	302	566	287	39
La	114	66	101	566	109	39
Ce	284	66	242	566	270	39
Pr	33.4	66	29.7	566	33.3	39
Nd	140	66	120	566	137	39
Sm	34	66	29.8	566	33.9	39
Eu	8.03	66	7.3	566	8.26	39
Gd	31.8	66	29.3	566	32.6	39
Tb	4.98	66	4.45	566	5.05	39
Dy	2.85	66	25.7	566	29.2	39
Ho	5.35	66	4.69	566	5.37	39
Er	14.6	66	13	566	14.9	39
Tm	2.11	66	1.79	566	2.05	39
Yb	13.7	66	12.5	566	17.7	39
Lu	2.05	66	18.4	566	2.03	39
Ir (ppb)	2	11	-	-	-	-
Os	-	-	-	-	-	-
Pd	8	12	-	-	-	-
Pt	128	12	0.11	7	-	-
Rh	9	12	-	-	-	-
Ru	12	12	-	-	-	-
Σ REY (ppm)	813	-	701		801	-
Σ HREY	199	-	172	655	210	-
Element ratios						
Mn/Fe	4.61	66	5.15	575	4.52	39
Co$^+$Cu$^+$Ni(%)	2.58	66	2.75	575	2.69	39
Y/Ho	17.94	66	16.9	566	19.54	39
Zr/Hf	65.32	66	67.20	566	63.64	39
Th/U	3.57	66	3.04	566	4.67	39
Ce/Ce*	1.05	-	1.01	-	1.02	-

Units of elements: Fe-ST: [%], the rest is [ppm] if not otherwise stated

(a) Hein et al. [14]

(b) German Federal Institute for Geosciences and Natural Resources (BGR) data

N indicates the number of analyzed samples. Ce/Ce* = $Ce_{SN}/(0.5La_{SN}+0.5P_{rSN})$

SN = Shale normalization with data from Lipin & McKay, 1989 [15]

2.2 Extraction of metals, hydrometallurgy and pyrometallurgy

The two main methods to extract metal from ore are hydrometallurgy and pyrometallurgy. Hydrometallurgy separates and extracts metals from the ore using aqueous reactions. Hydrometallurgy involves 3 steps; leaching to separate the metals from the ore, solution purification to remove unwanted ions from the solution, and metal recovery to extract the desired metal species from the solution. [16]

Pyrometallurgy is processing of ore at high temperatures to convert the ore into metals. The main steps are to convert carbonates, hydroxides, sulfides and sulphates in the ore into oxides and remove volatile substances either through roasting or calcination, refining to remove impurities, and smelting to reduce and extract the desired products. [17]

Pyrometallurgy and hydrometallurgy, with and without a precoursor step of pyrometallurgy have been applied as processing paths for metal extraction from polymetallic nodules [18]. While Co, Ni and Cu recovery are important, extraction of Mn have received less attention by the previously developed processes [18]. Several different methods have been explored with their own advantages and disadvantages. For hydrometallurgical routes the main disadvantage is the high consumption of chemicals, and leach residue [19], and for pyrometallurgical routes it is the energy intensive processes due to the need for high temperatures.

Sommerfeld et al. investigated a pyrometallurgic route for "Zero-Waste" involving two reduction steps [19] based on the process from INCO [18]. It was discovered that 90%-100% of Co, Ni, Cu and Mo could be extracted into a metal phase, while over 97% of Mn and most of the Fe remained in the slag to be extracted further as ferromanganese in the second reduction step. It was emphasized that further studies and a scale up is necessary. [19]

2.3 Gaseous reduction of manganese ore

2.3.1 Reaction kinetics

The use of gaseous reduction agents in metal production has received a lot of interest over the past few years. Using a gaseous reduction agent is similar to solid state processes determined by the reaction equilibrium and mass transport through the ore, making the permeability and surface area important factors in the process [20]. However, gaseous reduction has the benefit of being able to adjust the flow rate, potentially replenishing the atmosphere and shifting the equilibrium in the favor of reduction by adding inert gas to the gas flow, increasing the total flow rate. The ability to change different parameters gives more control over the process compared to the traditional method. Polymetallic nodules are as mentioned porous with a high surface area making gaseous reduction agents a viable choice. [3]

At temperatures above 550°C it is thermodynamically possible for methane to decompose into solid carbon and hydrogen gas (methane cracking) as shown in Equation (1). If the concentration of methane is too high it may have a detrimental effect for reduction purposes as methane cracking can form a soot layer on the surface. This layer reduces the available surface area and is hindering to further reduction of the material [20]. Methane cracking introduces solid carbon into the system making carbon a possible reducing agent, as well as the possibility for carbides to form.

The reduction of Manganese ore from MnO_2 to Mn goes through 4 steps as shown in Equation (2) - (5). Methane can be used as a reducing agent as Equation (6) shows, producing CO and H_2 as an off gas. These can also be used as reducing agents shown in Equation (7) and (8) respectively. Another possible reducing agent is solid carbon through the reaction shown in Equation (9). Figure 2 is an Ellingham Diagram created by HSC Chemistry 9 using Equation (2) - (9), and shows that MnO_2 can be reduced to MnO by methane from about 390°C, but that a full reduction to Mn isn't possible at temperatures below 1000°C.
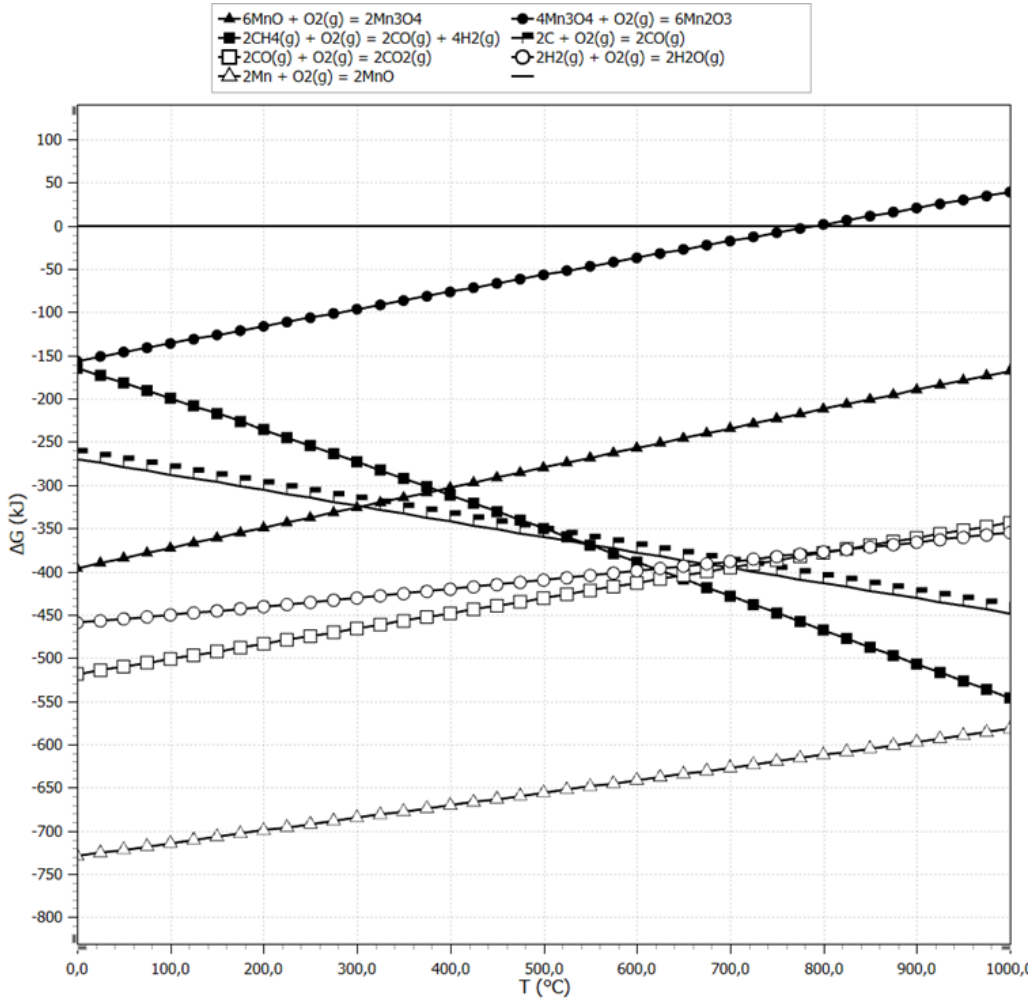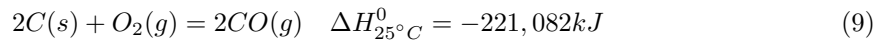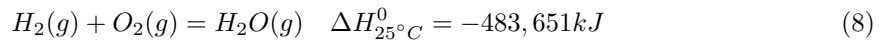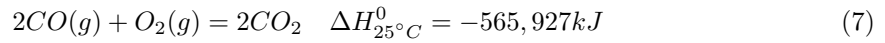
$$CH_4(g) = C_{soot} + 2H_2(g) \quad \Delta H^0_{25°C} = 74,600kJ \tag{1}$$

$$4MnO_2(s) = 2Mn_2O_3(s) + O_2(g) \quad \Delta H^0_{25°C} = 162,3kJ \tag{2}$$

$$6Mn_2O_3(s) = 4Mn_3O_4(s) + O_2(g) \quad \Delta H^0_{25°C} = 212,400kJ \tag{3}$$

$$2Mn_3O_4(s) = 6MnO(s) + O_2(g) \quad \Delta H^0_{25°C} = 459,474kJ \tag{4}$$

$$2MnO(s) = 2Mn(s) + O_2(g) \quad \Delta H^0_{25°C} = 770,441kJ \tag{5}$$

$$2CH_4(g) + O_2(g) = 2CO(g) + 4H_2(g) \quad \Delta H^0_{25°C} = -71,883kJ \tag{6}$$

$$2CO(g) + O_2(g) = 2CO_2 \quad \Delta H^0_{25°C} = -565,927kJ \tag{7}$$

$$H_2(g) + O_2(g) = H_2O(g) \quad \Delta H^0_{25°C} = -483,651kJ \tag{8}$$

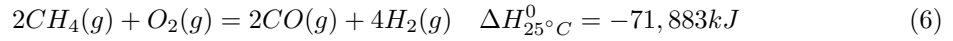$$2C(s) + O_2(g) = 2CO(g) \quad \Delta H^0_{25°C} = -221,082kJ \tag{9}$$
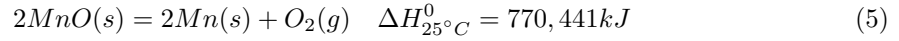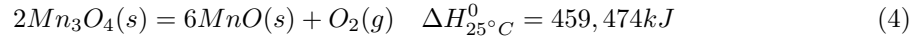

Figure 2: Ellingham diagram showing the reaction of manganese oxides and oxidation of C, H_2 and CH_4 Gibbs free energy of the reactions as a function of temperature for the reduction of manganese. Calculated using the Reaction Equations module in HSC Chemistry 9.

The reduction of Fe_2O_3 to Fe is shown in Equation (10) - (12). Figure 3 is an Ellingham Diagram created by HSC Chemistry 9 using Equation (6) - (12), and shows that the full reduction to Fe is possible from about 650°C with methane. As metallic iron is produced, the formation of iron carbides are a possibility, Equation (13) - (15). Figure 4 is an Ellingham Diagram created by HSC Chemistry 9 using Equation (13) - (15), and shows that methane will start to crack at temperatures above approximately 550°C. This produces the carbon necessary for iron carbides to start forming at temperatures above approximately 890°C.

$$6Fe_2O_3(s) = 4Fe_3O_4(s) + O_2(g) \quad \Delta H^0_{25°C} = 486,691kJ \tag{10}$$

$$2Fe_3O_4(s) = 6FeO(s) + O_2(g) \quad \Delta H^0_{25°C} = 640,681kJ \tag{11}$$

$$2FeO(s) = 2Fe(s) + O_2(g) \quad \Delta H^0_{25°C} = 530,105kJ \tag{12}$$

$$3Fe(s) + C(s) = Fe_3C(s) \quad \Delta H^0_{25°C} = 27,000kJ \tag{13}$$

$$5Fe(s) + 2C(s) = Fe_5C_2(s) \quad \Delta H^0_{25°C} = 54,782kJ \tag{14}$$

$$7Fe(s) + 3C(s) = Fe_7C_3(s) \quad \Delta H^0_{25°C} = 81,210kJ \tag{15}$$
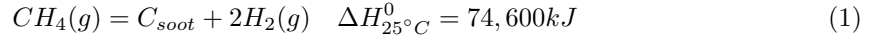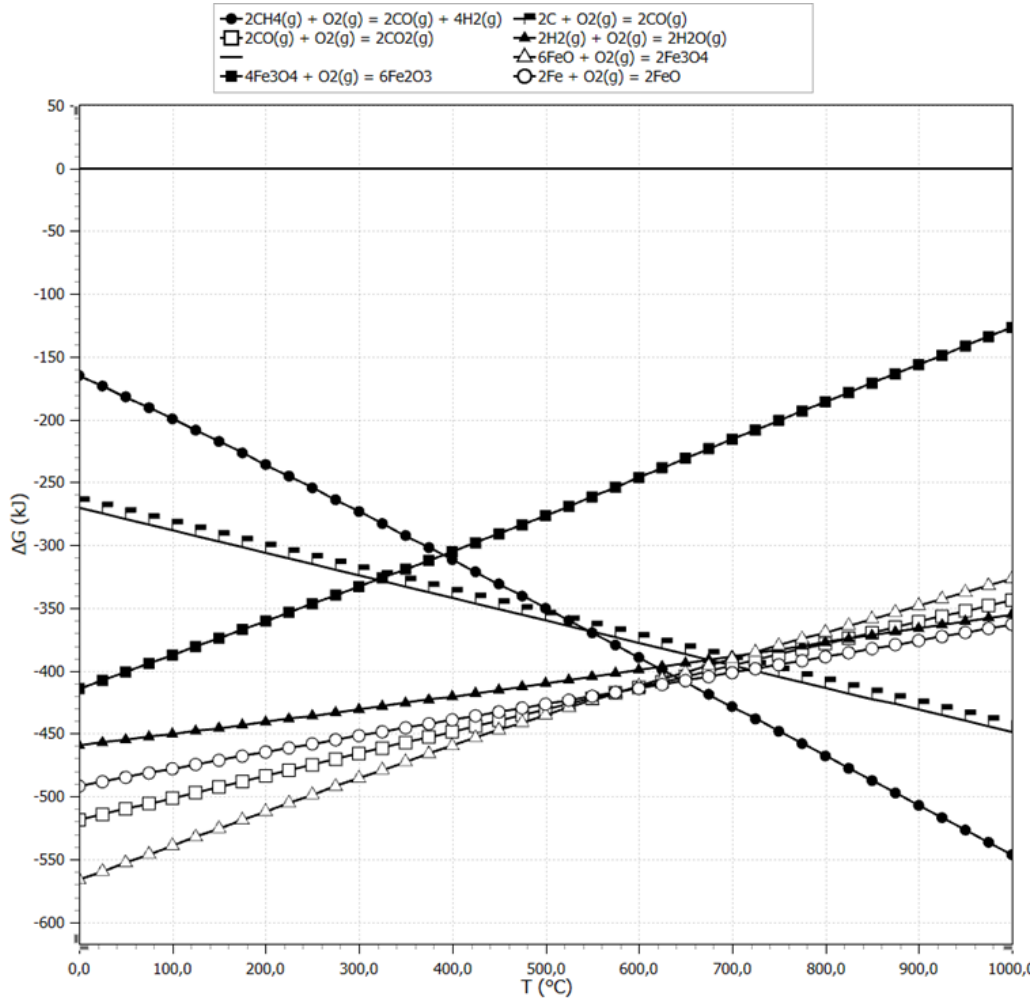

Figure 3: Ellingham diagram showing the reaction of iron oxides and oxidation of C, H_2 and CH_4 Gibbs free energy of the reactions as a function of temperature for the reduction of iron. Calculated using the Equation Reactions module in HSC Chemistry 9.

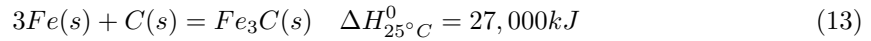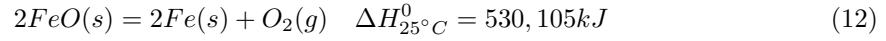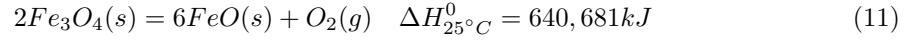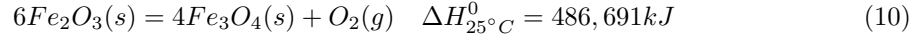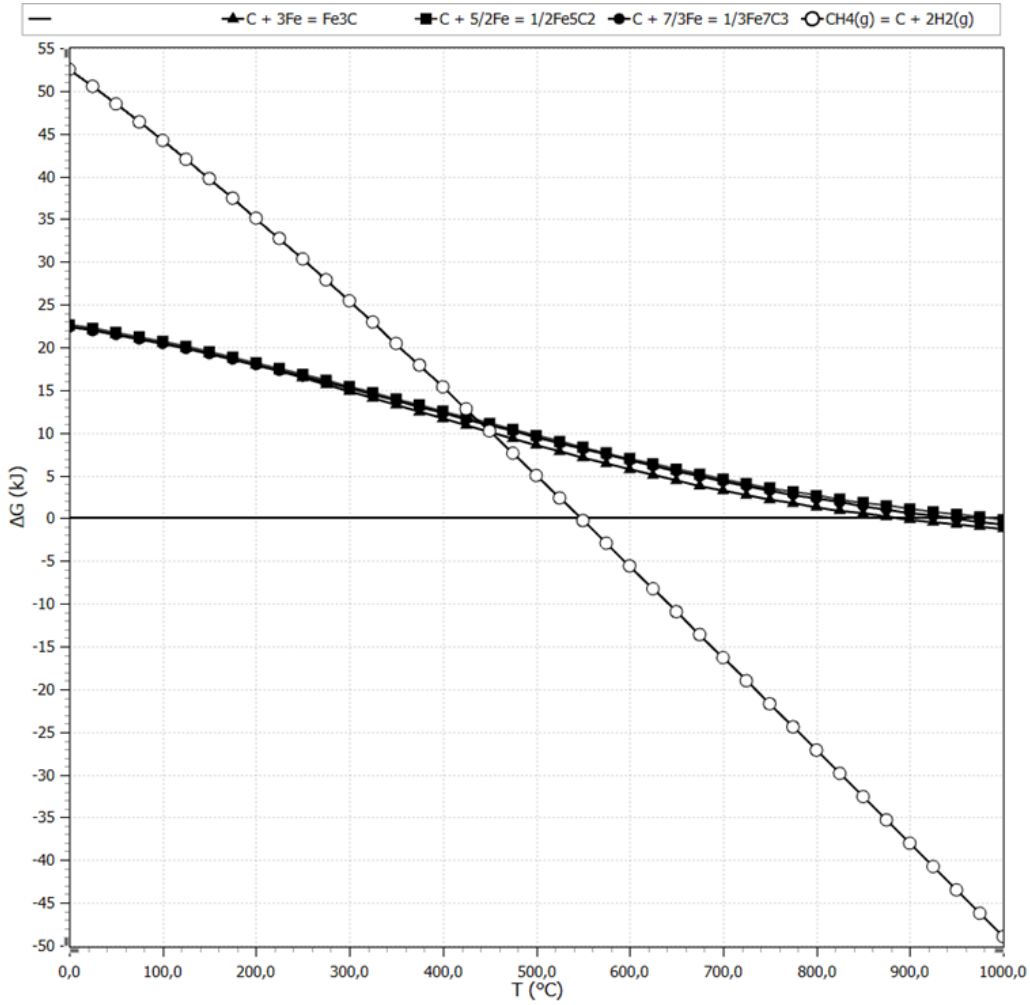Figure 4: Ellingham diagram showing the reaction Gibbs free energy of the formation of iron carbides and methane cracking. Calculated using the Equation Reactions module in HSC Chemistry 9.

The reduction of Co_3O_4 to Co, NiO to Ni and CuO to Cu is given in Equation (16) - (17), (18) and (19) respectively. Figure 5 is an Ellingham Diagram created by HSC Chemistry 9 using Equation (6) - (12), and shows that a full reduction of cobalt is thermodynamically possible at temperatures above $520°C$, Ni at temperatures above $475°$ and copper at temperatures above $175°$ with methane.

$$2Co_3O_4(s) = 6CoO(s) + O_2(g) \quad \Delta H^0_{25°C} = 409,935kJ \tag{16}$$

$$2CoO(s) = 2Co(s) + O_2(g) \quad \Delta H^0_{25°C} = 475,888kJ \tag{17}$$

$$2NiO(s) = 2Ni(s) + O_2(g) \quad \Delta H^0_{25°C} = 479,399kJ \tag{18}$$

$$2CuO(s) = 2Cu(s) + O_2(g) \quad \Delta H^0_{25°C} = 310.384kJ \tag{19}$$
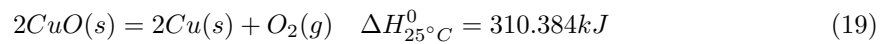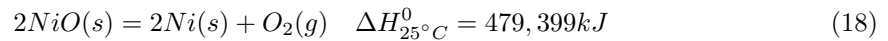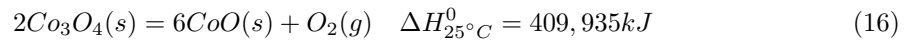
Figure 5: Ellingham diagram showing the reaction of cobalt, nickel and copper oxides and oxidation of C, H_2 and CH_4 Gibbs free energy of the reactions as a function of temperature for reduction of cobalt, nickel and copper. Calculated using the Equation Reactions module in HSC Chemistry 9.

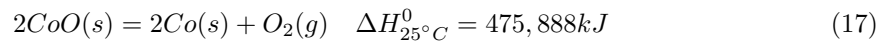### 2.3.2 Literature findings

The effect on reduction of manganese oxides by methane-containing gas have been studied by N. Anacleto et al. in the temperature range of 1000-1200°C. It was found that under a 20vol% H_2 and 80vol% Ar gas mixture MnO_2 reduced to MnO at 620°C, without sign of further reduction at higher temperatures. When 10vol% CH_4 gas was introduced (10vol% CH_4, 20vol%H_2 and 70vol%Ar) MnO started to reduce to manganese carbides at 760°C and the reduction completed at about 1200°C. Several experiments were performed with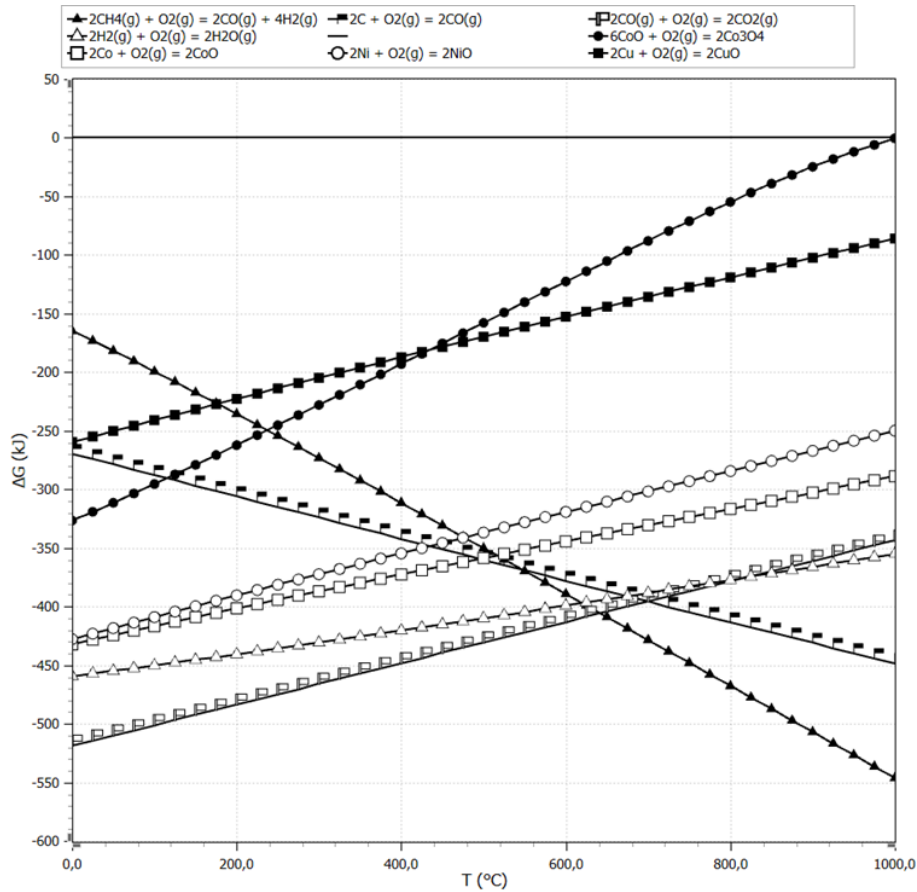 varying gas compositions and temperatures. The findings show that an increase in temperature, a methane concentration up to 10-15vol% and increasing the hydrogen concentration above 20vol% favors the reduction of MnO to Mn_7C_3. The addition of Fe_3O_4 to the MnO mixture was also found to have a positive effect on the reduction speed, while the addition of CO to the gas composition were found to have a strong retarding effect on the reduction of MnO. [21]

A. Cheraghi et al. also studied the kinetics and mechanism of low-grade manganese ore reduction by natural gas. Calcination under a gas flow of 1 NL Ar followed by reduction under 1 NL CH_4 and 1NL Ar were conducted at 700°C, 800°C, 900°C and 1000°C. XRD analysis of the calcined ore show that with increasing temperatures the intensity of $(Mn, Fe)_2O_3$ and Mn_2O_3 peaks decreased in favor of $(Mn, Fe)_3O_4$ and Mn_3O_4. The intensity of CaO also increased with increasing temperature. XRD analysis of the reduced ore showed that increase in temperature gave higher intensities for $(Fe, Mn)_3C$, CaO and $2MnO \cdot SiO_2$. MnO also saw an increase with increasing temperature, however, at 1000°C the intensity decreased. The intensity of SiO_2 also decreased at higher temperatures. [22]

A. Cheraghi et al. have also conducted a literature study of gaseous reduction of manganese ore. Their findings include that a reduction of MnO is possible with CH_4, but not with CO or H_2, that using a mixture of H_2 and CH_4 reduces methane cracking, and that reduction happens at lower temperatures than in a submerged arc furnace. [20]

2.4   Selected methods for ore reduction studies

2.4.1   Thermogravimetric Analysis

Thermogravimetric analysis or TGA is a method of analysis where the mass change as a function of temperature is measured. The instruments required for such an analysis is a precision scale and a temperature controlled environment such as a furnace. Periferal elements could be the use of atmospheric control in order to measure the effect of reactants on a sample. Data collected from a TGA presents the total weight loss for a sample as a function of temperature, as well as the rate of mass loss as a continuous function. When the weight loss curve drops it indicates the start of a decomposition reaction, and when the curve levels out the reaction is ending. There are multiple factors that influence the data collected from a TGA, namely the heating rate, the crucibel, and the atmosphere. In addition the TGA analysis is highly sensitive to external factors such as vibration. The heating rate of the TGA should be as low as to not blur possible multiple and limit the effect of possible exothermic or endothermic reactions. This has the benefit of also separating different stages of the reaction. The crucible geometry and material can in large part affect the collected data and TGA crucibles have been designed in order to avoid possible mass changes such as pressure-buildups or condensation. The atmosphere can induce reactions or may adsorb onto the crucible or material, which in some cases is intended. The operator of the TGA-device should be aware of this effect as not to accidentally affect their results. [23]

2.4.2   X-ray diffraction

X-ray diffraction or XRD is described by Encyclopaedia Britannica as "a phenomenon in which the atoms of a crystal, by virtue of their uniform spacing, cause an interference pattern of the waves present in an incident beam of X-rays"[24]. This interference pattern is characteristic of different crystal structures and is determined by Bragg's law as shown in equation 20. This phenomenon becomes highly useful for identifying phases in a sample as the spacing of different crystal structures are unique giving different patterns. The XRD pattern is commonly presented as a graph of intensity versus 2θ.

$$2d \times sin(\theta) = n \times \lambda \tag{20}$$

Although the patterns are unique to each crystal they can be very similar and may need supplementing data, such as element composition and distribution, or processing data. Strain in the sample could effect the diffraction pattern. Uniform strain can shift the pattern from side to side, and non-uniform strain can cause a widening of the peaks. The presence of substitution-elements or solid solutions in the crystal structure may induce strain. Solid solutions may also cause a phase with an intermediary diffraction pattern. Another factor that may shift the pattern left or right is alignment within the diffractometer. In addition to this when analyzing complex samples they may contain multiple phases, this will result in a pattern where the peaks are stacked. When working with such stacked patterns, a factor to be cognisant of is that XRD is a qualitative analysis method and the amount of a phase cannot be directly interpreted from the interference pattern. There is however a correlation between the prominence of a peak pattern an the phase composition, for example if a phase is not of sufficient quantity, it will not produce a sufficient pattern to be distinguished from background noise. [25]

2.4.3 X-ray fluorescence

Fluorescence is described by Encyclopaedia Britannica as "emission of electromagnetic radiation, usually visible light, caused by excitation of atoms in a material, which then re-emit almost immediately (within about 10^{-8} seconds)" [26]. X-ray fluorescence utilizes and the characteristic fluorescence spectrum of the elements contained within a sample in order to chemically analyze it.

2.4.4 Scanning electron microscope

Scanning electron microscope or SEM is defined by Encyclopaedia Britannica as a "type of electron microscope, designed for directly studying the surfaces of solid objects, that utilizes a beam of focused electrons of relatively low energy as an electron probe that is scanned in a regular manner over the specimen" . A scanning electron microscope can image a material surface by detecting various methods. Secondary electrons are ideal for topography as it nearly does not penetrate the sample surface and as well as the secondary electrons being produced in such a manner as to highlight topography. Where concave surfaces will emit less electrons and therefore be darker, and convex surfaces will emit more electrons and be brighter. Another method is backscattered electrons, this is useful for identifying elements. The detected electrons are backscattered due to the electric charge of the nucleus of the atoms imaged. The higher atom number gives higher electric charge and therefore appears brighter on the image. [27]

2.4.5 Energy dispersive X-ray

Energy dispersive x-ray also known as EDX is a SEM imaging method similar to XRF where the characteristic x-rays of the analyzed sample can be used to chemically analyze a sample. EDX however, can be used to collect data on points, lines, maps or an average of the scanned surface. This method is usually performed alongside SEM. In order to give greater insight into element distribution on the surface of the sample. The EDX detector measures the energy of the photons in the x-ray spectrum which are generated in a penetrating volume in the sample by the scanning electrons similar to as what is shown in figure 6. Due to this volume penetrating into the sample and expanding outwards, the resolution of EDX is not as high as the other imaging methods. [28]
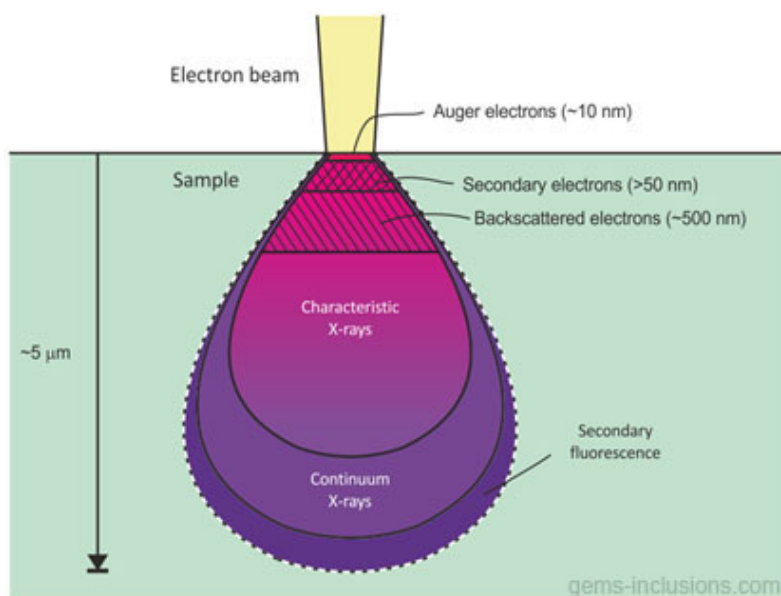

Figure 6: Interaction volume of SEM by different detection method illustrated in a cross section of a sample.

Source: Gems-inclusions.com [29]

2.4.6 BET

BET is the abbreviation of Brunauer, Emmet, and Teller who are the three scientists which developed this method of analyzing the specific surface area of a sample by building upon the Langmuir Isotherm. The BET method utilizes adsorption of a probing gas usually nitrogen and calculates the surface covered. The BET model which is a model that describes the amount of gas as a function of the relative pressure P/P_0, and is described in Equation 21. Where $n_{adsorbed}$ is the number of adsorbed atoms, n_m is amount of adsorbed atoms in a single layer. C is a constant dependant on the relation between the adsorption strength of the first layer and the vaporization enthalpy of the liquid adsorbate, P is the variable pressure, and P_0 is the saturated vapour pressure of the adsorbate. [30]

$$\frac{n_{adsorbed}}{n_m} = (C \times P/P_0)/((1 - P/P_0)(1 + (C - 1) \times P/P_0)) \tag{21}$$

3 Experimental procedure

3.1 Materials

The ore used in this bachelor project was bought and provided by the Department for Material Science and Engineering at the Norwegian University of Science and Technology. The ore originates from the CCZ. The supplier provided a compositional analysis of the ore through XRF. This composition is presented in Table 2.

Table 2: XRF data from the supplier.

Compound	wt%
MnO	40.03
SiO_2	17.92
Al_2O_3	6.73
CaO	2.22
MgO	3.44
K_2O	1.20
SO_3	0.53
P_2O_5	0.45
Fe_2O_3	4.18
TiO_2	0.38
Ni	1.00
Cu	1.00
Co	0.2
Ba	0.3

As Table 2 shows, the ore contains small amounts of phosphor. Due to this, extra safety measurements were taken during some of the experiments to make sure there was no formation of phosphine gas. This was done using a handheld phosphine detector and Dräger tubes under fume hood. Further information is provided in Appendix A.

The polymetallic manganese nodules studied in this thesis are shown in Figure 7.

Figure 7: Polymetallic manganese nodules studied for this thesis.

Beyond the polymetallic nodules which were analyzed, the equipment used for this thesis was:

- Retsch RS200 Vibratory Disc Mill
- Nabertherm HTCT 01/16 Muffle furnace
- Memmert UN55 convection oven
- Fume hood
- Dräger Tubes
- Ventis MX4 Muli Gas Detector
- XRF – performed by Degerfors Laboratories
- Linseis - STA PT 1600 - TGA 2017
- Thermal Technology LLC – 1000-3560-FP20 – ReSiNa
- Rikagu MiniFlex 600 XRD
- PowDLL Converter
- Diffrac.eva software
- CitoPress mounting press
- Polyfast
- Epofix
- ATM Saphir 330, Struers RotatoPol
- SC7620 Mini Sputter/ Glow Discharge System
- JEOL JCM 6000
- Micrometics, Degas sample dryer
- Micrometics, 3 Flex 3500, BET
- HSC Chemistry 9

3.2 Calcination

The ore were calcined in the state it was obtained, this means a size distribution around 7-40 mm in diameter. A portion of the ore was crushed in order down to a size between 4-15 mm, however as the ore is quite porous this resulted in a lot of material waste. Combining the effects of waste and porosity it was deemed unnecessary to crush the ore for further experiments. The calcination was performed using the Nabertherm HTCT 01/16 muffle furnace. The calcination program was set to 900°C for 2 hours, with a heating rate of 20°C/min. After the calcination the sample were left to cool overnight in the furnace. The sample was exposed to air for the entire calcination.

A test batch was run as the same settings under a fume hood in order to test for the possibility of phosphine formation. Neither Dräger tubes nor the handheld gas detector could detect any phosphine. However, as trace amounts of SO_2 were detected it was deemed safer to perform the rest of the calcination under a fume hood as well. Due to the size of the furnace the calcination was performed in multiple steps with several crucibles at a time.

3.3 Redcution in stationary bed

The reduction experiments were carried out in a Thermal Technology LLC – 1000-3560-FP20 – ReSiNa Furnace. The reduction experiments were carried out under 4 different gas compositions. The gas compositions are given in Table 3 together with the mass of the sample and the temperature.

Table 3: The various reduction setups in ReSiNa furnace (and TGA).

Experiment	$Ar/CH_4/H_2$ [%]	Sample weight [g]	Temperature [°C]
1	50/50/0	49.75	1160
2	0/0/100	49.72	1015
3 (TGA)	0/0/100	1.79	900
4	10/50/40	50.19	860
5	40/50/10	49.18	860
6	50/50/0	50.41	860

The reduction experiments were planned to be performed at 1100°C with a gas flow at 2NL/min. A thermocouple was used to measure the temperature inside the crucible with the sample. In order to ensure proper atmosphere, the furnace was flushed with argon, then purged by vacuuming to a pressure of 170 mTorr, before being flushed back to atmospheric pressure with argon. Reduction gas was only applied when the furnace reached the working temperature.

The temperature in the crucible was expected to give lower temperature than the programmed furnace temperature. Therefore a test with an empty furnace was programmed to reach 1160°C, but the furnace overshot to a temperature 1250°C in the crucible as shown in 8. Therefore, the first experiment was set to run at 1050°C with an atmosphere of 50% Ar, 50%CH_4. This experiment reached a temperature of roughly 1160°C in the crucible. Approximately 10 minutes after applying methane-gas the pressure in the furnace began increasing, and the experiment was aborted. The cause of the pressure increase was discovered to be clogging of the valves because of methane cracking. Therefore, the new reduction parameters were set to 900°C with a gas flow of 2NL/min. In the following experiment the furnace programmed to a max temperature of 850°C with a 100%H_2 atmosphere. The thermocouple overshot and reached a temperature of 1016°C as shown in Figure 9, but there were no other issues during the reduction. However, to compare more similar samples, the sample reduced in the TG analysis was used instead of the 100%H_2. To avoid methane cracking in the following experiments they were programmed with a temperature profile with 750°C as peak temperature, leading to the temperature stabilizing around 860°C. The temperature profile for the experiments at 860°C is given in Figure 10. The temperature profile of the reduction was recorded. However much of the data was lost or corrupted.
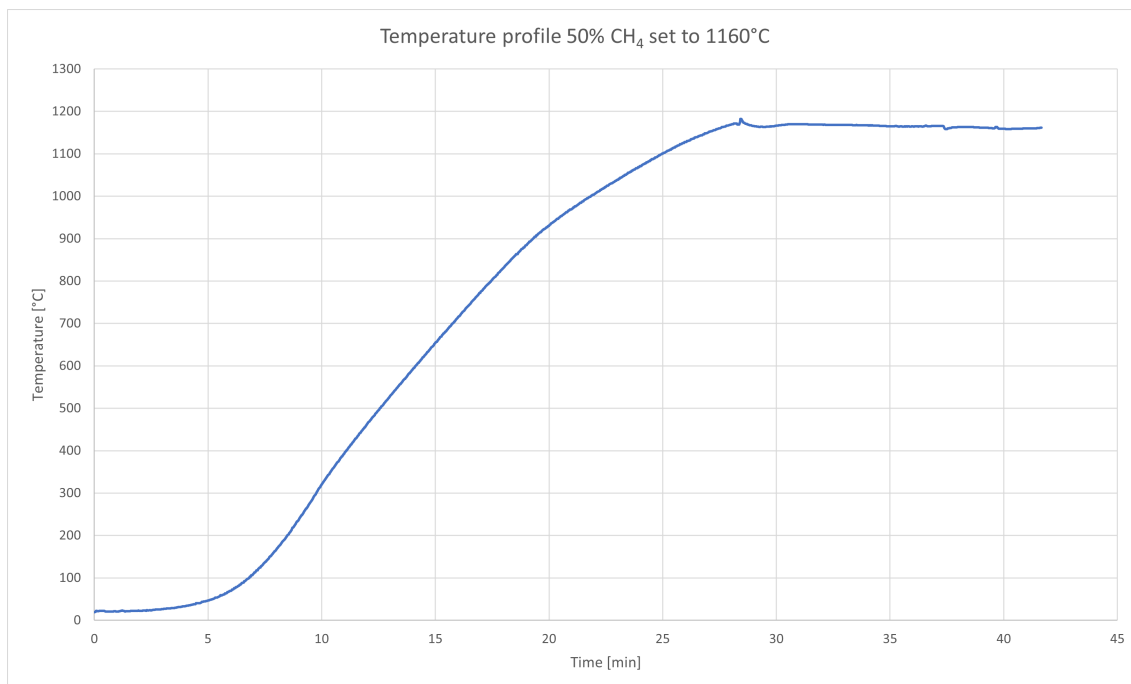

Figure 8: Temperature of reduction experiment with 50% Ar, 50%CH_4 stabilizing at 1161°C and is terminated after 42 minutes.
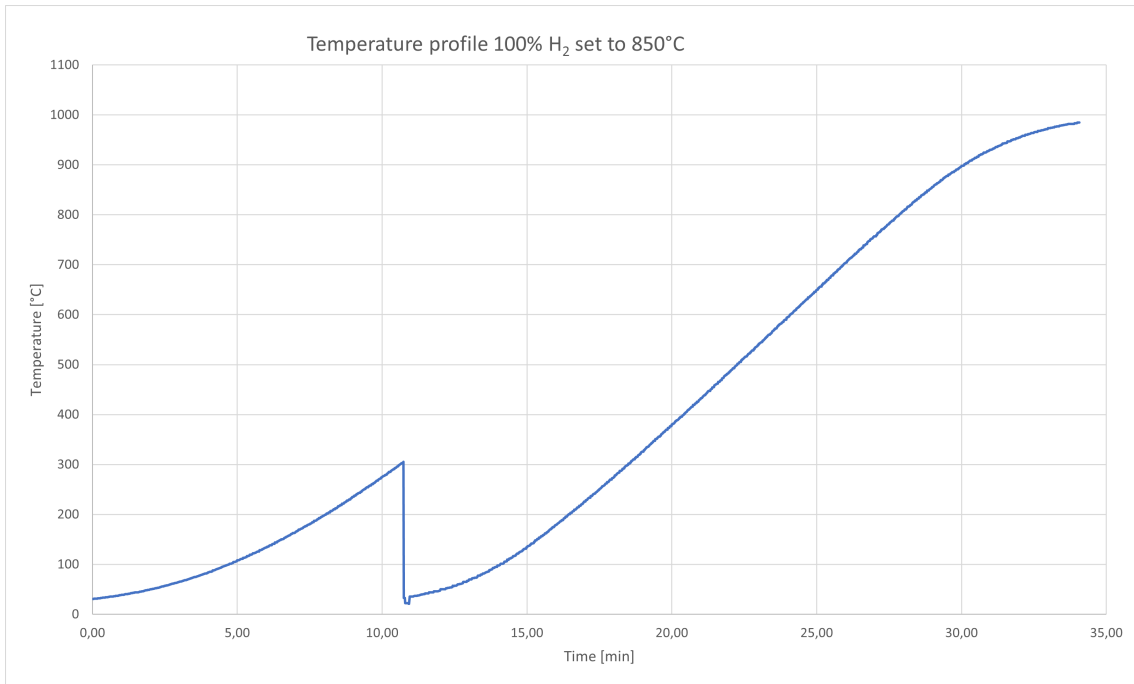
Figure 9: Temperature of reduction experiment with $100\%H_2$ stabilizing at $1015°$C cut short due to loss of data.
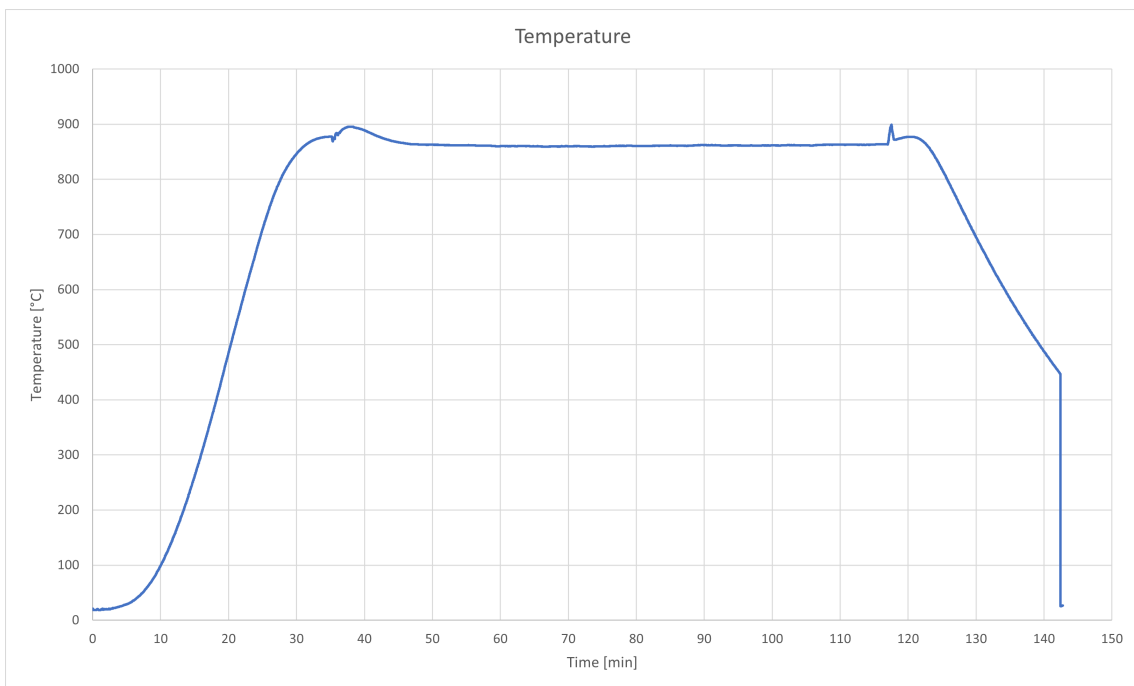

Figure 10: Temperature profile of the methane containing experiments at $860°$C. with a similar profile for each of the experiments.

3.3.1   Calcination and reduction in thermogravimetric analysis

The TG Experiments were performed using a Linseis - STA PT 1600 - TGA 2017. The TG was performed on a sample of the raw ore, and then again in a similar atmosphere as the reduction experiment with hydrogen. The same sample was used for both the calcination and reduction with a BET analysis in between the experiments. For the first TGA the sample was measured to 2.1364 grams and was heated at a rate of 5 °C/min for 180 min up to 900° then kept at that temperature for 60 minutes, then cooled down to room temperature. A separate sample of the raw ore was dried at 80° overnight in order to compare the mass change to the TG plot at lower temperatures. This giving insight into the level of moisture evaporating during the calcination. The second TG analysis, which included the hydrogen atmosphere was measured to 1.7910 grams and had a temperature profile such that it was heated at a rate of 10°/min and kept at that temperature for 60 minutes, then cooled. The temperature profiles for the respective experiments are visually presented along the results from the analysis in Figures 12 and 13. For the hydrogen reduction the gas flow was set to 0.2NL/min with Ar during heating and cooling, and 0.2NL/min H_2 during the reduction. When performing the TG analysis with the hydrogen atmosphere a gas detector was used to detect potential leaks, and the experiment was kept under observation until the gas flow of H_2 was stopped.

3.4   Characterization

3.4.1   SEM procedure

Samples for analysis were prepared using two different methods. The raw and calcinated ore were cast using CitoPress mounting press using polyfast epoxy. This epoxy is slightly conductive and made to be used in SEM. CitoPress have settings for polyfast. The epoxy was heated to 180°C for 3.5 minutes, and then directly cooled down for 1.5 minutes. This process happened under a pressure of 300 bar. After casting, the samples were ground down using the ATM Saphir 330 Struers RotatoPol up to 4000 grit paper. After grinding the samples were coated with a thin layer of carbon in SC7620 Mini Sputter/ Glow Discharge System at 6 seconds intervals 10 times.

The reduced ore was cast using Epofix, in a weight-based relationship of 25 to 3 between resin and hardener respectively. After casting the epoxy was left to cure overnight under a plastic cup. The mixing of epoxy and curing was performed under a fume hood. When cured these samples were also ground down using the ATM Saphir 330, Struers RotatoPol up to 4000 grit paper. Then the samples were coated in a thin layer gold in SC7620 Mini Sputter/ Glow Discharge System for 30 seconds, however due to excess gold on the first attempts, the samples were ground, then coated again. This left small artifacts of gold within the open pores of the samples.

After coating, a copper tape was added connecting the top to the bottom of the samples to ensure conductivity. Before being mounted into the SEM the height of the sample plus the sample holder was adjusted to fit just under a measuring bar to ensure good data collection during EDX analysis. For imaging a JEOL JCM 6000 scanning electron microscope. The samples were imaged using backscatter electron imaging (BEI) at 400x with acceleration voltage of 15kV. BEI was chosen as this primarily gives information on elemental distribution and less information on topography, which is not of interest. Additionally, EDX point, and map analysis was carried out.

3.4.2 XRD procedure

XRD were done in Rikagu MiniFlex 600 with a speed of $1°$ per minute from $10°$-$90°$. The raw ore was crushed down using a Retsch RS200 Vibratory Disc Mill at 800 rpm for 45 seconds, while the calcined and reduced samples were crushed into a fine powder using a pestle and mortar. The samples were prepared by placing approximately a small spatula of powder on a glass plate and sample holder before a small amount of ethanol were added the mix was distributed evenly, as to cover the analysis area. The sample holder was then mounted in the machine.

To analyze the results, the EVA software was used. Rikagu MiniFlex 600 doesn't give files in a format that is compatible with EVA, therefore the powDLL converter from the University of Ioannina were used to convert the files into XY format. The same procedure for XRD analysis was performed on each of the samples.

3.4.3 XRF procedure

XRF analysis were performed on the raw and the calcined ore. The two samples were crushed into fine powder prior to being sent. The raw ore was crushed using the Retsch RS200 Vibratory Disc Mill at 800 rpm for 45 seconds and the calcined sample was crushed using a pestle and mortar.

3.4.4 BET procedure

The BET samples had to fit a test tube with internal diameter of 7 mm in diameter. This meant the samples had to be crushed in order to be measured. In preparation for BET the samples were degassed with N_2 at $250°$C for 20 hours using Degas Smartprep for 3Flex from Micromeritics.

After degassing, when the samples were at a stable room temperature, the samples were attached to the Micrometics, 3 Flex 3500 BET. A cooling bath of liquid nitrogen was used for keeping the samples at a stable, cold temperature. Approximately 3L liquid nitrogen was used for cooling.

When handling liquid nitrogen proper protective equipment was used, such as a face shield and warm gloves.

4 Results

4.1 Observations

When the ore was being crushed there white inclusions was discovered in the sample. These were later analyzed. An image of some of these inclusions is showing in Figure 11.

Figure 11: White inclusions found in the polymetallic manganese nodules.

The gas detector discovered no traces of phosphine during the calcination, however small amounts of SO_2 was detected.

4.2 Mass changes in stationary bed reduction

The average mass change were calculated for calcination and reduction. In Table 4 the mass loss, and the percentage loss for calcination is calculated. The mass prior was found by weighing the crucible before and after loading it with ore, while the mass post was found by weighing the crucible before and after it was emptied. The average weight loss was found to be approximately 27.3%, which correlate well with the data found during the TG analysis. The mass loss and rate of loss for the reduction was calculated in the same way as for the calcination. These values are provided in Table 5.

Table 4: Mass calculations and mass loss for calcination

Calcination	Mass pre [g]	Mass post [g]	Mass loss [g]	Mass loss [%]
Crucible 1	37.519	27.094	10.424	27.8
Crucible 2	84.569	61.344	23.225	27.5
Crucible 3	26.832	19.480	7.352	27.4
Crucible 4	169.449	123.247	46.201	27.3
Crucible 9	170.211	124.049	46.162	27.1
Sum	488.579	355.214	133.365	27.3

Table 5: Mass calculations and rate of loss for reduction

Reduction	Mass pre [g]	Mass post [g]	Mass loss [g]	Rate of loss [%]
100% H_2	49.72	45.58	4.14	8.33
50%CH_4 40%H_2	50.19	48.02	2.17	4.32
50%CH_4 10%H_2	49.18	47.26	1.92	3.90
50%CH_4	50.41	46.47	3.94	7.82

A separate sample was dried overnight at 80°C to measure the weight loss caused purely by drying. This gives context to the calcination and illustrates the amount of moisture or other volatile substance makes up the raw sample. The data from Tables 4, 5, and 6 can also be compared to the data from the TG.

Table 6: Mass calculations and rate of loss for drying

Drying	Mass pre [g]	Mass post [g]	Mass loss [g]	Rate of loss [%]
Crucible 1	23.331	20.547	2.784	11.9

4.3   Mass changes in TGA for calcination and reduction

The TG diagram of the calcination in Figure 12 shows that the mass change begun around a temperature of 100°C, slowing down before making another step around 400°C, and again at 550°C. No more mass change of note was measured beyond 800°C.The total mass loss measured at the end of the TG experiment was approximately 578 mg. The relative mass loss is a more useful value for comparison and is calculated to be approximately 27.1%.
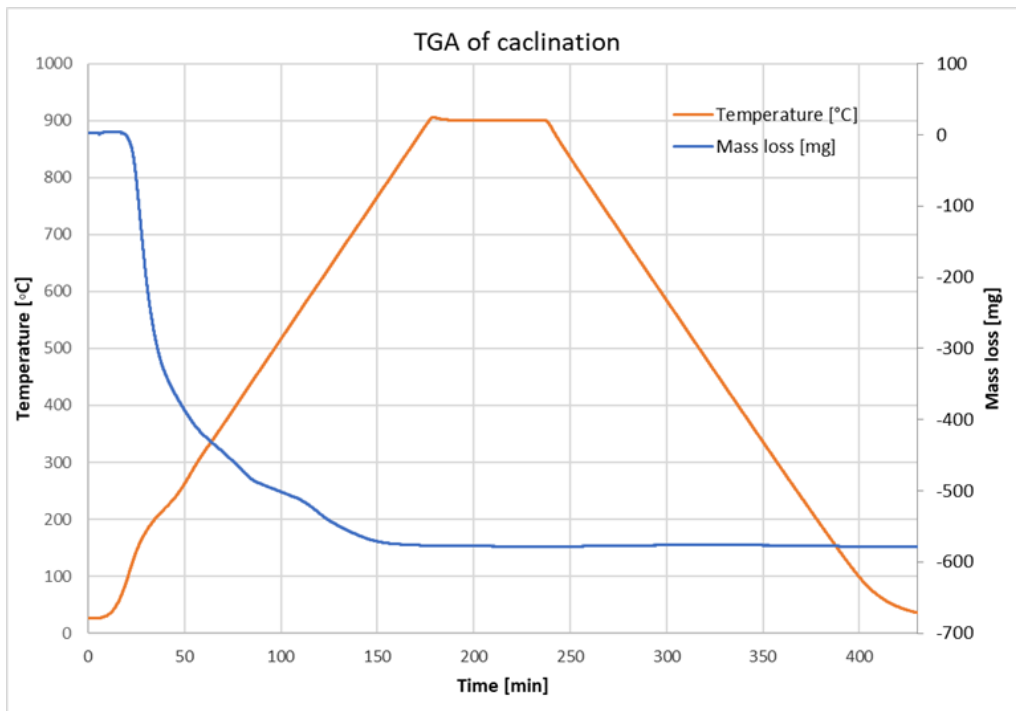

Figure 12: Thermogravimetric analysis from the calcination process of the raw polymetallic nodules.

The TG analysis with hydrogen atmosphere as shown in Figure 13 shows a simple curve which begun mass loss as soon as hydrogen was applied, and quickly slowed. At the point where the sample began cooling and the hydrogen supply was shut of the curve was disturbed after which the mass loss appeared to accelerate. The final mass loss was measured to be 136 mg or 7.6%.
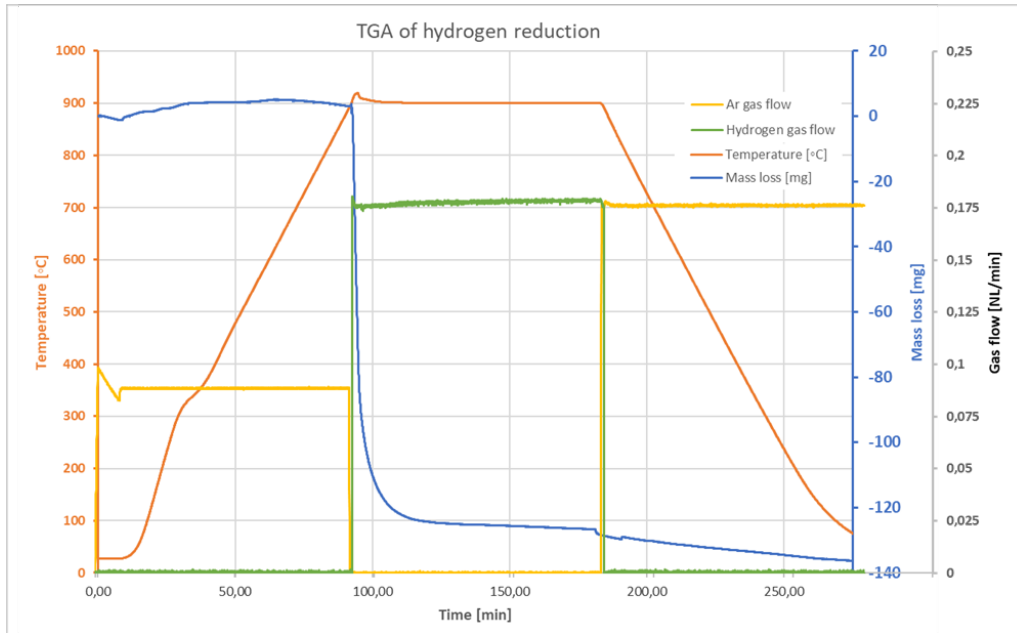

Figure 13: Thermogravimetric analysis of the reduction process with a $100\% H_2$ atmosphere of the calcined ore from the previous TGA.

4.4 BET results

Only the calcined sample gave usable data. The specific surface area of the calcined sample was found to be 2.2476 m^2/g. A full report from the Micrometics, 3 Flex 3500 can be found in Attachment B.

4.5 XRF results

Chemical composition analysis of the raw and calcined polymetallic nodules by XRF measurements were provided by Degerfors Laboratorium AB. The results are given in Table 7 and 8. The full report from Dregerfors Laboratorium AB is provided in Appendix C. A normalization has also been performed to replace the phase MnO with MnO_2 for the raw ore and Mn_2O_3 for the calcined ore. The LOI was also corrected for the raw ore during normalization. The LOI was determined to be 15.4%, the loss from drying at 80°C overnight subtracted from the average loss from calcination. The procedure for normalization is provided in Appendix D.

Table 7: XRF analysis of raw PMN and normalization of MnO to MnO_2.

Element	[wt%]	Noralized [wt%]
CaO	3.45	2.95
MgO	3.83	3.28
SiO$_2$	34.6	29.60
Al$_2$O$_3$	12.1	10.35
Fe$_2$O$_3$	7.00	5.99
MnO/MnO$_2$	23.3	24.43
Cr$_2$O$_3$	0.02	0.02
V$_2$O$_5$	0.05	0.04
TiO$_2$	0.87	0.74
NiO	1.14	0.98
Na$_2$O	2.57	2.20
K$_2$O	2.56	2.19
P$_2$O$_5$	0.41	0.35
SO$_3$	0.11	0.09
ZnO	0.11	0.09
MoO$_3$	<0.01	0.01
CuO	0.84	0.72
PbO	-//-	-//-
ZrO$_2$	0.01	0.01
SrO	0.05	0.04
BaO	0.20	0.17
Cl	0.22	0.19
Co$_3$O$_4$	0.17	0.15
CeO$_2$	<0.01	0.01
Y$_2$O$_3$	-//-	-//-
LOI	6.26	15.4

Table 8: XRF analysis of calcined PMN and normalization of MnO to Mn_3O_3.

Element	[wt%]	Normalized [wt%]
CaO	3.05	2.89
MgO	4.96	4.71
SiO$_2$	16.2	15.37
Al$_2$O$_3$	6.73	6.39
Fe$_2$O$_3$	8.84	8.39
MnO/Mn$_2$O$_3$	48.0	50.69
Cr$_2$O$_3$	-//-	-//-
V$_2$O$_5$	0.10	0.09
TiO$_2$	0.68	0.65
NiO	2.40	2.28
Na$_2$O	3.29	3.12
K$_2$O	1.26	1.20
P$_2$O$_5$	0.39	0.37
SO$_3$	0.22	0.21
ZnO	0.29	0.28
MoO$_3$	0.10	0.9
CuO	1.72	1.63
PbO	0.06	0.06
ZrO$_2$	0.03	0.03
SrO	0.08	0.08
BaO	0.28	0.27
Cl	0.03	0.03
Co$_3$O$_4$	0.36	0.34
CeO$_2$	-//-	-//-
Y$_2$O$_3$	0.03	0.03
LOI	0.81	0

4.6 SEM and EDX results

4.6.1 Raw ore

The SEM imaging of the raw polymetallic manganese nodules show a thin layered structure. Fractures can be seen through the sample. It was imaged with backscattered electrons at 400x with 15 kV.
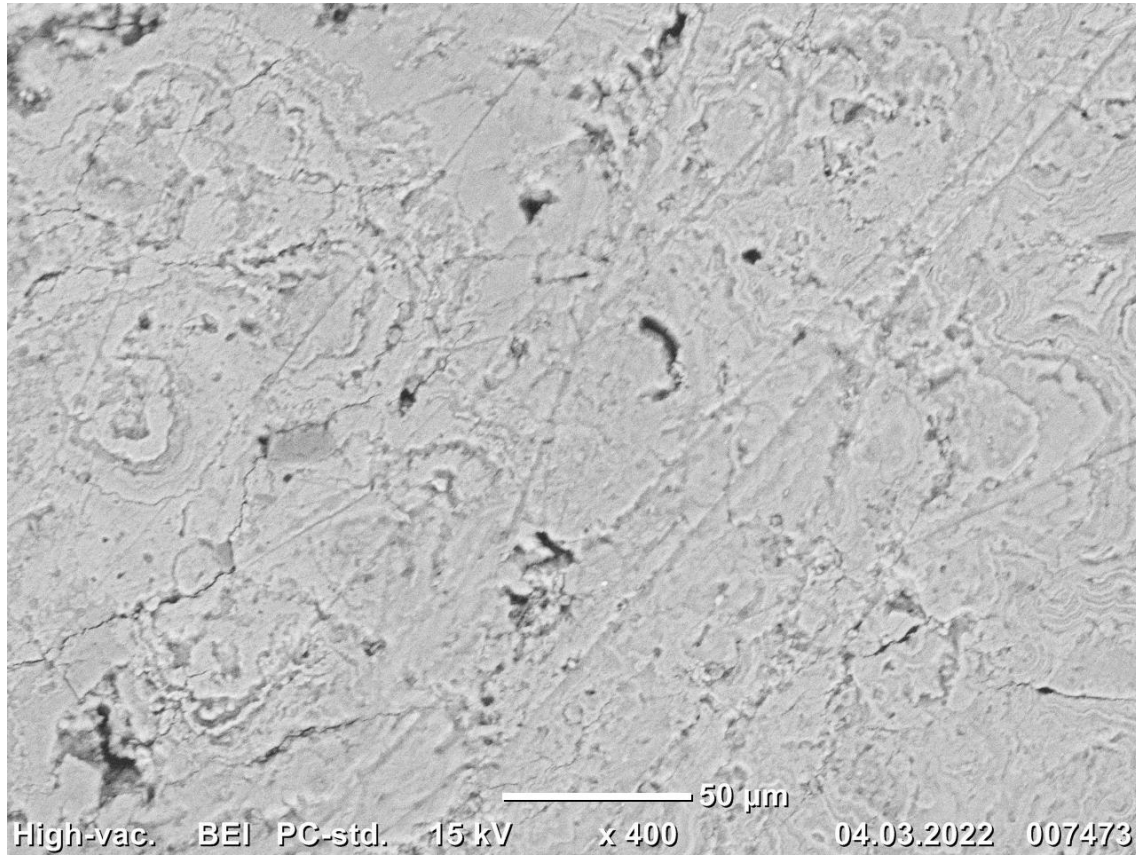
Figure 14: 400x SEM image of the raw PMN with backscatter electrons. The layered structure is indicative of the known growth mechanism.

The EDX analysis of the raw nodule in Figure 15 a clear layering, where Ni, Cu, Mn and Mg can be located in the same layers, Co, Fe, Si, Ti and Ca seem to correlate as well, and K, Na, Al and more Si seems to be scattered throughout the sample.

Figure 15: EDX of the raw ore at 400x magnification. Elements included from left to right and top to bottom are: Ni, Co, Cu, Na, Mn, Fe, Si, Al, Mg, K, Ti, and Ca

4.6.2 Calcined ore

The SEM image of the calcined ore, shows a large pore volume. There is less of a layered structure and there is good contrast between areas of the sample. It was imaged with backscattered electrons at 400x with 15 kV.
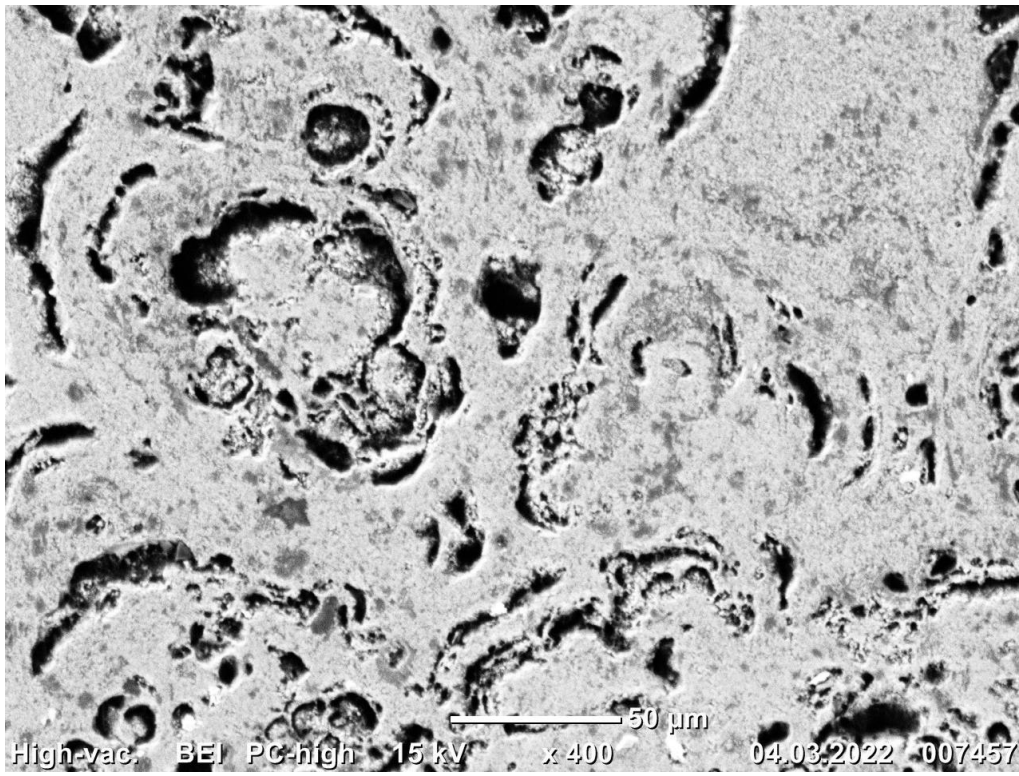
Figure 16: 400x SEM BEI image of the calcined ore. The layered structure from the raw ore is less prevalent.

The EDX analysis of the calcined nodule in Figure 17 shows less of a layered structure. Ni, Co, Cu, Mn, Fe, K and Ti are now more evenly distributed in the sample. Elements of Na, Si, Al, Mg and Ca seem concentrated along the pore walls. As well as spots of Cu, Na, Si, Al, Mg, K, and Ca are spread through the sample surface, not necessarily correlating with each other.
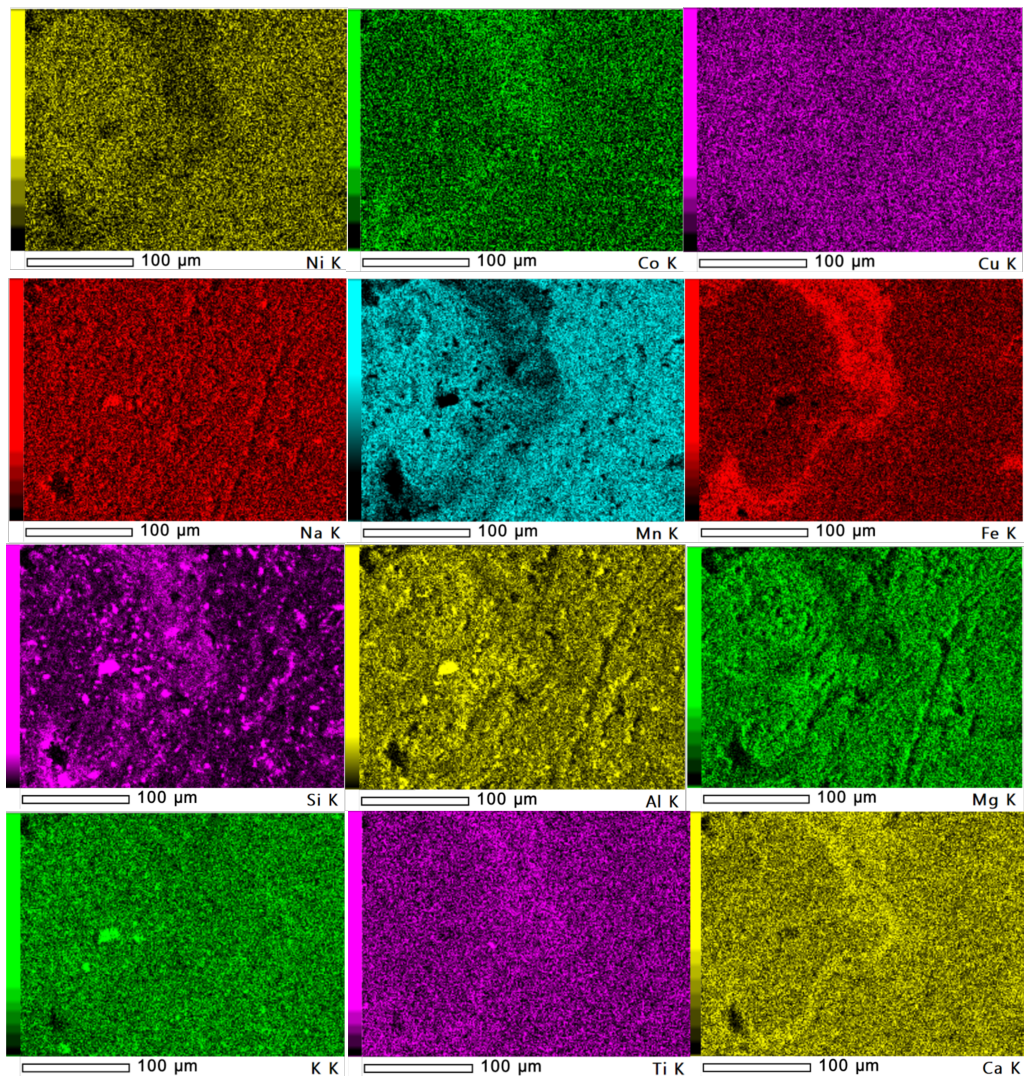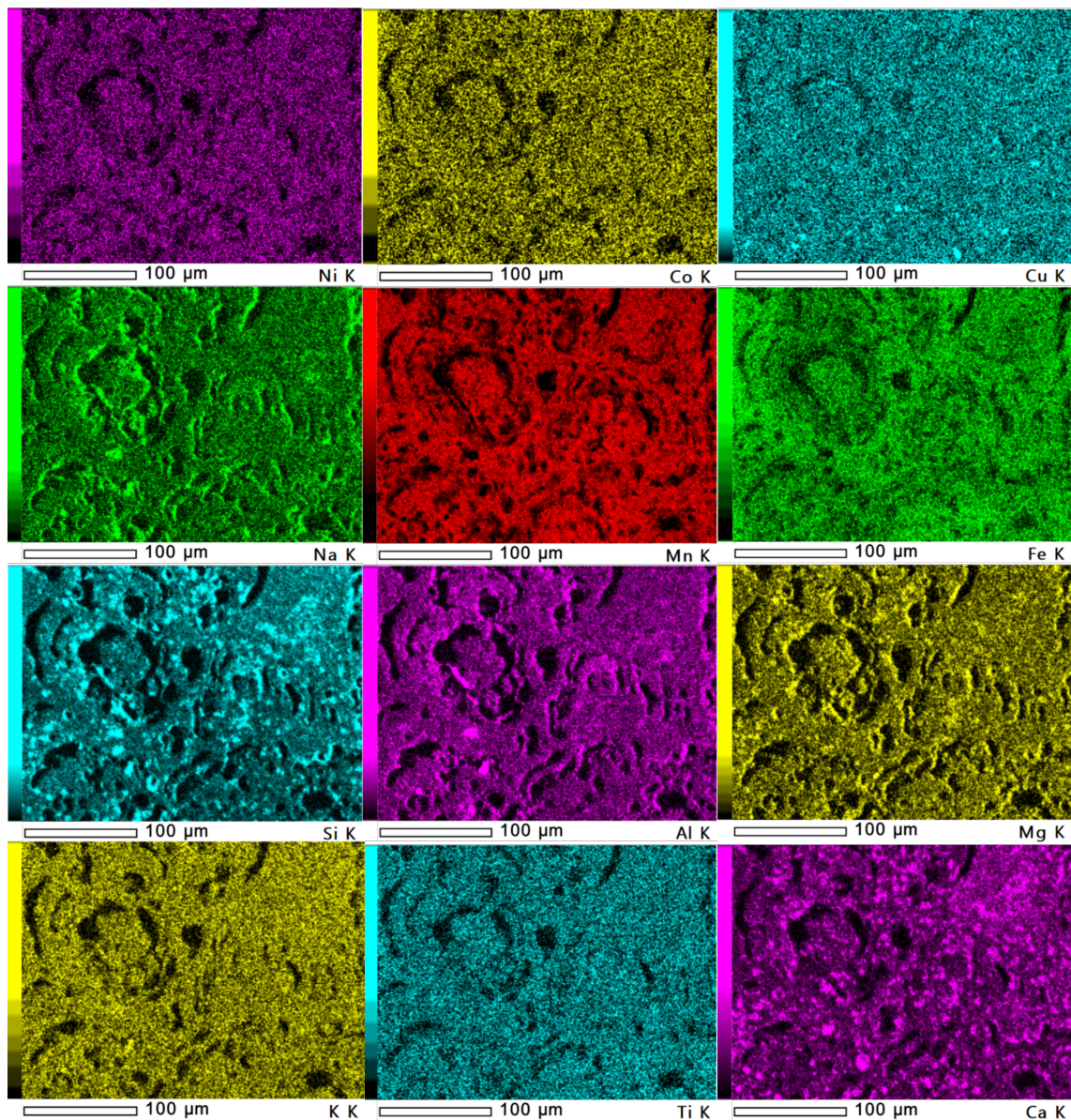

Figure 17: EDX of the calcined ore at 400x magnification. Elements included from left to right and top to bottom are: Ni, Co, Cu, Na, Mn, Fe, Si, Al, Mg, K, Ti, and Ca.

4.6.3 Reduced ore 50%Ar, 50%CH_4

The SEM image of the sample reduced in an atmosphere of 50% Ar, 50%CH_4 is encapsulated with the epoxy filling the open pores. There is high contrast between the areas of high and low intensity. It was imaged with backscattered electrons at 400x with 15 kV.
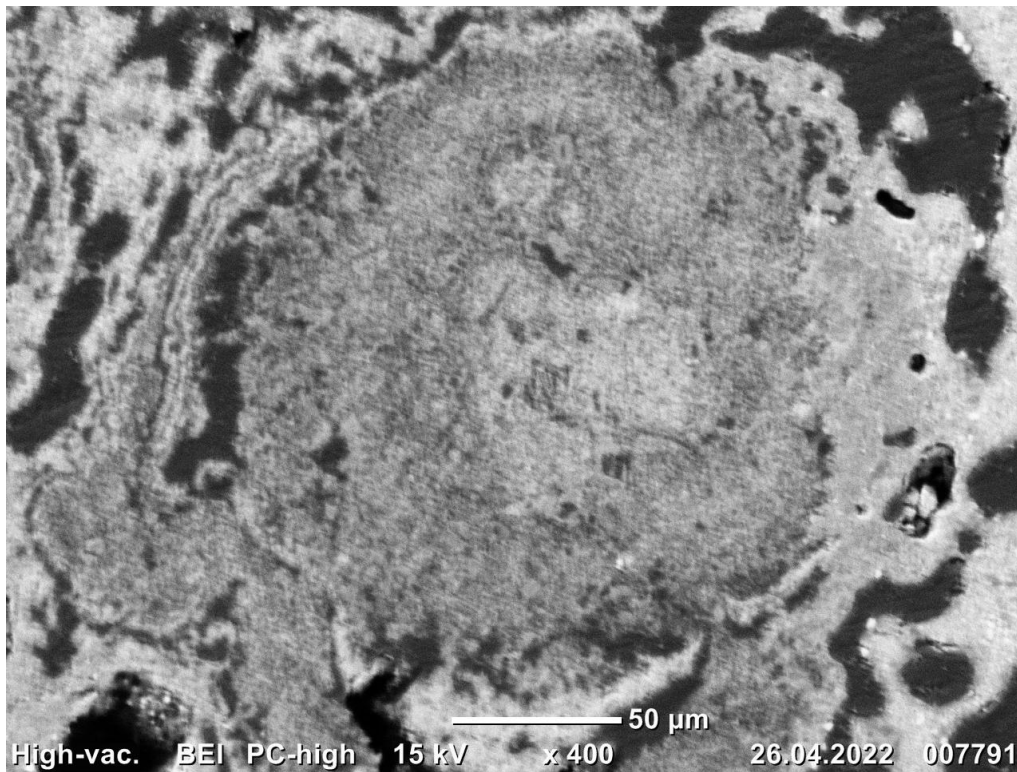
Figure 18: 400x SEM BEI image of the sample reduced by 50%Ar 50%CH_4.

The EDX analysis of the sample reduced in an atmosphere of 50% Ar, 50%CH_4 in Figure 19 shows carbon largely separated from the other elements, this is the epoxy. Oxygen is concentrated in mainly two areas, one spot in the lower left, and in a band on the right. This is mainly correlated with the elements of Na, Al, Si, K, Ca, and Ti. Phases of iron, and manganese can be found both separately and together. The elements Co, Ni, Cu and Au is evenly spread over the sample with Ni and Cu having some spots. Na, Al, and Si share some spots, Si and Ca also share some spots.
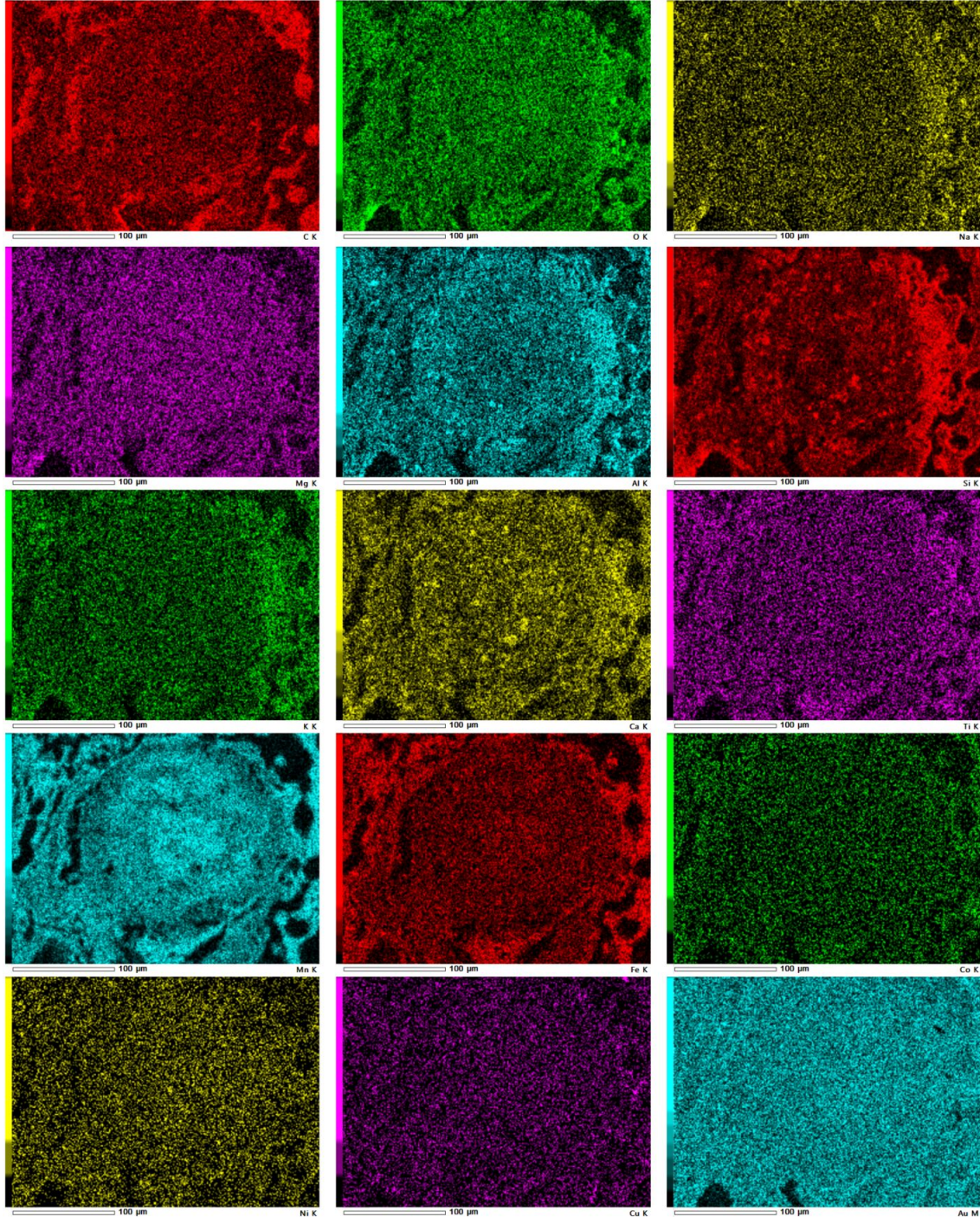
Figure 19: EDX mapping of 50%Ar, 50%CH_4 . Elements from left to right, top to bottom: C, O, Na, Mg, Al, Si, K, Ca, Ti, Mn, Fe, Co, Ni, Cu, and Au.

4.6.4 Reduced ore 40%Ar, 50%CH_4, 10%H_2

The SEM image of the sample reduced in an atmosphere of 40%Ar, 50%CH_4, 10%H_2 in Figure 20 shows clear lines of increased intensity. It was imaged with backscattered electrons at 400x with 15 kV.

Figure 20: 400x SEM BEI image of the sample reduced by 40%Ar, 50%CH_4, 10%H_2.

The EDX analysis of the sample reduced in an atmosphere of $40\%Ar$, $50\%CH_4$, and $10\%H_2$ is shown in Figure 21. Carbon in the epoxy is limited the a few spots, but is otherwise spread in spots on the sample surface. Oxygen alongside most of the elements is mostly evenly distributed throughout the sample, with exception for the areas of epoxy. Phases of iron, and manganese can be found both separately and together. Cobalt, although not having large contrasts, seem to correlate with Fe. Na, K, and Al, and Si, Al, and Ca also share some spots.

Figure 21: EDX analysis of the ore reduced in $40\%Ar$, $50\%CH_4$ and $10\%H_2$ atmosphere. at 400x magnification. Elements included from left to right and top to bottom: C, O, Na, Mg Al, Si, K, Ca, Ti, Mn, Fe, Co, Ni, $Cu4$, and Au.

4.6.5 Reduced ore 10%Ar, 50%CH_4, 40%H_2

The SEM image of the sample reduced in an atmosphere of 10%Ar, 50%CH_4, and 40%H_2 in Figure 22 shows spots of phase separation where spots of high intensity is surrounded by areas of low intensity, all in a matrix of middle intensity. It was imaged with backscattered electrons at 400x with 15 kV.
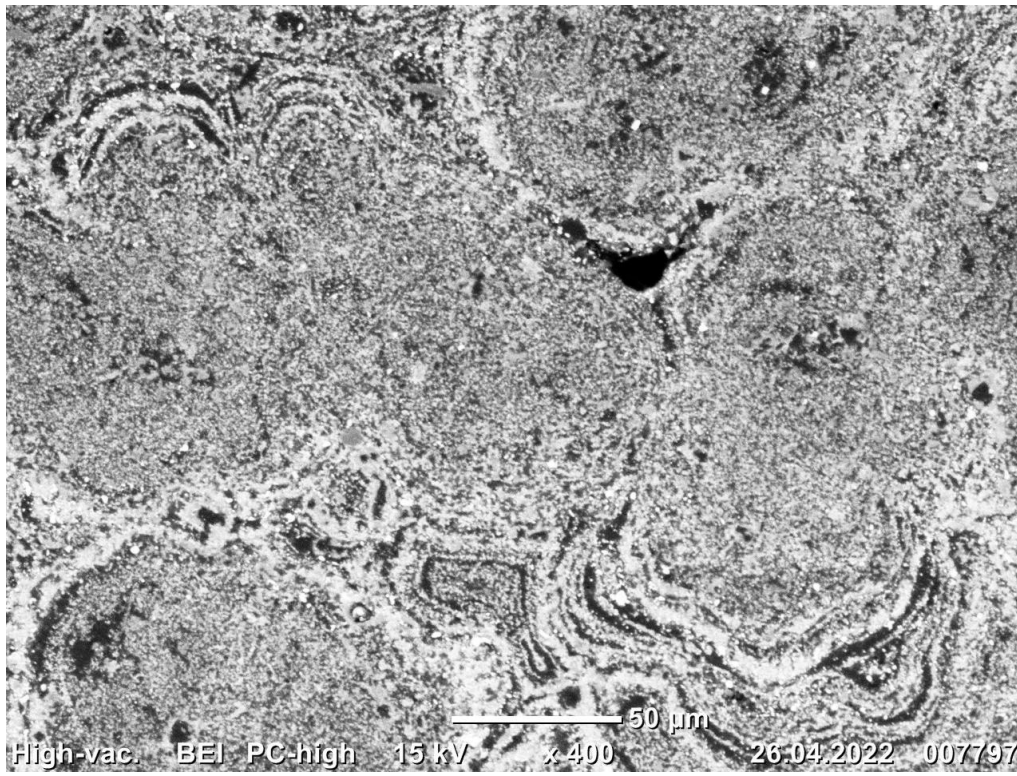

Figure 22: 400x SEM BEI image of the sample reduced by 10%Ar, 50%CH_4, and 40%H_2.

The EDX analysis of the sample reduced in an atmosphere of $10\%Ar$, $50\%CH_4$, and $40\%H_2$ is shown in 23. Carbon mainly in the form of epoxy is located in the previously open pores. A pore which as closed prior to sample preparation seem to have opened, and is visible as a hole in the lower right. Oxygen have high contrasts around certain areas positively correlating with Na, Al, Si, K, Ca and Ti. Phases of iron, and manganese seem to share some larger spots, while not correlating in other areas. Cobalt, although not having large contrasts, seem to correlate with Fe. Na, K, Al, and Si share multiple spots and Si, Al and Ca also share some spots.
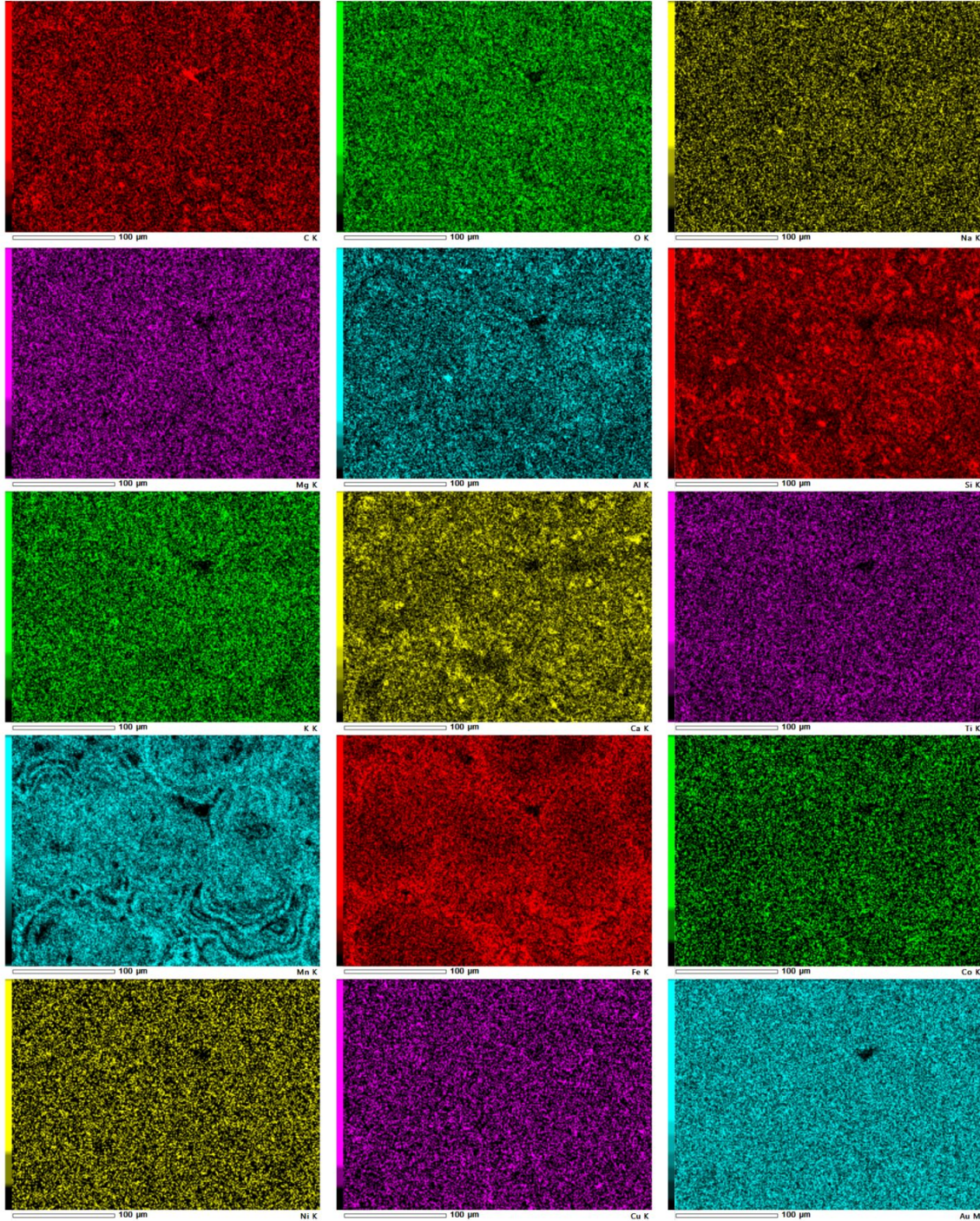

Figure 23: EDX analysis of the ore reduced in $10\%Ar$, $50\%CH_4$ and $40\%H_2$ atmosphere. at 400x magnification. Elements included from left to right and top to bottom is C, O, Na, Mg Al, Si, K, Ca, Ti, Mn, Fe, Co, Ni, Cu, and Au.

4.6.6   Reduced ore $100\%H_2$

The SEM image of the sample reduced in a pure hydrogen atmosphere as shown in Figure 24 shows a highly detailed layered structure following the pores of the sample. It was imaged with backscattered electrons at 400x with 15 kV.
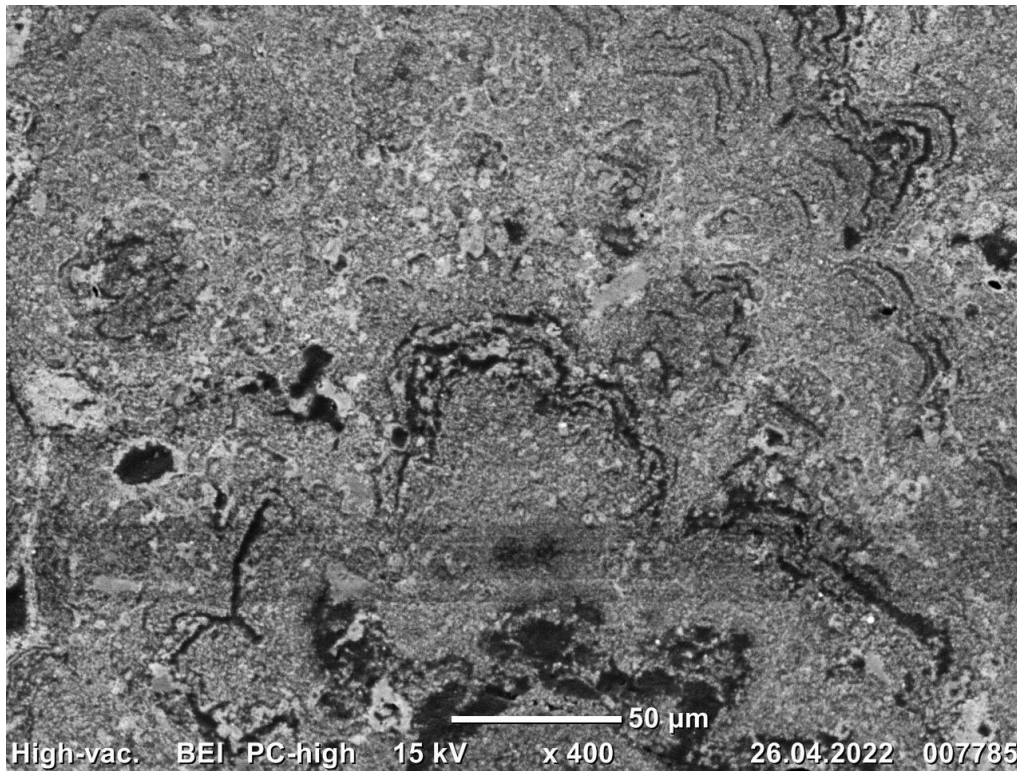
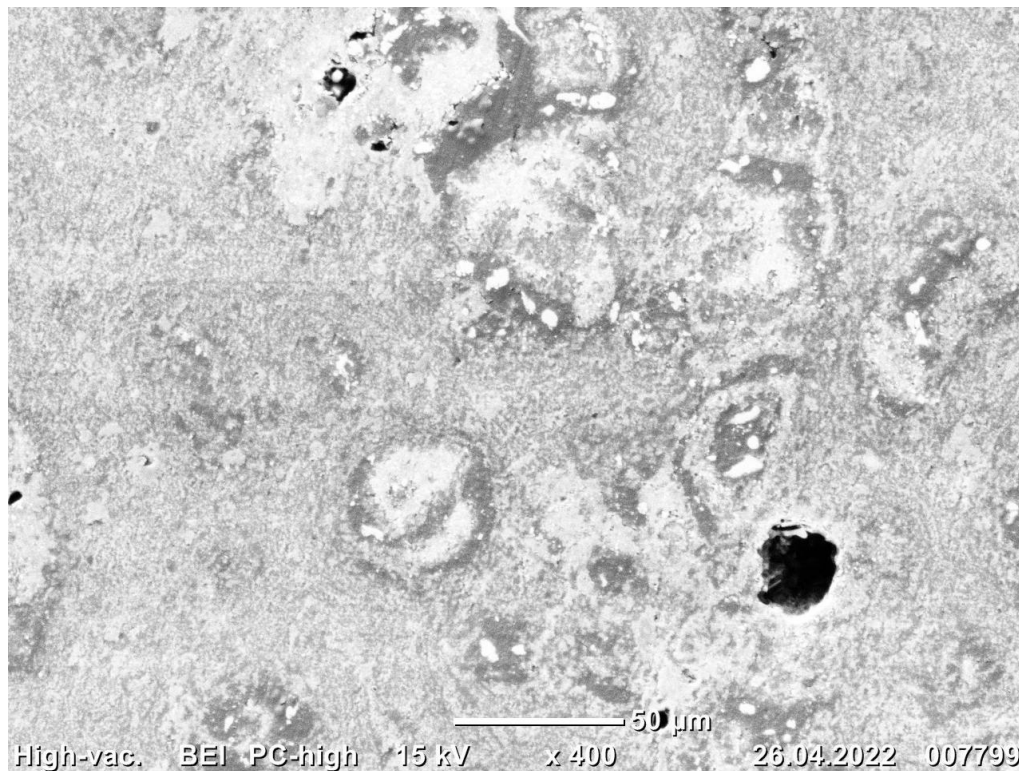
Figure 24: 400x SEM BEI image of the sample reduced by $100\%H_2$.

The EDX analysis of the sample reduced in an atmosphere of 100% H_2 is shown in 25. Carbon mainly in the form of epoxy is separated from the other elements. Oxygen, Mg, K, Ti, Co, Ni, and Cu is largely evenly spread over the analyzed surface, except from the areas of high carbon concentration. Manganese has a high contrast, negatively correlating with carbon. seem to share some larger spots, while not correlating in other areas. Fe has a spot of increased concentration on the center left, but this does not correlate with any other elements. Na, K, Al, and Si share multiple spots and Si, Al and Ca also correlates.
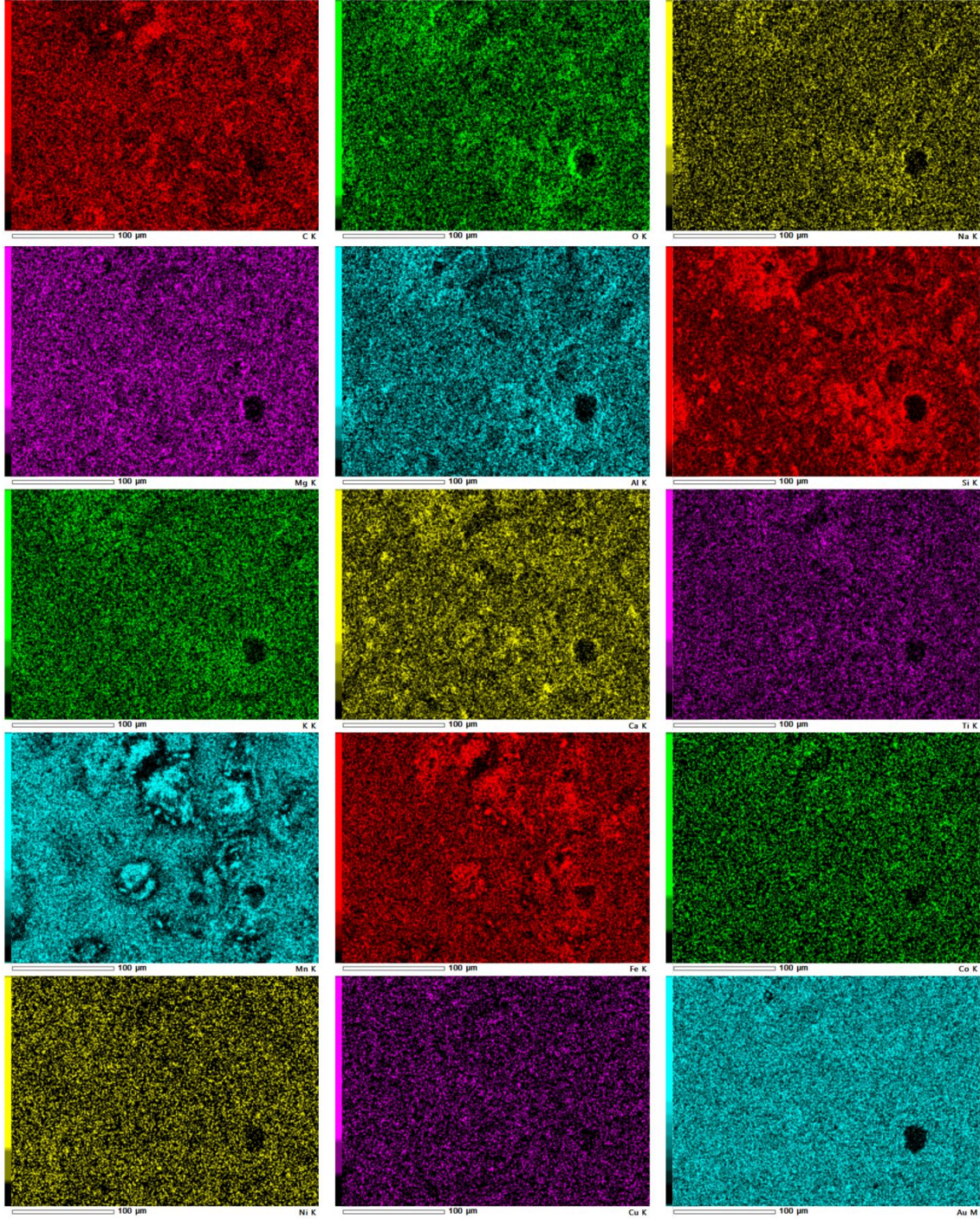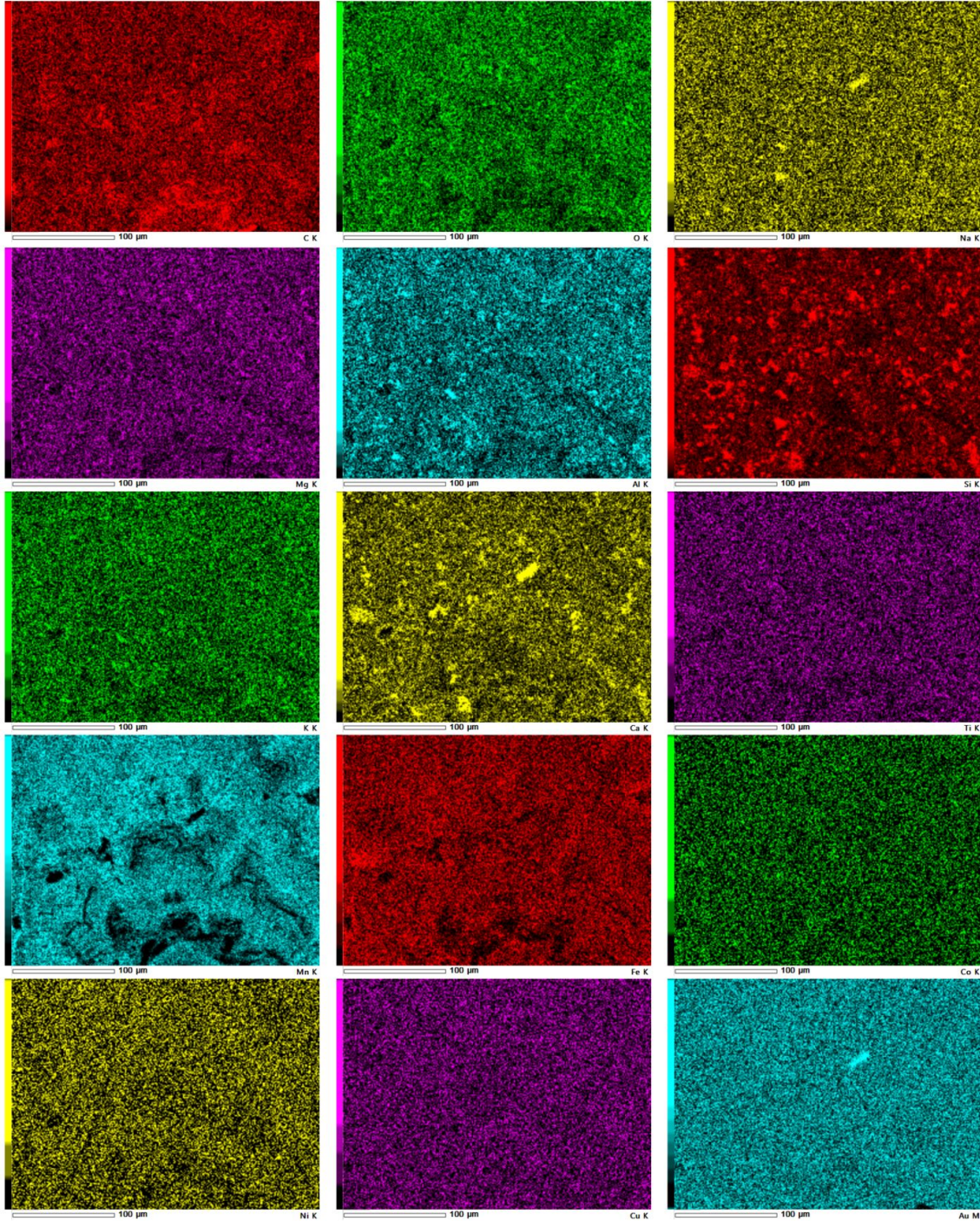

Figure 25: EDX analysis of the ore reduced in an $100\% H_2$ atmosphere at 400x magnification. Elements included from left to right and top to bottom is C, O, Na, Mg Al, Si, K, Ca, Ti, Mn, Fe, Co, Ni, Cu, and Au.

4.7 XRD

4.7.1 XRD analysis of raw ore

The XRD analysis of the raw ore as shown in Figure 26 indicated a phase composition of quartz (SiO_2), albite $(NaAlSi_3O_8)$, goethite $(\alpha-FeO(OH)$, Ca-Mg-Si $(CaMgSi_2O_6)$, asbolane $(NiMn_2O_3(OH)_4 \cdot H20)$, lithiphorite $(Al_{0.65}H_2Li_{0.33}MnO_4)$, manganese oxide($MnO_2$, vernadite $(Mn(OH)_4)$, chalcophanite $(H_6Mn_3O_10Zn)$, and birnessite(MnO_2). With a lot of noise in the diffraction pattern.
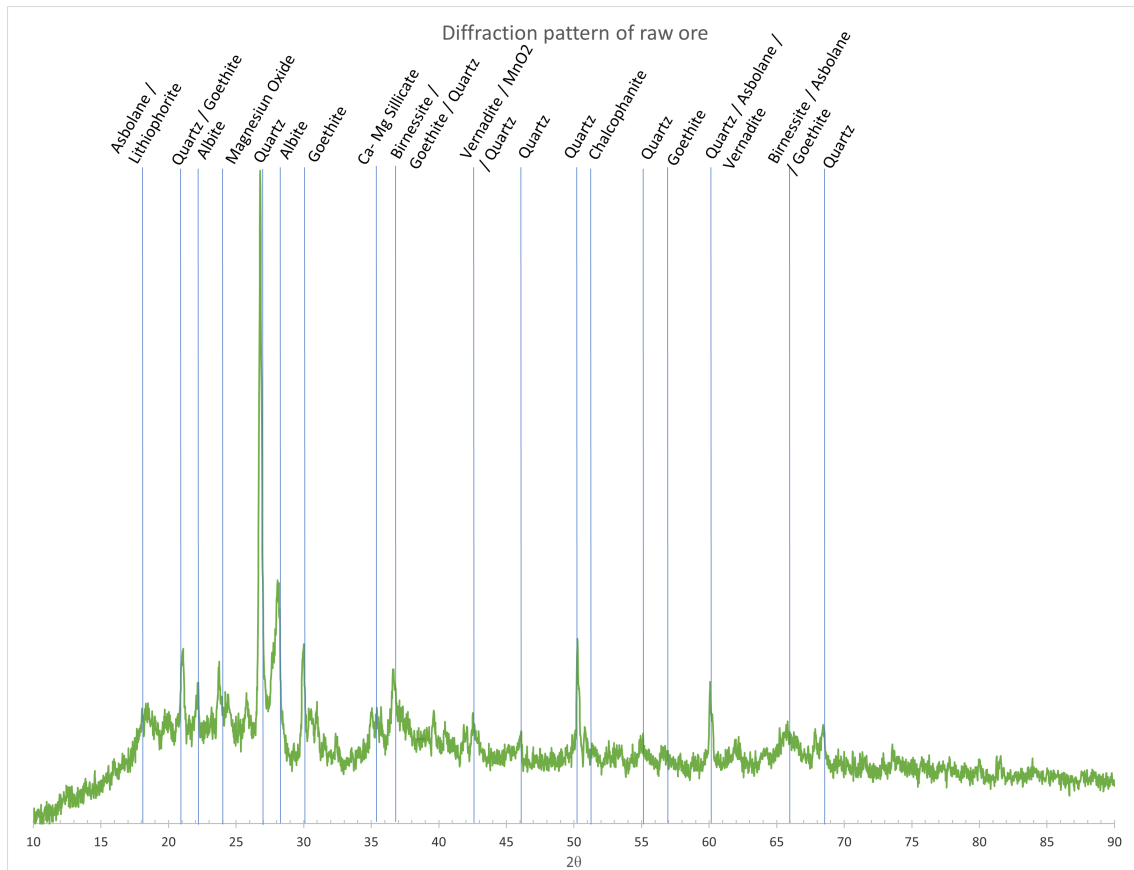
Figure 26: X-ray diffraction pattern of a raw polymetallic nodule, with identified peaks.

The stones identified as inclusions was analyzed with XRD in order to asses the contained phases, the main phases identified were quartz SiO_2 and albite $NaAlSi_3O_8$. Some of the main peaks such as for 45°, 55°, and 65° were however not identified.
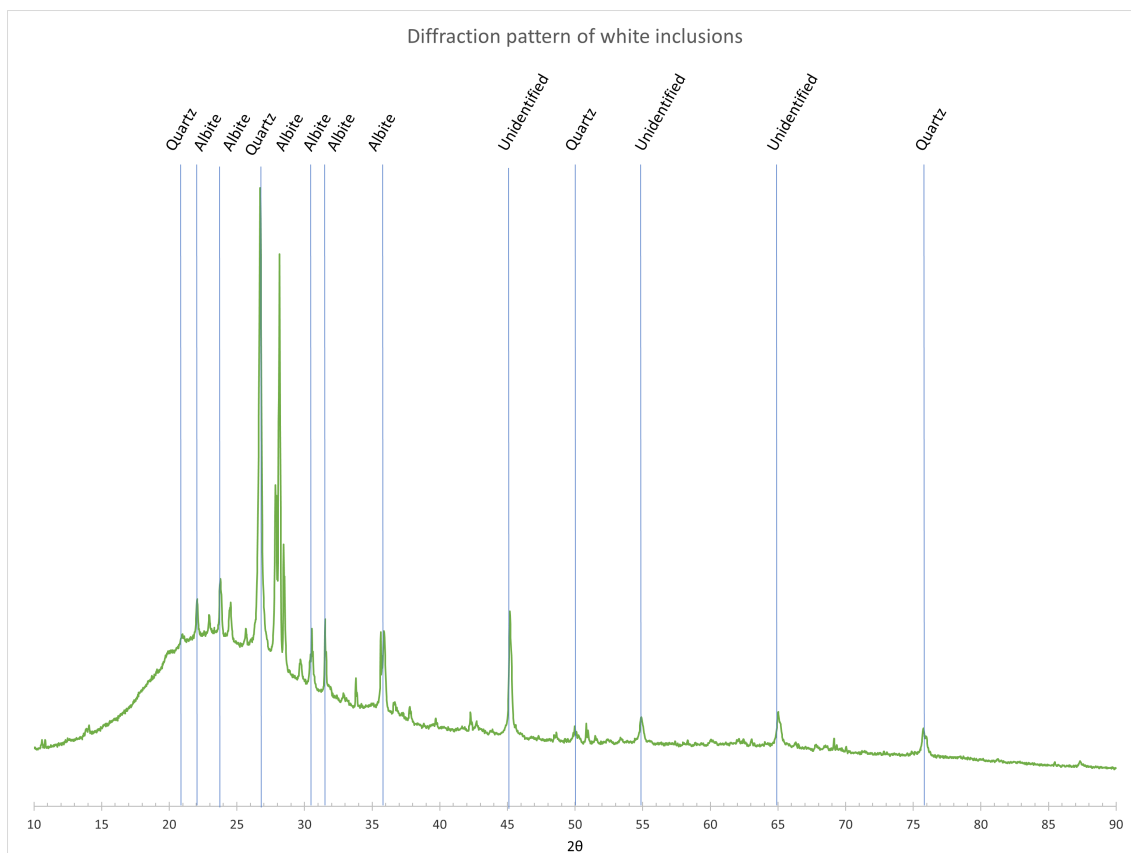
Figure 27: X-ray diffraction pattern of stones found as inclusions in the raw polymetallic nodule, with identified peaks.

4.7.2 XRD analysis of calcined ore

When analyzing the XRD results for the calcined ore, Figure 28, some problems occurred. The XRD pattern shows a wide "bar" between the two peaks at a 2θ-value of roughly 33° and 35°, as well as several of the larger peaks not being identifiable. The peaks identified was manganese bearing magnetite $((Mn, Fe)_3O_4))$, bixbyite (Mn_2O_3), manganese oxide (ζMn_2O_3), magnesium aluminium silicate $(MgO \cdot Al_2O_3 \cdot SiO_2)$, and cuprite (Cu_2O). Of note is the wide bars present between multiple peaks, for example the peak at 32.5° and 35°. Multiple peaks were al.so not identified, such as the paks at 36°, 58° and 60,6°.
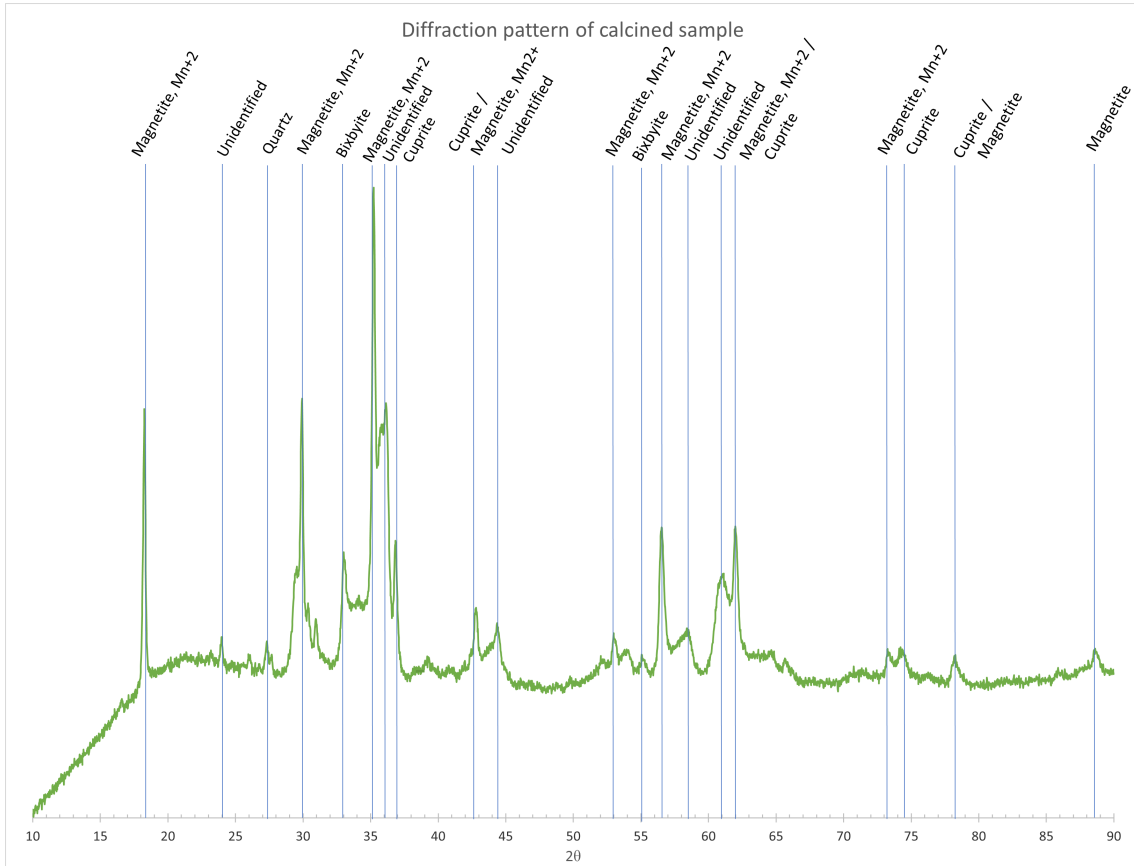
Figure 28: The X-ray diffraction pattern of a calcined polymetallic nodule, with identified peaks.

4.7.3 XRD analysis of reduced ore

The XRD analysis of all the reduced samples is presented in Figure 29. The diffraction patterns of the different samples are similar sharing many of the same identifyable phases. The identified phases were tephorite / fayalite ($(Fe, Mn)_2SiO_4$), nepheline ($NaAlSiO_4$), manganosite (MnO), ferrite ($\alpha - Fe$), and coppernickel ($CuNi$). Austenite ($\gamma - Fe$), and quartz was only identified in the sample reduced in an atmosphere of 40% Ar, 50%CH_4, and 10%H_2.
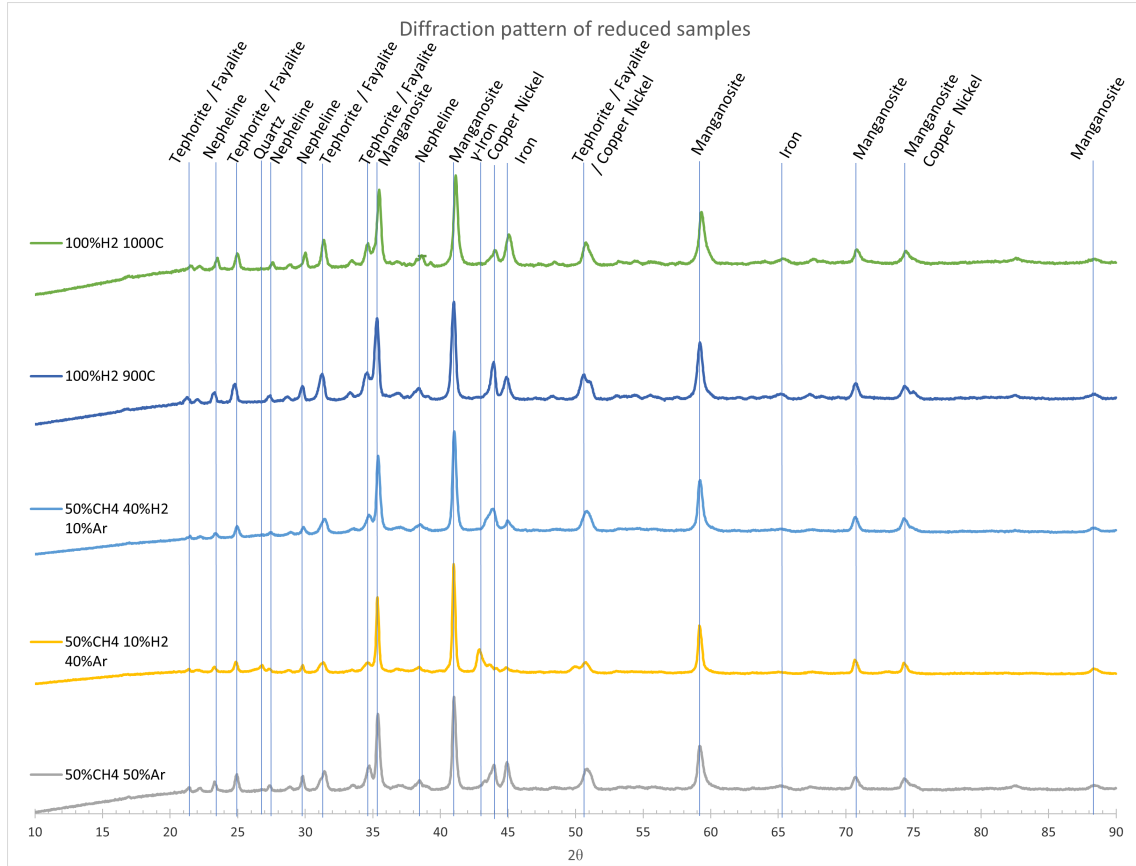
Figure 29: The stacked X-ray diffraction patterns of polymetallic nodules reduced at different atmospheres, with their identified peaks.

5 Discussion

In the following parts both the execution of the sample preparation and results from the various experiments will be discussed. Potential improvements to execution will be presented alongside results of interest.

5.1 Discussion of experimental procedure

5.1.1 Discussion of sample preparation

The calcination was performed in batches, as mentioned in section 3.2 there was a genuine worry of phosphine development. Because of this the calcination was performed in a fume hood and the off gas was tested for toxic gasses. Luckily no phosphine was detected, which would have implied further and more comprehensive risk reduction measures. A limited amount of SO_2 was however detected as the calcination passed $400°C$ and the rest of the calcination was therefore also performed in the fume hood. Future calcination could have been performed in larger volumes and/or be performed within the ReSiNa-furnace in the same program as the reduction. Comparing the TGA of the calcination process with the mass calculations observed from the main batch of the calcination, they seem consistent.

When running the first reduction experiment in an atmosphere of $50\%Ar$, 50% CH_4, there was a high amount of methane cracking causing soot. This soot caused clogging of the venting filters making it necessary to end the experiment early. Future experiments should take methane cracking more carefully into consideration to avoid the furnace malfunctioning. The decision was made to reduce temperature to limit cracking. A misalignment in the ReSiNa-furnace between the programmed and actual crucible temperature caused difficulties in achieving the intended temperature. Because of this the reduction with 100% H_2 was performed at $1016°C$, whilst the methane containing reduction were performed at a lower temperature of $860°C$. The elevated temperature could have caused the sample from the hydrogen reduction to be different. However, as the sample from the TGA-reduction was a suitable replacement this sample was used for further characterization. Both the $900°C$ and $1016°C$ were characterized in XRD, and show little difference. In the future the furnace should be more precisely calibrated, or a more detailed map between programmed settings and resulting temperature should be developed for the furnace.

When logging the temperature data for the reduction process an external thermocouple and data-logger was used. The thermocouple gave good data, however, it proved difficult for processing data and some of it was lost or corrupted by data overflow this is especially visible in Figure 9. A part of this data loss or corruption could be caused by the overwriting of saved temperature profiles. The wires connecting the data-logger and thermocouple were not isolated, and at times these connected giving false temperature values. In future experiments potential remedies for collecting temperature profiles should be the use of isolated wires and either using a different data-logger or being more diligent in collecting the data.

Another factor regarding the temperature whilst reducing is the factor of the temperature not stabilizing prior to the reduction agents were introduced into the furnace. As can be seen in Figure 10 - 13 the temperature peaks before stabilizing at the working temperature. This can be seen in all the temperature profiles. However, as the working gas is applied just as the temperature reaches working temperature, it is difficult to determine whether this peak is caused by the reduction being exothermic or if it's caused by a delay in the system. The temperature profile of Figure 12 and 13 is probably more accurate due to the reaction volume being smaller. These figures show that the peak is more apparent when hydrogen is introduced, and may indicate an exothermic reaction. The profiles from the TGA are presumed to be more accurate, as the reaction chamber is smaller, and the temperature control more accurate in the thermogravimetric device than in the ReSiNa-furnace.

The size of the calcined ore did not seem to have an observable effect on the mass loss. This is because the ore used in the reduction experiment with $100\%H_2$ and the experiment with 10% Ar, $50\%CH_4$, $40\%H_2$ was of a smaller size than the samples used in the experiments with $40\%Ar$, $50\%CH_4$, $10\%H_2$ and $50\%Ar$, $50\%CH_4$ without any sign of correlation. A possible explanation for the lower mass loss in the samples reduced under a methane atmosphere may be the formation of soot from methane cracking. This, however, doesn't explain why the sample reduced under $50\%Ar$, $50\%CH_4$ have the second highest mass loss, as this was expected to have the highest amount of methane cracking. This could also be caused by errors in the weight measurement, and should in future research be measured more carefully.

The different reduction compositions did not only cause a difference in chemical composition, but also a difference in total reduction capacity. Calculating the theoretical total available electrons in a complete reduction, this difference is visible in Table 9. It is not apparent that this would have an effect on the resulting reduced sample, as all of the experiment would have plenty of reduction potential in the amount of available electrons. The samples being approximately 50 grams for the reduction, and having an average oxidation state of +3, and the metal ions at approximately 50% of the total mass, with an average molar mass of 56g/mol. This would mean that the ore could take a total of electrons is 0.05 mols of electrons which is considerably less than any of the compositions. However, having a higher partial pressure of reduction agents could increase activity, enabling new reactions. This is described in more detail in section 5.2.

Table 9: Gas-makeup used with the various reduction tests with calculated available electrons

Sample	Contents	Available electrons [mol]
1	$50\%Ar$ / $50\%CH_4$	32.1228
3	$40\%Ar$ / $50\%CH_4$ / $10\%H_2$	38.5474
2	$10\%Ar$ / $50\%CH_4$ / $40\%H_2$	33.7289
4	$100\%H_2$	16.0614

5.1.2 Discussion of experimental procedure

When performing the BET analysis, the samples had to be crushed down to a diameter of approximately 7mm in order to be able to fit the sample in the test tube. This affects the surface area of the sample and thereby the result of the BET analysis. However, if the internal surface area of the ore is considerably larger than the outer surface area this effect could be negligible. The literature on the raw polymetallic manganese nodules describes the specific surface area of the polymetallic nodules as between 100 - 150 m^2/g [3]. The BET analysis of the raw sample did not produce any readable data. However, the calcined sample indicated a surface area of approximately 2,25 m^2/g. This despite the porosity seemingly increasing during the calcination based on the SEM images, Figure 14 and 16. This could be explained by the pore growth causing an increase in pore size, increasing pore volume but reducing specific surface area [31]. The ore shrank in size during calcination, but such a large loss of surface area still seem unlikely. Further surface area analysis with larger sample size should be done in order to establish more reliable data.

When preparing the samples for XRF they were crushed in a disc mill. Something which became apparent during the crushing was the presence of a white inclusions within the ore. It was later assumed that these inclusions consisted of quartz SiO_2 and albite $NaAlSi_3O_8$, possibly encapsulated by the nodules form the sediment in which the polymetallic nodules grow. These inclusions could severely affect the measured levels of silicon within the samples. It is assumed that this is what causes the considerably high levels of silicon in the XRF analysis of the raw ore, while for the calcined ore it is at a level closer to both the literature and what is described by the supplier. In future experiments and possibly for future metal production, the removal of these inclusions could be done via mineral processing to reduce the levels of silicon in the ore for industrial processing and to analyze the samples more accurately.

The samples used in this thesis originates from the seafloor which is unconventional and may therefore contain phases not widely studied. This became apparent when attempting to analyze the XRD patterns of the raw and to a lesser degree calcined polymetallic nodules. The databases, although extensive, may not account for the slight variations of elements absorbed in the porous structure of the polymetallic nodules [3]. The diffraction pattern could also have shifted right or left during analysis as a result uniform strain in the sample. Non-uniform strain could also cause a widening of the peaks, and as the sample contains several phases, different peaks could overlap. This had to be accounted for when identifying the phases and may have introduced errors as a result of misjudgement. When identifying the peaks, multiple factors such as thermodynamics, EDX-mapping, and literature were utilized in order to minimize error in judgement and properly identify the correct phases. XRD is not a suitable analysis method for detecting very small phase concentrations in a sample. It is assumed that this is the reason for not being able to identify phases of cobolt or magnesium, which were of high interest for this thesis.

When casting the samples for SEM analysis, two different epoxies were used. These epoxies contained high amounts of carbon. This made assessing the carbon distribution of the samples with EDX unfeasible. Some of the pores which had been filled with the epoxy is clearly visible and it is highly likely that the epoxy may have contaminated some of the sample as to give elevated levels of carbon. After casting, the samples were coated in a layer of electrically conductive material. Carbon was used for the raw and calcined samples, and gold was used for coating the reduced samples. Comparing the SEM BEI images and EDX mapping of Figures 14-25 shows that although the BEI images illustrate distinct patterns and layers in the samples it does not necessarily translate to the EDX-mapping. This could be caused due to the larger volume of analysis for EDX thereby giving less resolution. This volume does also peer further into the sample than the backscattered electrons as shown in Figure 6, possibly blurring thin layers. As well as the different elements of iron and manganese is of a very similar atomic number appearing similar in the BET images.

5.2 Thermodynamics of gas reduction process

To get an understanding of what happens in this complex system during reduction, equilibrium diagrams for the reaction between 0-4 moles CH_4 and 1 mole Mn_2O_3, Fe_2O_3, Co_3O_4, NiO and CuO at 900°C. The diagrams were drawn using the Equilibrium compositions module in HSC Chemistry 9 as shown in Figures 30 - 32. The elements considered in these diagrams are Mn_2O_3, Mn_3O_4, MnO, Mn, Mn_3C, Mn_5C_2, Mn_7C_3, Fe_2O_3, Fe_3O_4, FeO, Fe, Fe_3C, Fe_5C_2, Fe_7C_3, NiO, Ni, CuO, Cu_2O, Cu, CoO, Co_3O_4 and Co. These figures show that when the concentration of methane is low CO_2 and H_2O gases is produced, as the CO and H_2 produced from methane being used as a reduction agent as shown in Equation (6), they are later used as reduction agents as shown in Equations (7) - (8). When more methane is introduced to the system the equilibrium concentrations of CO_2 and H_2O decreases while the concentrations of CO and H_2 increases, indicating incomplete reaction. The concentration of CO in the Mn_2O_3 (Figure 30), NiO (Figure 31), and CuO (Figure 32) systems stagnates at approximately 1 mole methane in the system. At the same point solid carbon start to form, indicating that methane begins to crack. Equation (1) show the cracking of methane.

Figure 30: Equilibrium amounts in moles of possible phases when 1 mole Mn_2O_3 reacts with 0-4 moles of CH_4 (g). Created using the Equilibrium calculations module in HSC chemistry 9.
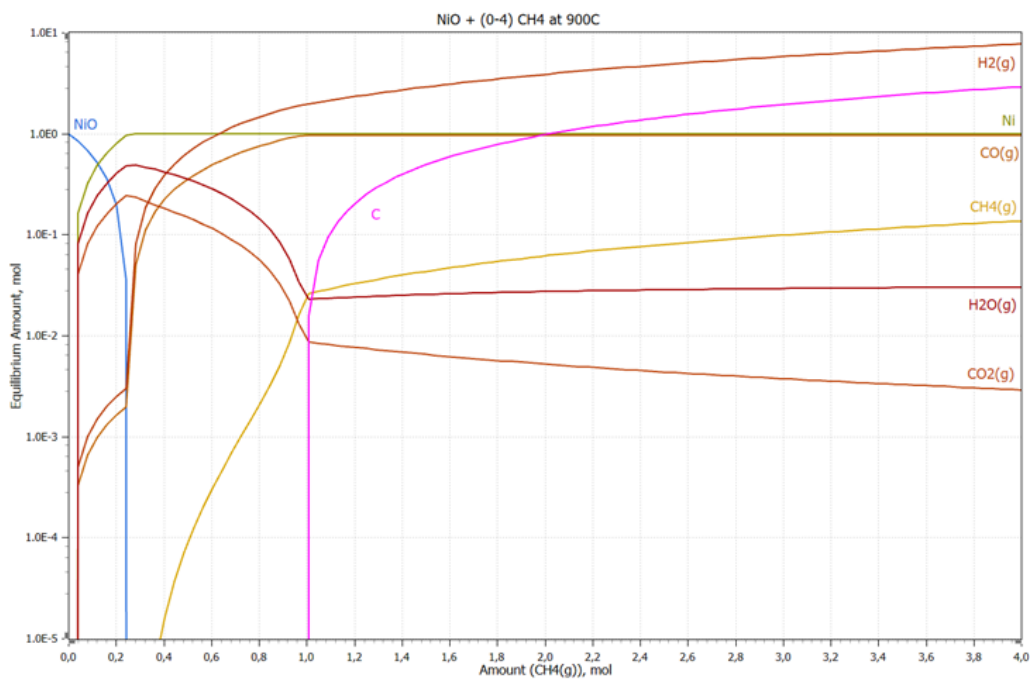
Figure 31: Equilibrium amounts in moles of possible phases when 1 mole NiO reacts with 0-4 moles of CH_4 (g). Created using the Equilibrium calculations module in HSC chemistry 9.
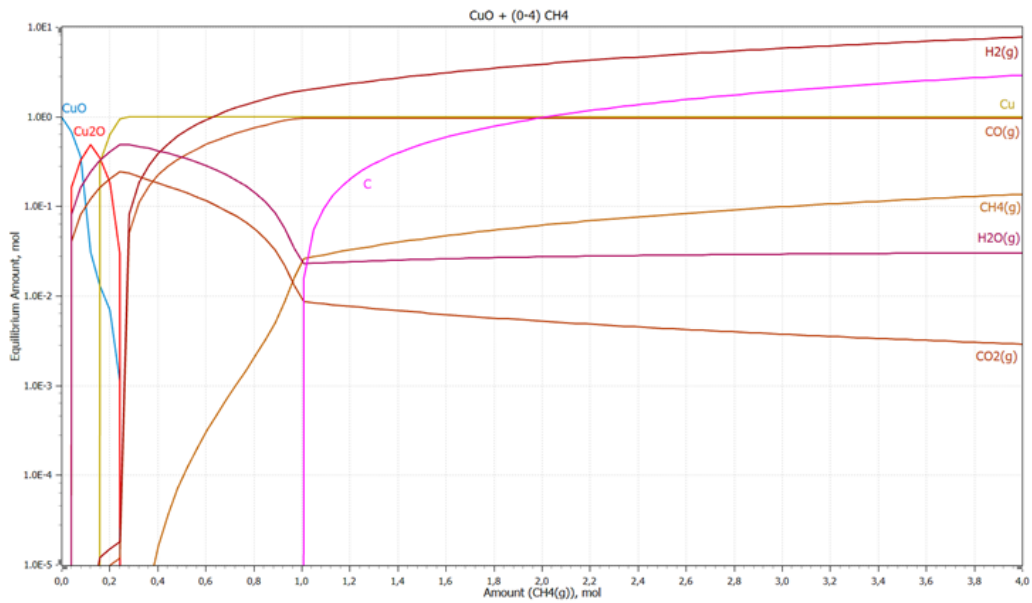
Figure 32: Equilibrium amounts in moles of possible phases when 1 mole CuO reacts with 0-4 moles of CH_4 (g). Created using the Equilibrium calculations module in HSC chemistry 9.

The reduction of Mn_2O_3 to MnO is described in Equation (3)-(4), Equation (18) describes the reduction of NiO to Ni, and Equation (19) describes the reduction of CuO to Cu. Only considering the reduction by methane described in Equation (6), it takes 1 mole methane to complete the reductions of 1 mole Mn_2O_3, NiO and CuO. This is indicative that reduction by methane will be prioritized, and methane will start to crack after no further reduction is possible. The equilibrium diagram for Co_3O_4 in Figure 33, is consistent with this. Co_3O_4 reduction to Co is described in Equation (16) - (17), when this reaction ends solid carbon begins to form.
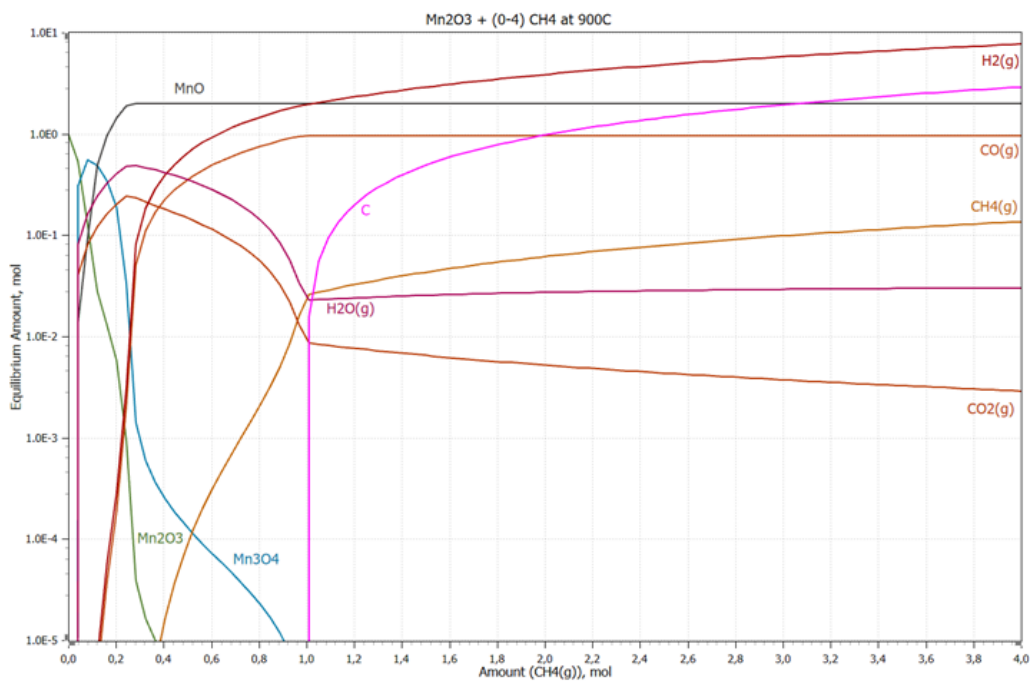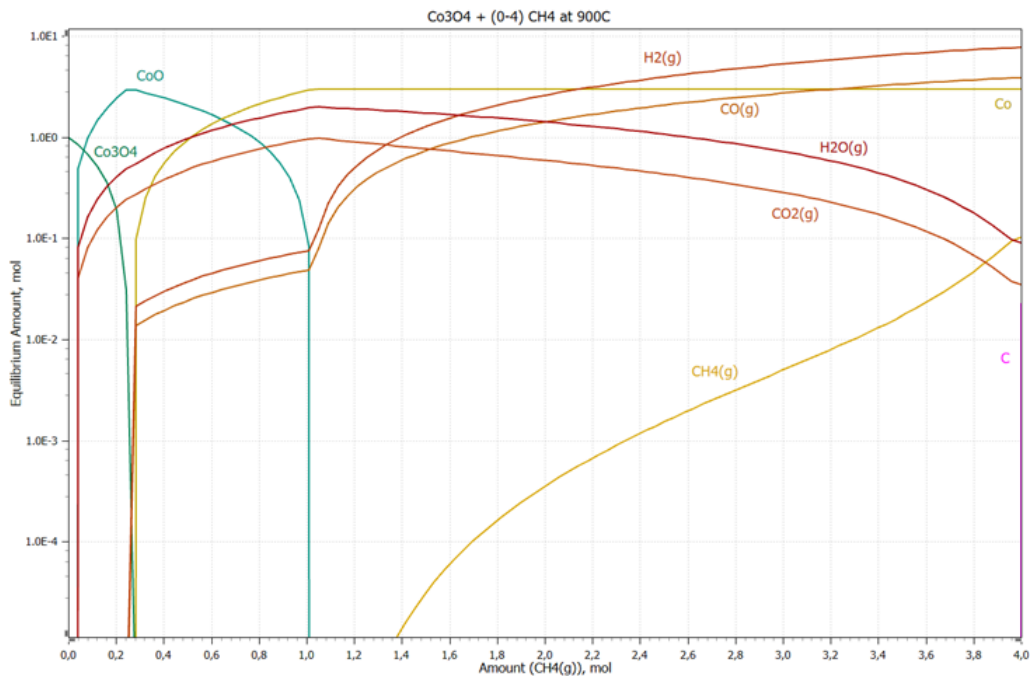

Figure 33: Equilibrium amounts in moles of possible phases when 1 mole Co_3O_4 reacts with 0-4 moles of CH_4 (g). Created using the Equilibrium calculations module in HSC chemistry 9

Fe, differ from the other elements. To reduce 1 mole Fe_2O_3 to Fe, Equation (10) - (12), by the methane reduction will take 3 moles methane. In the Fe_2O_3 equilibrium diagram, Figure 34, carbides start to form when there is about 2.9 moles methane in the system. The formation of carbides indicate methane cracking, and the solid carbon reacting with the iron, Equation (13) - (15). After all the iron has been converted to carbides there is a small gap before solid carbon forms at 3.8 moles methane in the system. In the gap the amount of Fe_3C decreases, while the concentration of Fe_5C_2 and Fe_7C_3 increases explaining where the excess carbon goes.
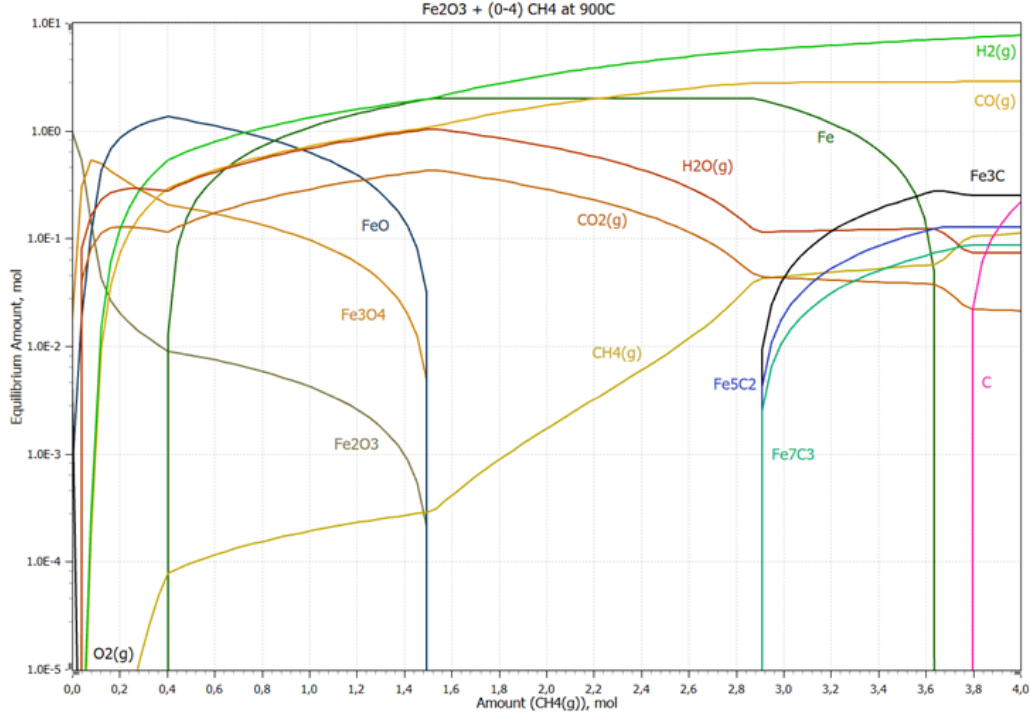
Figure 34: Equilibrium amounts in moles of possible phases when 1 mole Fe_2O_3 reacts with 0-4 moles of CH_4 (g). Created using the Equilibrium calculations module in HSC chemistry 9.

The equilibrium diagrams are useful for predicting the reactions that occur, but doesn't give information about how long it will take for the system to achieve equilibrium or how it is impacted by a more complex system. As for further reduction of MnO, CO has been reported to have a retarding effect [21]. Therefore, a equilibrium diagram with methane as reducing agent won't give a good indication on how MnO will react further as both reduction to Mn and reduction to manganese carbides produces CO as an off gas. These equilibrium diagrams, as shown in Figures 30 - 32 shows that reduction starts immediately when methane enters the system, but nothing about how long it will take. The equilibrium diagrams indicate that methane cracking occurs only after the reduction of the metal oxides has finished. This is because methane is a strong reduction agent, and the reduction by methane leads to lower ΔG than cracking of methane as shown in Figures 2 - 5.

For the reduction to MnO, Fe, Co, Ni, and Cu, the total ΔG is lower for the reduction than for the cracking of methane. The reduction product showed limited, if any, cracking of methane which had been adsorbed into the sample that could be detected with XRD. The EDX mapping as shown in Figures 19, 21, 23, and 25 indicated a high amount of carbon spread over the analyzed surface. This is, however, suspected of being contaminants from the epoxy used to prepare the samples. Some cracking could be observed as a layer of soot on the surface of the crucible.

5.3 Discussion of composition and microstructure

5.3.1 Raw ore

The peak for quartz in the x-ray diffraction pattern is significantly more intense than the peaks of the other phases including manganese, which is the main element. A possible reason for this is that the sample contained a high amount of quartz as a distinct phase. As well as the manganese residing in several different phases which all had less intense peaks.

Through the EDX mapping of the raw ore in Figure 15, there is only one phase that is easily identifiable. This is a phase consisting of Na, Si, Al and K. Such a phase was not identified in the XRD results, Figure 26. Albite has the chemical formula $NaAlSi_3O_8$, and potassium can replace up to 10% of sodium in albite [32] which may explain this phase. The XRF results, however, does not support that all the potassium resides in this phase. The EDX mapping also show that aluminium occurs together with silicon, but such a phase was not identified. Silicon is also present in more areas than aluminium. Another observation from the EDX mapping is manganese and iron residing in different phases, even though it isn't possible too see a clear distinction in the SEM image. This can be explained by the way backscatter images are made. As the molecular weight of manganese is 54.94 g/mol and molecular weight of iron is 55.85 g/mol only a very slight contrast will show.

5.3.2 Calcined ore

The diffraction pattern of the calcined ore, Figure 28, presents multiple interesting artifacts. One is the presence of wide bars of increased intensity between multiple peaks. A possible explanation for the wide bar observed in the XRD spectrum of the calcined ore could be incomplete mass transfer during the calcination. This might also explain why the highest peak was found to be manganese bearing magnetite if the mass transfer of manganese is incomplete and rather show many smaller peaks than one large. Several peaks are wide, possibly hiding smaller peaks beneath them. The widening of these peaks may be caused by inhomogeneous strain as described in the literature [25]. During calcination the ore shrank, which can be a cause for this strain. Apparent in the XRD spectrum is the presence of unidentified peaks, mainly at 44°, 58.5° and 60.5°. The main expected elements are already identified. The likely candidates for elements in these phases are therefore Si, Al Mg, Ca, and Ni.

Comparing the EDX mapping of the raw ore, Figure 15, with the EDX mapping of the calcined ore, Figure 17, it is evident that manganese has moved from being prominent in some areas in the raw ore, to being evenly distributed throughout the calcined ore. In the EDX mapping most of, if not all the silicon seem to appear in phases together with Na, Mg, Al and Ca, which are the main elements not identified by XRD. Compared to the raw ore, Na, Mg and Ca have concentrated more around the silicon in the calcined sample. No such phases were identified through the XRD analysis. However, a phase of quartz was found. As is evident from the XRF results of the raw ore from Dregerfors Laboratorium AB in Table 7, the amount of silicon through the polymetallic nodules can vary greatly. The inclusion of silicon in the form of quartz after calcination is still reasonable as it is also found in the XRD spectrum.

The EDX mapping also show copper in a few spots with small amounts of other elements. This indicates that copper somewhat has condensed together during calcination. As copper isn't reducible by heating in air to 900°C as shown in the Ellingham diagram for Co, Ni and Cu, Figure 5, a copper oxide phase, either Cu_2O or CuO is likely to occur in the calcined sample. The presence of copper oxide is supported by the x-ray diffraction identifying cuprite (Cu_2O).

In the TGA of the calcined ore shown in Figure 12, several drops in the mass loss curve were identified. A drop in the mass loss curve indicates an evaporative reaction beginning, a leveling of the curve indicates the reaction ending. Observing the TGA of the calcination of the raw ore 3 such drops can be seen. The first drop is found at approximately $100°C$, and can safely be assumed to be caused by the evaporation and decomposition of moisture and hydroxides. Hydroxides begin evaporation at higher temperatures, this may blur the contrast between the different reactions at lower temperature. The second identifiable drop occurs when the furnace reaches $400°C$, as this was the same temperature as SO_2 was detected, this drop is assumed to be caused by the decomposition of sulfides in the sample. Comparing the XRF data from the supplier, Table 2, with the XRF data received from Dregerfors of the calcined sample, Table 8, the sulphur content has decreased. The final drop occurs at approximately $650°C$ and is assumed to be caused by the partial reduction of the polymetallic nodules. This is supported by the Ellingham diagrams in Figures 2-5 and described by Equations (1)-(19).

5.3.3 Reduced ore

Manganosite is the most prominent phase identified under all the different atmospheres. As manganese is the most prevalent element in the ore, and not expected to reduce beyond this state, it is reasonable that this phase is highly prominent.

Fayalite and Tephroite, are two species of olivine with the chemical formulas Mn_2SiO_4 and Fe_2SiO_4 which form solid solution with an intermediate phase knebelite $FeMnSO_4$. These phases were identified in all of the reduced samples. Fayalite was best suited to the samples reduced under $40\%Ar$, $50\%CH_4$, $10\%H_2$ and $10\%Ar$, $50\%CH_4$, $40\%H_2$ atmosphere, while tephroite was best suited to the $50\%Ar$, $50\%CH_4$ and the $100\%H_2$ atmosphere. This indicates that the reduction atmosphere does not correlate to the resulting fayalite / tephroite phase. The prominent phase may therefore be caused by difference in ore composition. The intensity of the fayalite / teproite peaks is markedly lower in the two intermediary samples with a mixture of H_2 and CH_4 gas.

Iron is identified in all the reduced samples through XRD. The iron reduction is expected as it is described in the Ellingham and the equilibrium diagrams, Figures 3 and 34 respectively. A point of note is the precense of γ-iron or austenite in the sample reduced in an atmosphere of 40% Ar, 50% CH_4, 10% H_2. γ-iron is normally only stable at high temperatures, meaning that it should have returned to ferrite. As the sample was reduced in an intermediary of the two reduction gases, it is unlikely that the presence of this phase is caused by the reactants. A possible cause for this phase could, however, be the utilization of stabilizing elements such as nickel, manganese, or cobalt. The binding of these elements as a stabilizing agent could also explain the reduced levels of identified copper nickel phases in the same sample. [33] Cobalt was not identified in any of the phases in the x-ray diffraction analysis, however, viewing the EDX analysis in Figures 19, 21, 23, and 25, although faintly, cobalt can be seen correlating with iron. In Figure 5 cobalt can be seen reducing to it's metallic state at temperatures above $525°C$. This could indicate that the small amount of cobalt present was reduced and entered phase with iron, thereby not being identifiable by XRD.

The EDX analysis was not able to properly identify carbon in the sample and gave high values of carbon spread widely over the surface, as can be seen in the EDX Mapping of the reduced samples as shown in Figures 19, 21, 23, and 25. The high occurrence of carbon may be contamination from the epoxy used in sample preparation.

Cheragi et al. [22] have reported to find cementite, $(Fe, Mn)_3C$, in low grade manganese ore after reduction under a gas flow of 1 NL Ar and 1 NL CH_4 at 900°C for 60 minutes. It was therefore expected to be identified. Figure 4 shows that iron reacts with carbon to form iron carbide at temperatures above 875°C placing the temperature used for these experiments on the edge of spontaneous reaction. Iron carbide, or manganese carbide in the form of cementite was not identified, although, may be present in quantities to small to be identifiable. The TGA in Figure 13 show that the reduction reactions complete quickly after reduction agents are introduced, giving ample time for methane to crack. Cracking of methane became evident by soot collecting on the crucible. However, the lack of solid carbon or cementite in the XRD analysis was a surprising result and could be a caused by inaccessibility for the carbon through the pores. However, beyond the theory, the reason for this is unexplained.

Visible in all the XRD spectrum were the presence of copper nickel in metallic form. The reduction atmosphere seemed to have little to no effect on the nickel copper. This is result was expcted as the copper and nickel is easily reducable and easily forms a solid solution with eachother. It is not necessary that these two are in phase with each other, but the two can form a solid solution and can be hard to separately identify via XRD [31]. As shown in Figure 29 the copper nickel peak visibly less prominent in the sample reduced in an atmosphere og 40% Ar, 50%CH_4, 10%H_2. This could be caused by the elements entering phase with iron stabelizing the austnite, or it could originate from a separate unknown cause.

Nepheline with the formula $(Na, K)AlSi_4$ is another phase identified in all the reduced samples. The EDX-maps of the corroborate the presence of nepheline, as it shows the elements sodium, aluminium and silicon appear alongside each-other as shown in Figure 19, 21, 23, and 25. In his paper H. Winkler "on the synthesis of nepheline" [34] describes a simple production path for nepheline in which a compound with an approximate relation of Na_2O: Al_2O_3: SiO_2 = 1:1:2, and heated to a temperature below 1200 °C. This process is similar to the calcination process performed in this thesis. Nepheline was not clearly identified in the calcined sample due to high levels of noise, but it is possible the phase was generated during the calcination. This phase may also explain where the aluminium and potassium is residing after the reduction.

The formation of fayalite is spontaneous at higher temperatures under a reducing atmosphere [35]. Given it's similarities this is also expected to be the case for tephorite. Silicon did not entering phase with other elements as seen in the sample reduced in an atmosphere of 40%Ar, 50%CH_4, 10%H_2 could be caused by a large presence of quarts in the raw sample ore, perhaps from the same inclusions as described previously. The transport of silicon atoms from these inclusions would be limited by the mass transport of elements, and could therefore keep the quartz unchanged. This could be due to the inclusions having poor mass transport, or possibly another factor hindering the silicon from entering a phase with other elements.

The 100%H_2 and the 50%Ar, 50%CH_4 have very similar XRD patterns. This indicates that the same reductions take place, and since there are no carbon available in the 100%H_2 and there is limited to no formation of carbides in the 50%Ar, 50%CH_4 there is believed to be minimal differences between the different reduction atmospheres. The gas composition that stands out are the 40%Ar, 50%CH_4, 10%H_2, where the iron has gone over into another phase.

The similarities between the different gas mixtures can mainly be explained by the temperature. At 900° methane and hydrogen are both able to do the same reductions. While Fe, Co, Ni and Cu are able to be reduced to metallic states at this temperature, Figure 3 and 5, this isn't possible for Mn. As can be seen from Figure 2, MnO is almost reducable to Mn at 1000° by methane, that isn't the case with the hydrogen reduction.

6   Conclusion

In this research polymetallic manganese nodules were characterized, and their calcination and reduction behavior by H_2 and CH_4 gasesand their mixtures were studied. The main conclusions can be summarized as:

- The polymetallic manganese nodules were found to have a highly complex microstructure consisting of several phases.
- In the polymetallic manganese nodules and iron were found to mostly reside in different phases.
- Polymetallic manganese nodules will produce metallic iron, nickel, and copper when reduced at 900°C in an environment with readily available reactants of either methane or hydrogen gas. Phases of cobalt was not identified, but is theoretically reduced to a metallic state, and may have alloyed with another metal.
- No carbide was found in the samples reduced by methane-containing gases
- Manganese oxides were not identified to be reduced beyond manganosite.
- Silicon content of the ore greatly affected the reduced samples, binding elements of manganese and iron into phases of fayalite and tephorite.
- The silicon contribution in the polymetallic nodules appears to originate form inclusions in the nodules which can be visually identified as white stones.
- Phosphine gas is not generated from this sample selection of polymetallic manganese nodules.
- The increase in porosity of the manganese nodules during calcination allows for easy mass transport of reactants and gaseous reduction products, possibly allowing for processing without a pelletization stage.
- The reaction speed of the reduction is significant and appear exothermic in nature.

Bibliography

[1] Fotiou S, Akenji L, Bengtsson M, Schandl H, Salem J, Briggs E, et al. Sustainable Consumption and Production: A Handbook for Policy Makers; 2015.

[2] Cronan DS. Deep sea minerals;. Available from: https://www.geolsoc.org.uk/Geoscientist/Archive/September-2015/Deep-sea-minerals.

[3] Sharma R, et al. Deep-Sea Mining. Springer Cham; 2017.

[4] Halada K, Shimada M, Ijima K. Forecasting the Consumption of Metals up to 2050. Journal of The Japan Institute of Metals - J JPN INST METAL. 2007 10;71:831–839.

[5] Mandovà H, Vass T, Pales AF, Levi P, Gül T. The challenge of reaching zero emissions in heavy industry;. Available from: https://www.iea.org/articles/the-challenge-of-reaching-zero-emissions-in-heavy-industry.

[6] Bimbo N, Sharpe J, Noguera Diaz A, Physick A, Holyfield L, Rowlandson J, et al. Fuel Gas Storage: The Challenge of Hydrogen; 2014. ChemEngDayUK 2014 ; Conference date: 07-04-2014 Through 08-04-2014.

[7] the SSAB press team. HYBRIT recieves support from the EU Innovation Fund;. Available from: https://mb.cision.com/Main/980/3538183/1558277.pdf.

[8] Safarian J. A Sustainable Process to Produce Manganese and Its Alloys through Hydrogen and Aluminothermic Reduction. Processes. 2021 12;10:27.

[9] Ministry of Finance. Long-term Perspectives on the Norwegian Economy 2021. Stortinget; 2021. 14 (2020-2021). Available from: https://www.regjeringen.no/contentassets/91bdfca9231d45408e8107a703fee790/en-gb/pdfs/stm202020210014000engpdfs.pdf.

[10] Energy R. Marine Minerals. Rystad Energy; 2020.

[11] Bohrmann G, Abelmann A, Gersonde R, Hubberten H, Kuhn G. Pure siliceous ooze, a diagenetic environment for early chert formation. Geology. 1994 03;22(3):207–210. Available from: https://doi.org/10.1130/0091-7613(1994)022⟨0207:PSOADE⟩2.3.CO;2.

[12] Usui A, Hino H, Suzushima D, Tomioka N, Suzuki Y, Sunamura M, et al. Modern precipitation of hydrogenetic ferromanganese minerals during on-site 15-year exposure tests. Scientific Reports. 2020 02;10:3558.

[13] Gonon M. In: Case Studies in the X-ray Diffraction of Ceramics; 2020. .

[14] Hein J, Koschinsky A. Deep-ocean ferromanganese crusts and nodules. Geochemistry of Mineral Deposits: Treatise of Geochemistry, 2nd Edition. 2014 01;13:273–291.

[15] McLennan SM. In: Rare earth elements in sedimentary rocks: Influence of provenance and sedimentary processes; 2019. p. 169–200.

[16] the editors of Encyclopaedia. hydrometallurgy;. Available from: https://www.britannica.com/technology/hydrometallurgy.

[17] the editors of Encyclopaedia. pyrometallurgy;. Available from: https://www.britannica.com/technology/pyrometallurgy.

[18] Randhawa N, Hait J, Jana R. A brief overview on manganese nodules processing signifying the detail in the Indian context highlighting the international scenario. Hydrometallurgy. 2016 10;165:166–181.

[19] Sommerfeld M, Friedmann D, Kuhn T, Friedrich B. "Zero-Waste": A Sustainable Approach on Pyrometallurgical Processing of Manganese Nodule Slags. Minerals. 2018 11;8:544.

[20] Cheraghi A, Yoozbashizadeh H, Safarian J. Gaseous Reduction of Manganese Ores: A Review and Theoretical Insight. Mineral Processing and Extractive Metallurgy Review. 2019 08;41(3).

[21] Anacleto N, Ostrovski O, Ganguly S. Reduction of Manganese Oxides by Methane-containing Gas. ISIJ International. 2004 01;44:1480.

[22] Cheraghi A, Yoozbashizadeh H, Ringdalen E, Safarian J. Kinetics and Mechanism of Low-Grade Manganese Ore Reduction by Natural Gas. Metallurgical and Materials Transactions B. 2019 08;50:1566–1580.

[23] Coats AW, Redfern JP. Thermogravimetric analysis. A review. Analyst. 1963;88:906–924. Available from: http://dx.doi.org/10.1039/AN9638800906.

[24] the editors of Encyclopaedia. X-ray diffraction;. Available from: https://www.britannica.com/science/X-ray-diffraction.

[25] Speakman SA. Introduction to X-Ray Powder Diffraction Data Analysis;. Available from: http://prism.mit.edu/xray/documents/2%20Introduction%20to%20XRPD%20Data%20Analysis.pdf.

[26] the editors of Encyclopaedia. fluorecence;. Available from: https://www.britannica.com/science/fluorescence.

[27] Bradbury S, Joy DC, Ford BJ. scanning electron microscope;. Available from: https://www.britannica.com/technology/scanning-electron-microscope.

[28] Lewis DB. Scanning Electron Microscopy and X-ray Microanalysis. Transactions of the IMF. 1992;70(4):198–202. Available from: https://doi.org/10.1080/00202967.1992.11870972.

[29] Gavrilenko E. SEM-EDS/WDS analysis;. Available from: https://www.gems-inclusions.com/inclusions-studies/analytical-methods/sem-eds-wds-analysis/.

[30] the editors of Mrecer-instruments. he BET method for measurement of surface area.;. Available from: https://mercer-instruments.com/en/applications/BET-surface-area-analysis.html.

[31] Barnett SJ, Macphee DE, Lachowski EE, Crammond NJ. XRD, EDX and IR analysis of solid solutions between thaumasite and ettringite;.

[32] the editiors of mindat org. Albite;. Available from: https://www.mindat.org/min-96.html.

[33] the editors of Materials Today. Effect of Alloying elements in Steel, TTT diagram and Phase transformation diagram;. Available from: https://materials-today.com/effect-of-alloying-elements-in-steel/.

[34] Winkler HGF. On the synthesis of nepheline*. American Mineralogist. 1947 04;32(3-4):131–136.

[35] Wang Z, Peng B, Zhang L, Zhao Z, Liu D, Peng N, et al. Study on Formation Mechanism of Fayalite (Fe2SiO4) by Solid State Reaction in Sintering Process. JOM. 2017;70:539–546.

Appendix

[Appedix to come]

A Risk Assessment

RISK ASSESSMENT (RiskManager alternative)

Unit/Institute:	Department of Materials Science and Engineering		Date:	01.02.2022
Responsible line manager (name):	Einar Magne Hjorthol		Revised:	04.02.2022
Responsible for activities being risk assessed (name):	Jafar Safarian			
Participants in the risk assement (names):	Ole Kristian Brustad, Jonas Låstad, Arman Hoseinpur Kermani			

Description of the activity, process, area, etc.:

Ore and ore powder handeling, powder crushing, calcination and heat treatment, and prereduction in furnace. Testing using SEM, XRD, XRF, TG/DTA, and BET porosity measurement. Laberatories at NTNU department of material science, Kalvskinnet and gløshaugen.

Activity / process	Unwanted incident	Existing risk reducing measures	Probability (P)	Consequence (C) Evaluate the categories individualley. *Health should always be evaluated.*				Risk value (P x C)	Risk reducing measures - suggestions Measures reducing the probability of the unwanted incident happening should be prioritized.	Residual risk after measures being implemented (S x K)
			(1-5)	Health (1-5)	Material values (1-5)	Environment (1-5)	Reputation (1-5)			
Handeling natural ore, and test samples.	Contamination, damage to, or loss of specimen	Catuion when handeling test samples and ore not for use.	1	1	2	1	1	1	Avoid handeling the specimen unnecessarily.	1
Crushing the ore.	Heavy machinery can cause physical injury or damage to equipment.	Protective gear: Lab shoes, gloves, glasses.	1	3	2	1	1	3	Know the machine well and how to use it.	2
Handeling of fine ore powder.	Spill which means inhailing or contact with the substance on the skin or in the eye which can cause seroius internal injury.	Protective gear: gloves, lab coat, glasses and respiratory protection. Fume hood as a barrier and ventilation.	1	1	1	1	1	1	Always use lids that can fully keep the substance sealed in when transporting the material from one station to another.	1
Firing furance for calcination	High temperatures which can cause burn damage.	Protective gear: Heat resistant gloves, lab coat and glasses for protection. Tongs to avoid direct contact with the heat from the container. Brushes or ventialtors for cleaning the furance making sure that nothing unwanted is in the furance. Lab rules clearly state that you need to know the material you are working with.	1	3	1	1	1	3	Let it cool down in the furance for extra saftey.	1
Firing furance for calcination	Development of toxic gasses due to decomposition of ore.	Testing for potential phosphene generation. Personal phosphene detectors. Fumehood and protective masks when working with samples. Avoiding bystanders when handeling samples.	1	4	1	1	2	4	Preparing a test sample before heating the main batch.	2
Handeling of samples producing toxic gases in contact with water (if applicable)	Uncontained development of phosphine gas	Testing for potential phosphene generation. Personal phosphene detectors. Fumehood and protective masks when working with samples. Avoiding bystanders when handeling samples.	1	4	1	2	3	4	The samples were tested for toxic gases evolution in fume hood, and they were safe.	2
Storage of samples producing toxic gases in contact with water. (if applicable)	Development and leakage of phosphene gas in storage container	Dedicated storage containers and locations. Using detectors when opening the containers	1	4	1	2	3	4	The samples were tested for toxic gases evolution in fume hood, and they were safe.	3
Reduction step with samples producing toxic gases (if applicable)	Development and release of phosphene during reduction step	Using Dräger tubes, fumehood and protective masks when opening the furnace. Avoiding bystanders when handeling samples. Flushing the furnace with Ar before opening	1	4	1	2	3	4	Reductive gas flashing and checking the connections for no gas leackage, check the bubbling of gas in the connected water/oil bottle to the gas outlet.	2

Sample preparation for SEM	Epoxy vapours development	Working in fume hood until polymerized	1	1	1	1	1	1		1
Cross sectioning and milling for analyses (SEM, XRF, XRD).	Cuts and fragments of the meterial beeing shot outwards from the cross scetioning and milling machines.	Protective gear: Gloves, face mask, ventilation, safety glasses.	2	2	1	1	1	4		2
Handeling of liquid nitrogen	Spillage of liquid nitrogen, frost bite from cold objects	A face shield and isolated gloves are used when filling the liquid container.	1	1	1	1	1	1		
Reduction experiment in a ReSiNa furnace using gas flow.	Burn damage from high temperatures and risk of explosions. Gas suffication from odorless and colorless gas or gas poisoing from leakage. High pressure gas in which can cause explosions in high temperatures or in direct sunlight when in gas tank/bottle.	Protective gear: Heat resistant gloves, as the resina furance is relativly safe, a lab coat and glasses are fine. Built in alarm system in the lab for when concentration of gas excedes a certain unsafe limit. Personal mobile gas detector. Leak detector and pressure test to know if something is leaking. Ask the people who are certified to move the bottles to do it(Always use a gas trolley, remove the regulator, avoid sunlight and do not take the elevator when transporting the gas bottles). Warning signs on the door. Flushing the chamber after the experiment with vacuuming and then filling the chamber with Ar and then opning the chmaber. checkig the gas atmosphere arround the gas burner of the RESINA furnace from time to time to measure the posionous gases (this can be done by gas detectors or Dräger tubes)	1	3	2	1	1	3	Be familliar with the gas and regulators. Hightened caution when handeling dangerous equipment.	2
any lab activity and presence in the department	risk of spreading COVID 19	Sticking to the COVID 19 measures released by the HSE responsible people in our department. Booking the labs before using them. Keeping the COVID 19 safe distance and using masks if there is a crowd arround.	1	1	1	1	2	1		1

B   BET analysis

Sample: BET
Operator:
Submitter:
File: C:\data\Jonas L\MNNodCal1.SMP

Started: 3/31/2022 1:48:49 PM	Analysis adsorptive: N2
Completed: 3/31/2022 4:17:35 PM	Analysis bath temp.: -195,850 °C
Report time: 4/1/2022 8:40:10 AM	Thermal correction: No
Sample mass: 1,7984 g	Ambient free space: 16,2355 cm³ Measured
Analysis free space: 56,1304 cm³	Equilibration interval: 5 s
Low pressure dose: None	Sample density: 1,000 g/cm³
Automatic degas: No	

Summary Report

Surface Area

Single point surface area at p/p° = 0,299081967: 2,2240 m²/g

BET Surface Area: 2,2476 m²/g

Sample: BET
Operator:
Submitter:
File: C:\data\Jonas L\MNNodCal1.SMP

Started: 3/31/2022 1:48:49 PM
Completed: 3/31/2022 4:17:35 PM
Report time: 4/1/2022 8:40:10 AM
Sample mass: 1,7984 g
Analysis free space: 56,1304 cm³
Low pressure dose: None
Automatic degas: No

Analysis adsorptive: N2
Analysis bath temp.: -195,850 °C
Thermal correction: No
Ambient free space: 16,2355 cm³ Measured
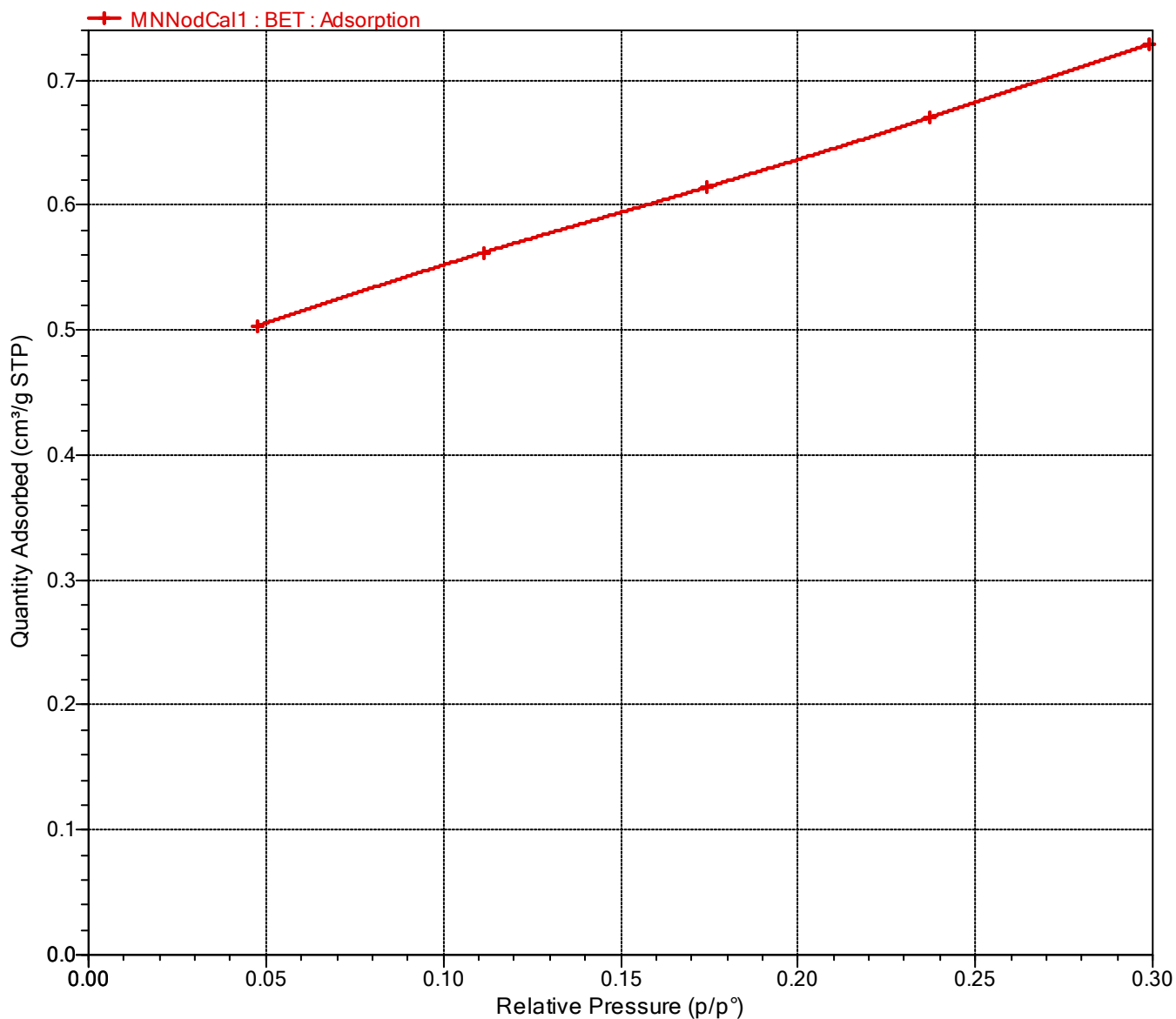Equilibration interval: 5 s
Sample density: 1,000 g/cm³

Isotherm Tabular Report

Relative Pressure (p/p°)	Absolute Pressure (mmHg)	Quantity Adsorbed (cm³/g STP)	Elapsed Time (h:min)	Saturation Pressure (mmHg)
			01:46	762.722290
0.047654738	36.369553	0.5034	02:08	763.188599
0.111672974	85.226273	0.5622	02:10	763.177246
0.174151132	132.914963	0.6145	02:13	763.216187
0.237337738	181.147507	0.6701	02:15	763.247803
0.299081967	228.290466	0.7290	02:17	763.304016

Sample: BET
Operator:
Submitter:
File: C:\data\Jonas L\MNNodCal1.SMP

Started: 3/31/2022 1:48:49 PM	Analysis adsorptive: N2
Completed: 3/31/2022 4:17:35 PM	Analysis bath temp.: -195,850 °C
Report time: 4/1/2022 8:40:10 AM	Thermal correction: No
Sample mass: 1,7984 g	Ambient free space: 16,2355 cm³ Measured
Analysis free space: 56,1304 cm³	Equilibration interval: 5 s
Low pressure dose: None	Sample density: 1,000 g/cm³
Automatic degas: No	

Isotherm Linear Plot

Sample: BET
Operator:
Submitter:
File: C:\data\Jonas L\MNNodCal1.SMP

Started: 3/31/2022 1:48:49 PM	Analysis adsorptive: N2
Completed: 3/31/2022 4:17:35 PM	Analysis bath temp.: -195,850 °C
Report time: 4/1/2022 8:40:10 AM	Thermal correction: No
Sample mass: 1,7984 g	Ambient free space: 16,2355 cm³ Measured
Analysis free space: 56,1304 cm³	Equilibration interval: 5 s
Low pressure dose: None	Sample density: 1,000 g/cm³
Automatic degas: No	

Isotherm Log Plot

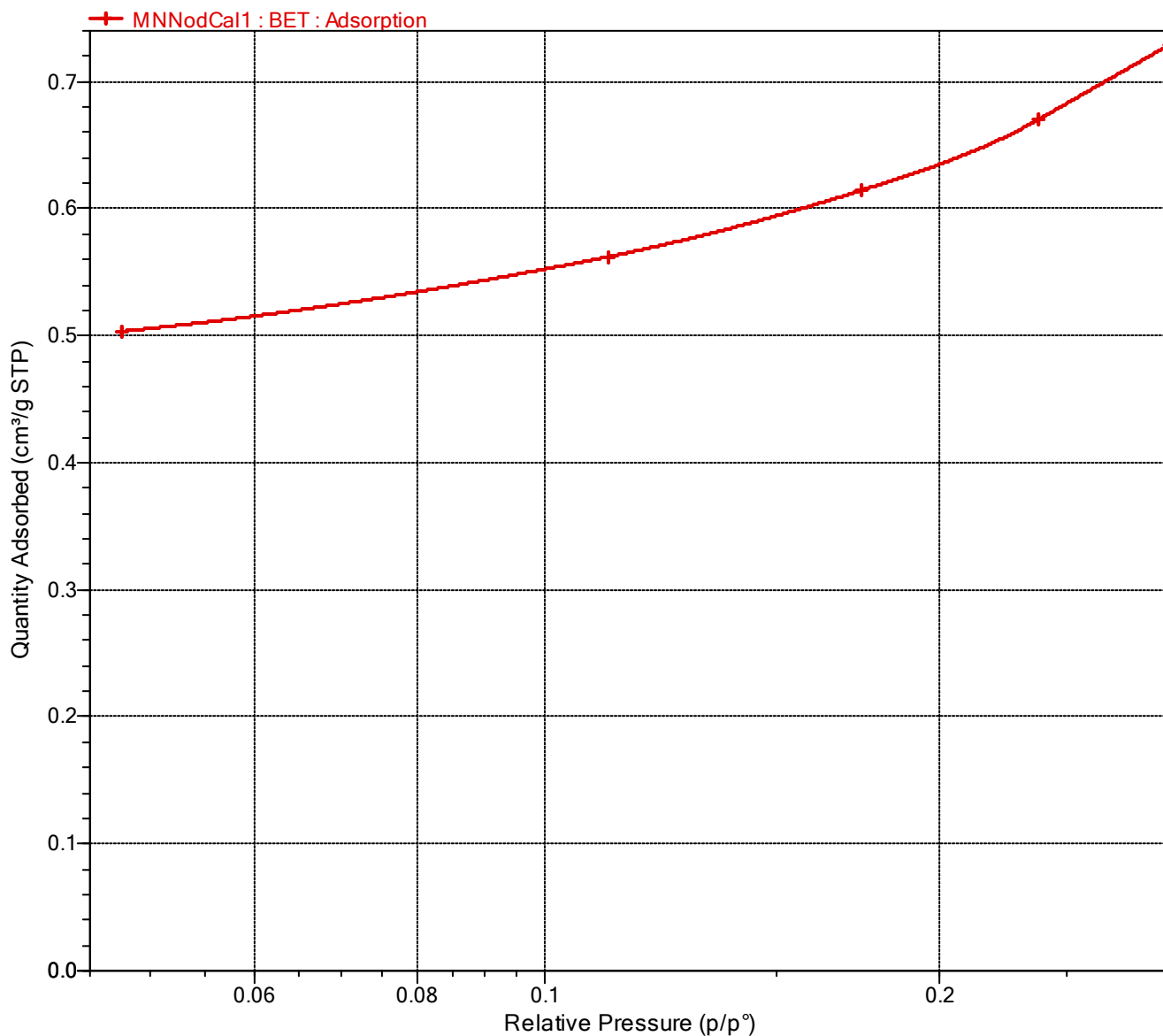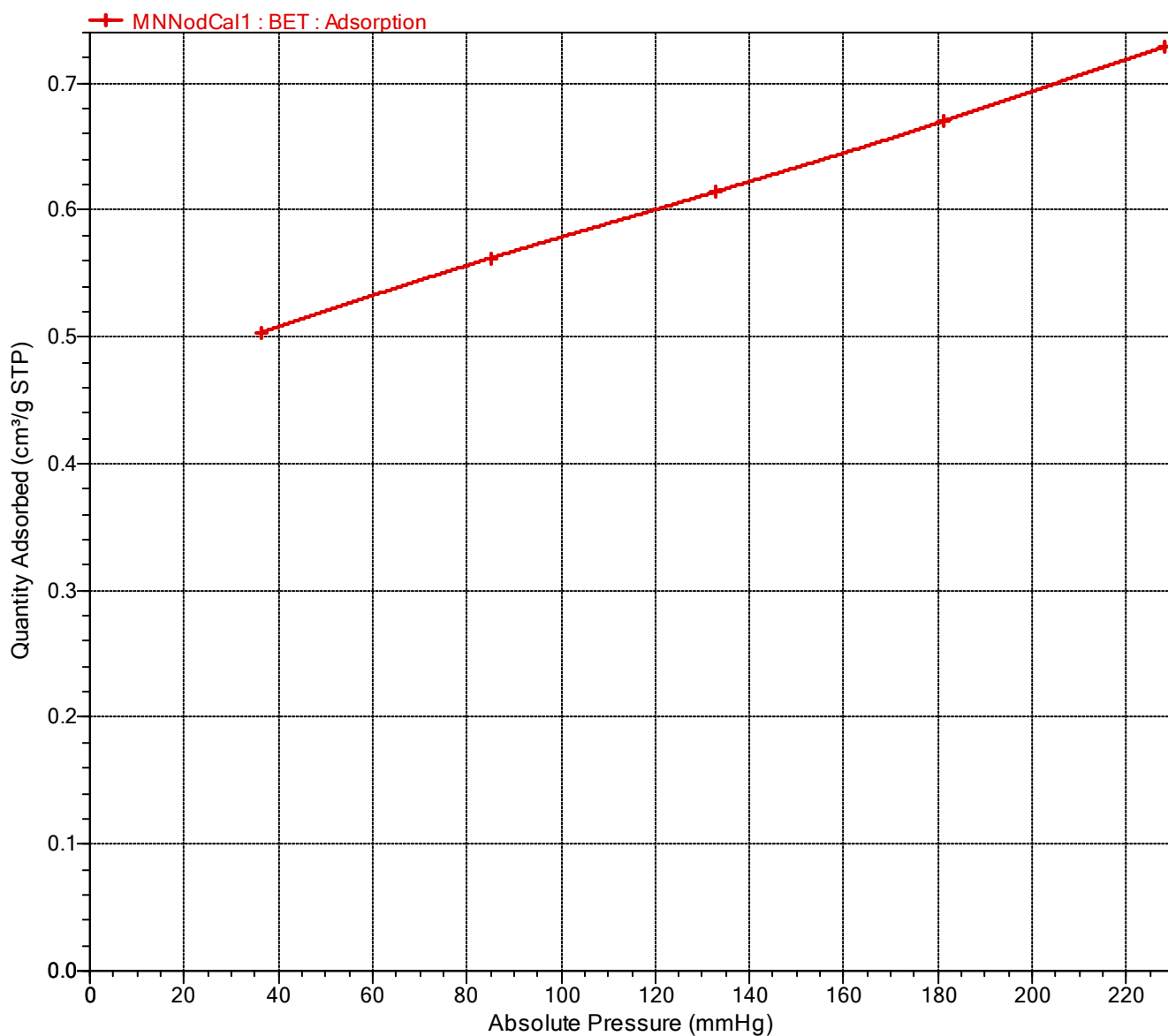— MNNodCal1 : BET : Adsorption

Sample: BET
Operator:
Submitter:
File: C:\data\Jonas L\MNNodCal1.SMP

Started: 3/31/2022 1:48:49 PM
Completed: 3/31/2022 4:17:35 PM
Report time: 4/1/2022 8:40:10 AM
Sample mass: 1,7984 g
Analysis free space: 56,1304 cm³
Low pressure dose: None
Automatic degas: No

Analysis adsorptive: N2
Analysis bath temp.: -195,850 °C
Thermal correction: No
Ambient free space: 16,2355 cm³ Measured
Equilibration interval: 5 s
Sample density: 1,000 g/cm³

Isotherm Linear Absolute Plot

MNNodCal1 : BET : Adsorption

mi micromeritics®

Sample: BET
Operator:
Submitter:
File: C:\data\Jonas L\MNNodCal1.SMP

Started: 3/31/2022 1:48:49 PM	Analysis adsorptive: N2
Completed: 3/31/2022 4:17:35 PM	Analysis bath temp.: -195,850 °C
Report time: 4/1/2022 8:40:10 AM	Thermal correction: No
Sample mass: 1,7984 g	Ambient free space: 16,2355 cm³ Measured
Analysis free space: 56,1304 cm³	Equilibration interval: 5 s
Low pressure dose: None	Sample density: 1,000 g/cm³
Automatic degas: No	

Isotherm Log Absolute Plot
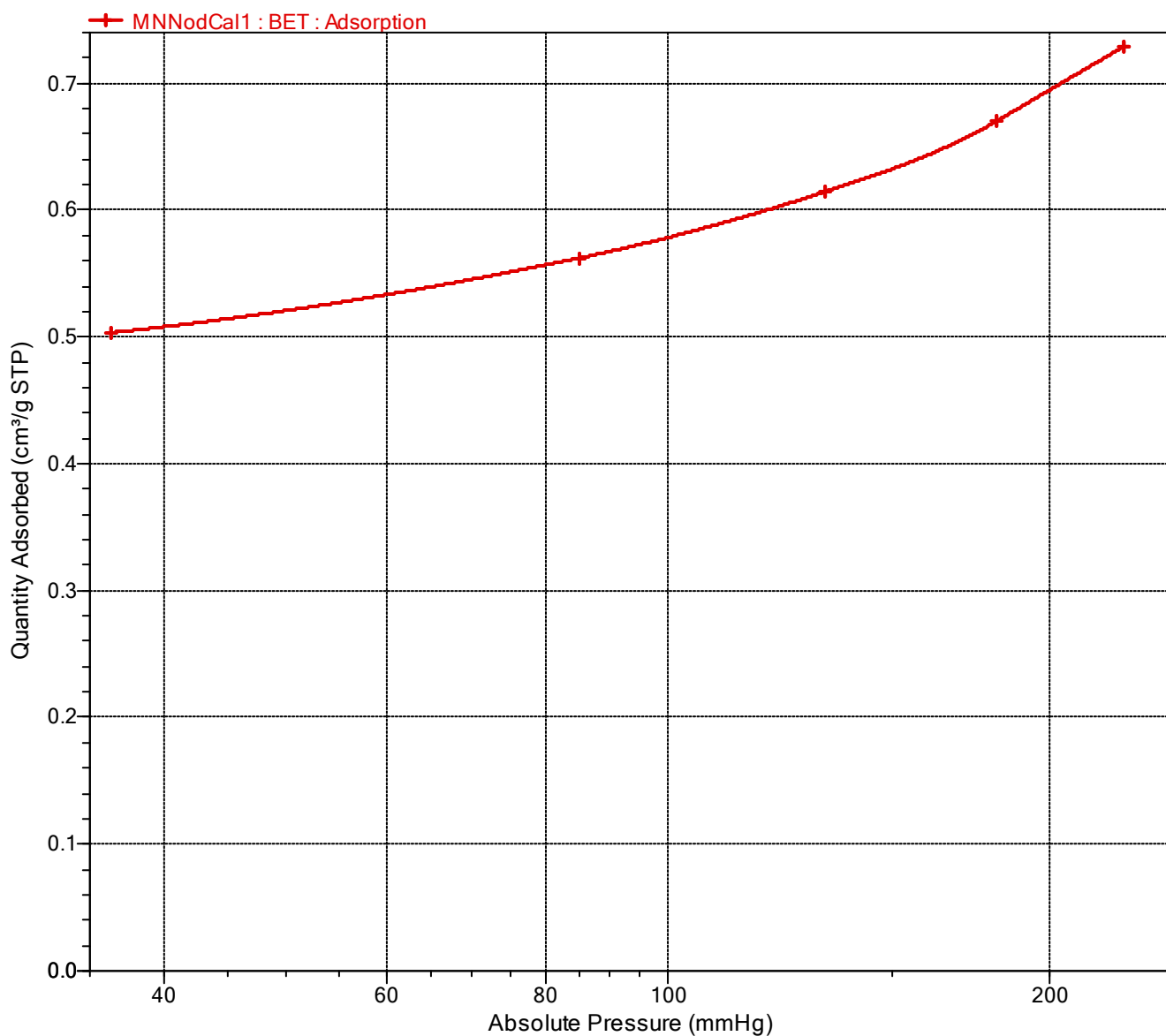
— MNNodCal1 : BET : Adsorption

Sample: BET
Operator:
Submitter:
File: C:\data\Jonas L\MNNodCal1.SMP

Started: 3/31/2022 1:48:49 PM	Analysis adsorptive: N2
Completed: 3/31/2022 4:17:35 PM	Analysis bath temp.: -195,850 °C
Report time: 4/1/2022 8:40:10 AM	Thermal correction: No
Sample mass: 1,7984 g	Ambient free space: 16,2355 cm³ Measured
Analysis free space: 56,1304 cm³	Equilibration interval: 5 s
Low pressure dose: None	Sample density: 1,000 g/cm³
Automatic degas: No	

Isotherm Pressure Composition
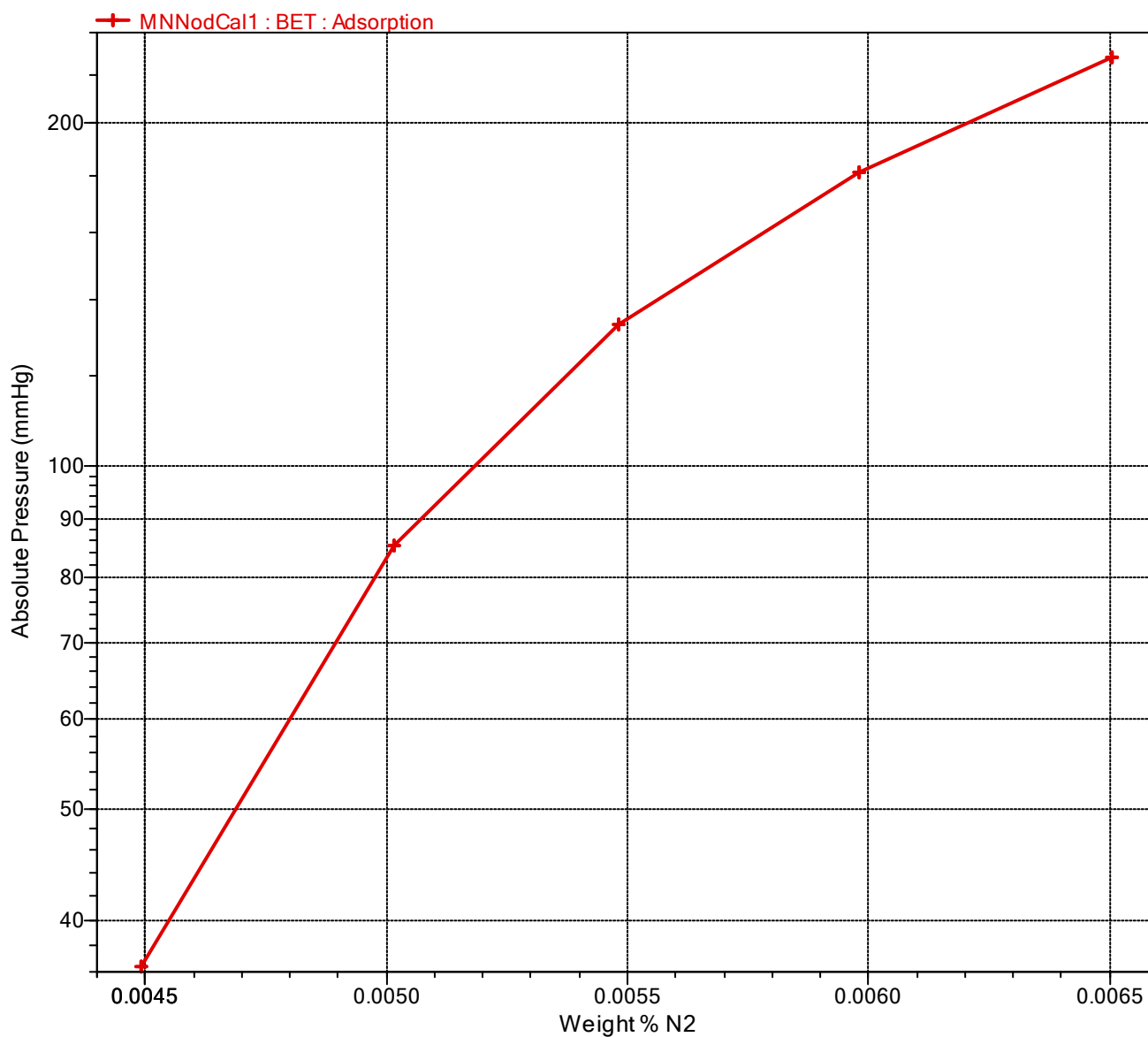

MNNodCal1 : BET : Adsorption

Sample: BET
Operator:
Submitter:
File: C:\data\Jonas L\MNNodCal1.SMP

Started: 3/31/2022 1:48:49 PM
Completed: 3/31/2022 4:17:35 PM
Report time: 4/1/2022 8:40:10 AM
Sample mass: 1,7984 g
Analysis free space: 56,1304 cm³
Low pressure dose: None
Automatic degas: No

Analysis adsorptive: N2
Analysis bath temp.: -195,850 °C
Thermal correction: No
Ambient free space: 16,2355 cm³ Measured
Equilibration interval: 5 s
Sample density: 1,000 g/cm³

BET Report

BET surface area: 2,2476 ± 0,0090 m²/g
Slope: 1,928894 ± 0,007556 g/cm³ STP
Y-intercept: 0,007615 ± 0,001641 g/cm³ STP
C: 254,299612
Qm: 0,5164 cm³/g STP
Correlation coefficient: 0,9999847
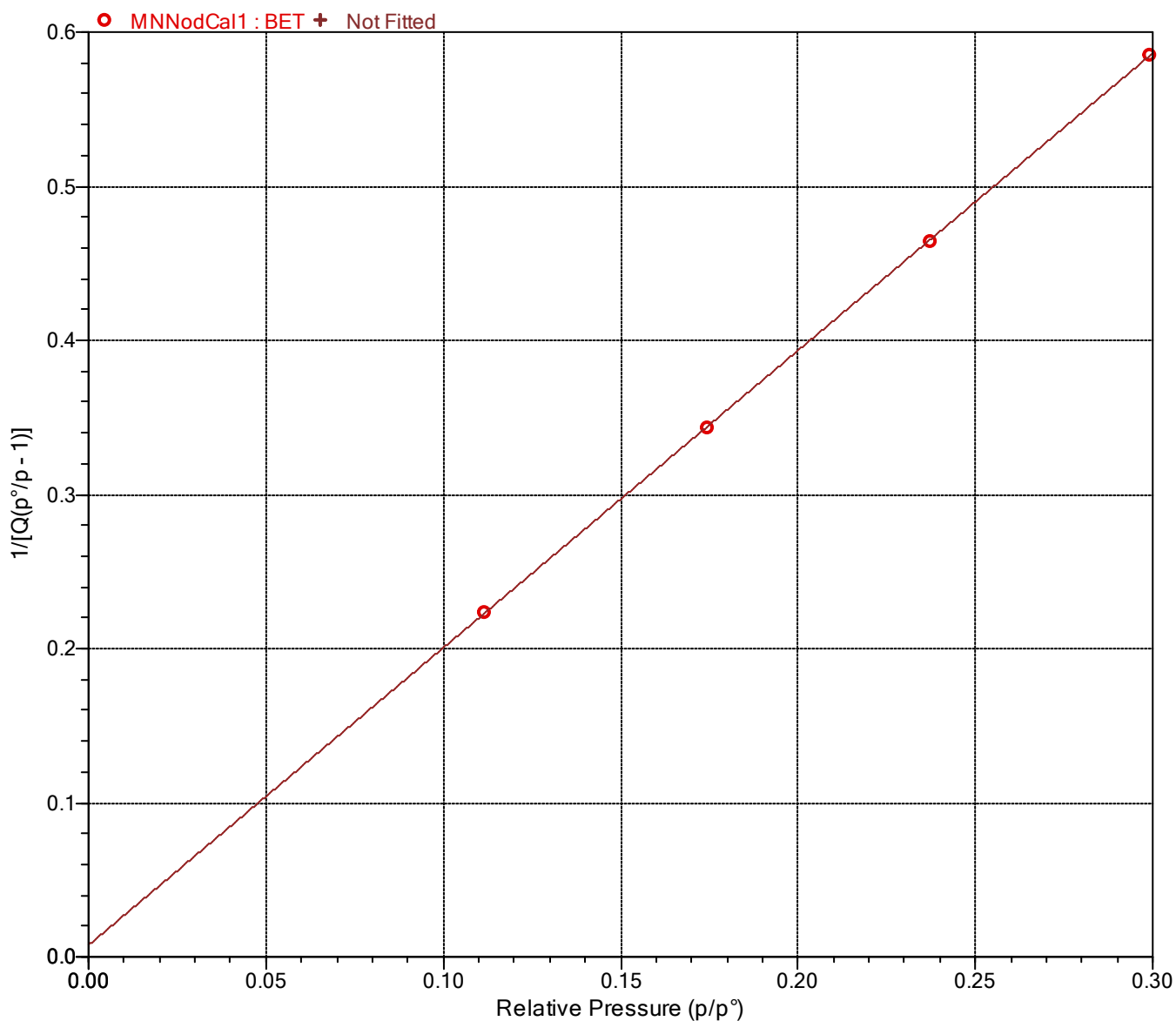Molecular cross-sectional area: 0,1620 nm²

Relative Pressure (p/p°)	Quantity Adsorbed (cm³/g STP)	1/[Q(p°/p - 1)]
0.111672974	0.5622	0.223604
0.174151132	0.6145	0.343175
0.237337738	0.6701	0.464370
0.299081967	0.7290	0.585333

Sample: BET
Operator:
Submitter:
File: C:\data\Jonas L\MNNodCal1.SMP

Started: 3/31/2022 1:48:49 PM	Analysis adsorptive: N2
Completed: 3/31/2022 4:17:35 PM	Analysis bath temp.: -195,850 °C
Report time: 4/1/2022 8:40:10 AM	Thermal correction: No
Sample mass: 1,7984 g	Ambient free space: 16,2355 cm³ Measured
Analysis free space: 56,1304 cm³	Equilibration interval: 5 s
Low pressure dose: None	Sample density: 1,000 g/cm³
Automatic degas: No	

BET Surface Area Plot

Plot legend: MNNodCal1 : BET + Not Fitted

Y-axis: $1/[Q(p^\circ/p - 1)]$

X-axis: Relative Pressure (p/p°)

Sample: BET
Operator:
Submitter:
File: C:\data\Jonas L\MNNodCal1.SMP

Started:	3/31/2022 1:48:49 PM	Analysis adsorptive:	N2
Completed:	3/31/2022 4:17:35 PM	Analysis bath temp.:	-195,850 °C
Report time:	4/1/2022 8:40:10 AM	Thermal correction:	No
Sample mass:	1,7984 g	Ambient free space:	16,2355 cm³ Measured
Analysis free space:	56,1304 cm³	Equilibration interval:	5 s
Low pressure dose:	None	Sample density:	1,000 g/cm³
Automatic degas:	No		

Sample Log

Date	Time	Log Message
3/31/2022	1:48:49 PM	Started analysis of file MNNodCal1.SMP on port 2.
3/31/2022	1:48:49 PM	System volume: 36.2726 cm³
3/31/2022	1:50:19 PM	Port 2 1000 mmHg transducer scale changed from 517,7836 to 517,7841 mmHg (fraction of nominal: 1.01).
3/31/2022	2:39:40 PM	Sample port 2 leak rate measured (interval: 30 s, rate: 0,000335 mmHg/min).
3/31/2022	2:48:23 PM	Ambient free-space measurement on sample port 2 complete (elapsed: 3572 s, qty in free-space: 16,2355 cm³, P1: 798,1556 mmHg, P2: 329,3620 mmHg, Tman: 45,0 °C, Tport: 45,0 °C).
3/31/2022	3:01:52 PM	Analysis free-space measurement on sample port 2 complete (elapsed: 4381 s, qty in free-space: 56,1304 cm³, P3: 173,4615 mmHg, Tport: 45,0 °C).
3/31/2022	3:35:15 PM	Psat port is charged with N2 at 762,7591 mmHg
3/31/2022	3:49:09 PM	Port 2 vacuum level is 2,40e-05 mmHg
3/31/2022	3:49:14 PM	Data collection started on sample port 2 (gas: N2).
3/31/2022	4:05:59 PM	Analysis termination started.
3/31/2022	4:17:35 PM	Finished a sample analysis for C:\data\Jonas L\MNNodCal1.SMP on port 2.

C   XRF analysis

D-LAB
DEGERFORS LABORATORIUM AB

Provningsresultat / Test Results:

Ordernr / Orderno
DL-73067

Beställare / Client	Referens / Reference
NTNU	**Arman Hoseinpur Kermani**

Adress / Address
Felles Fakturamottak,PO Box 50, Økern, NO-0508 OSLO

Er beställning / Your order No	Ankomstdag / Sample Registration Date	Utskriftsdatum / Date of issue	DL ID
	2022-02-21	**2022-02-22**	**707451**

Provbeteckning / Sample identity
Natural Mn ores

Noteringar / Notes
Order made by NTNU with N-number 22UV15716

Resultat/
Results

CaO	3.45 %
MgO	3.83 %
SiO_2	34.6 %
Al_2O_3	12.1 %
Fe_2O_3	7.00 %
MnO	23.3 %
Cr_2O_3	0.02 %
V_2O_5	0.05 %
TiO_2	0.87 %
NiO	1.14 %
Na_2O	2.57 %
K_2O	2.56 %
P_2O_5	0.41 %
SO_3	0.11 %
ZnO	0.11 %
MoO_3	< 0.01 %
CuO	0.84 %
ZrO_2	0.01 %
SrO	0.05 %
BaO	0.20 %
Cl	0.22 %
Co_3O_4	0.17 %
LOI	6.26 %
CeO_2	< 0.01 %

DEGERFORS LABORATORIUM

Björn Bernhardsson

Rapporten är signerad digitalt/
The report is digitally signed

D-LAB
DEGERFORS LABORATORIUM AB

Provningsresultat / Test Results:

Ordernr / Orderno
DL-73067

Beställare / Client	Referens / Reference
NTNU	**Arman Hoseinpur Kermani**

Adress / Address
Felles Fakturamottak,PO Box 50, Økern, NO-0508 OSLO

Er beställning / Your order No	Ankomstdag / Sample Registration Date	Utskriftsdatum / Date of issue	DL ID
	2022-02-21	**2022-02-22**	**707453**

Provbeteckning / Sample identity
Natural Mn ores - Roasted

Noteringar / Notes

Resultat/
Results

CaO	3.05 %
MgO	4.96 %
SiO_2	16.2 %
Al_2O_3	6.73 %
Fe_2O_3	8.84 %
MnO	48.0 %
V_2O_5	0.10 %
TiO_2	0.68 %
NiO	2.40 %
Na_2O	3.29 %
K_2O	1.26 %
P_2O_5	0.39 %
SO_3	0.22 %
ZnO	0.29 %
MoO_3	0.10 %
CuO	1.72 %
PbO	0.06 %
ZrO_2	0.03 %
SrO	0.08 %
BaO	0.28 %
Cl	0.03 %
Co_3O_4	0.36 %
LOI	0.81 %
Y_2O_3	0.03 %

This report may not be reproduced other than in full, except with the prior written approval of the issuing laboratory.

Note: The results are only valid for the sample that has been delivered to the laboratory.
We are not responsible for electronically transferred reports due to changes of data during transmission. Please contact us in doubtful cases.

DEGERFORS LABORATORIUM

Björn Bernhardsson

Rapporten är signerad digitalt/
The report is digitally signed

D   Normalization

Normalization of the raw polymetallic manganese nodules

1	2	3	4	5	6
Compound	wt%	100g	MnO->MnO2	100g w/o LOI	Adding LOI
CaO	3.45	3.45	3.45	3.49	2.95
MgO	3.83	3.83	3.83	3.87	3.28
SiO2	34.6	34.64	34.64	34.99	29.60
Al2O3	12.1	12.11	12.11	12.24	10.35
Fe2O3	7	7.01	7.01	7.08	5.99
MnO/MnO$_2$	23.3	23.33	28.59	28.88	24.43
Cr2O3	0.02	0.02	0.02	0.02	0.02
V2O5	0.05	0.05	0.05	0.05	0.04
TiO2	0.87	0.87	0.87	0.88	0.74
NiO	1.14	1.14	1.14	1.15	0.98
Na2O	2.57	2.57	2.57	2.60	2.20
K2O	2.56	2.56	2.56	2.59	2.19
P2O5	0.41	0.41	0.41	0.41	0.35
SO3	0.11	0.11	0.11	0.11	0.09
ZnO	0.11	0.11	0.11	0.11	0.09
MoO3	0.01	0.01	0.01	0.01	0.01
CuO	0.84	0.84	0.84	0.85	0.72
ZrO2	0.01	0.01	0.01	0.01	0.01
SrO	0.05	0.05	0.05	0.05	0.04
BaO	0.20	0.20	0.20	0.20	0.17
Cl	0.22	0.22	0.22	0.22	0.19
Co3O4	0.17	0.17	0.17	0.17	0.15
CeO2	0.01	0.01	0.01	0.01	0.01
LOI	6.26	6.27	6.27	0.00	15.4
SUM	99.89	100.00	105.26	100	100

1 and 2: Data of the raw polymetallic manganses nodules received from Dregerfors Laboratorium AB

3: Normalizing for 100g by multiplying each cell in column 2 by the sum of column 2 and multiplying by 100.

4: Replacing MnO with MnO$_2$ by multiplying with the molar mass of MnO$_2$ divided by the molar mass of MnO (1Mn are added are removed).

5: Normalizing for 100g without LOI. Same as 3, but subtracting LOI from the SUM.

6: Adding LOI of 15.4 by multiplying all cells in 5 by 0.846

Normalization of the calcined polymetallic manganese nodules

1	2	3	4	5	6
Compound	wt%	100g	MnO->Mn2O3	100g w/o LOI	Adding LOI
CaO	3.05	3.05	3.05	2.92	2.89
MgO	4.96	4.96	4.96	4.75	4.71
SiO2	16.2	16.21	16.21	15.50	15.37
Al2O3	6.73	6.74	6.74	6.44	6.39
Fe2O3	8.84	8.85	8.85	8.46	8.39
MnO	48	48.04	53.46	51.11	50.69
V2O5	0.1	0.10	0.10	0.10	0.09
TiO2	0.68	0.68	0.68	0.65	0.65
NiO	2.4	2.40	2.40	2.30	2.28
Na2O	3.29	3.29	3.29	3.15	3.12
K2O	1.26	1.26	1.26	1.21	1.20
P2O5	0.39	0.39	0.39	0.37	0.37
SO3	0.22	0.22	0.22	0.21	0.21
ZnO	0.29	0.29	0.29	0.28	0.28
MoO3	0.1	0.10	0.10	0.10	0.09
CuO	1.72	1.72	1.72	1.65	1.63
PbO	0.06	0.06	0.06	0.06	0.06
ZrO2	0.03	0.03	0.03	0.03	0.03
SrO	0.08	0.08	0.08	0.08	0.08
BaO	0.28	0.28	0.28	0.27	0.27
Cl	0.03	0.03	0.03	0.03	0.03
Co3O4	0.36	0.36	0.36	0.34	0.34
Y2O3	0.03	0.03	0.03	0.03	0.03
LOI	0.81	0.81	0.81	0.00	0.81
SUM	99.91	100.00	105.42	100	100

1 and 2: Data of the calcined polymetallic manganese nodules received from Dregerfors Laboratorium AB

3: Normalizing for 100g by multiplying each cell in column 2 by the sum of column 2 and multiplying by 100.

4: Replacing MnO with Mn_2O_3 by multiplying with the molar mass of Mn_2O_3 divided by 2 times the molar mass of MnO (2Mn are added are removed).

5: Normalizing for 100g without LOI. Same as 3, but subtracting LOI from the SUM.

6: Adding LOI back (it should stay the same wt%) by multiplying all cells in 5 by 0.9919.